

5-2014

Advancements in alternative energy applications for space conditioning.

Brian S. Robinson
University of Louisville

Follow this and additional works at: <https://ir.library.louisville.edu/etd>

Part of the [Mechanical Engineering Commons](#)

Recommended Citation

Robinson, Brian S., "Advancements in alternative energy applications for space conditioning." (2014). *Electronic Theses and Dissertations*. Paper 1221.
<https://doi.org/10.18297/etd/1221>

This Doctoral Dissertation is brought to you for free and open access by ThinkIR: The University of Louisville's Institutional Repository. It has been accepted for inclusion in Electronic Theses and Dissertations by an authorized administrator of ThinkIR: The University of Louisville's Institutional Repository. This title appears here courtesy of the author, who has retained all other copyrights. For more information, please contact thinkir@louisville.edu.

ADVANCEMENTS IN ALTERNATIVE ENERGY APPLICATIONS FOR SPACE
CONDITIONING

By

Brian S. Robinson
BS, University of Louisville, 2008
MEng, University of Louisville, 2009

A Dissertation
Submitted to the Faculty of
J.B. Speed School of Engineering at the University of Louisville
in Partial Fulfillment of the Requirements
for the Degree of

Doctor of Philosophy

Department of Mechanical Engineering
University of Louisville
Louisville, KY

May 2014

ADVANCEMENTS IN ALTERNATIVE ENERGY APPLICATIONS FOR SPACE
CONDITIONING

By

Brian S. Robinson
BS, University of Louisville, 2008
MEng, University of Louisville, 2009

A Dissertation Approved on

April 22, 2002

By the following Dissertation Committee:

Dr. M. Keith Sharp

Dr. William Hnat

Dr. Ellen Brehob

Dr. Andrea Kelecy

Dr. William Biles

ABSTRACT
ADVANCEMENTS IN ALTERNATIVE ENERGY APPLICATIONS FOR SPACE
CONDITIONING

Brian S. Robinson

April 22, 2014

This dissertation documents advancements made in passive, renewable energy applications for building space conditioning (heating and cooling). Since, for most climates across the US, space heating requires a much larger annual energy demand than space cooling, the majority of this dissertation is focused on the heating season. The dissertation is divided into five chapters, primarily covering computer simulations and experimental studies pertaining to specific space conditioning technologies. Chapter One discusses the significance of supplanting fossil fuel based energy production with clean, renewable sources, and provides further detail on the organization of this dissertation. Chapter Two provides background on the heat pipe augmented solar wall – a passive solar space heating technology. Additionally, the design, construction, and experimental analysis of the first full-scale prototype for this system are highlighted in the chapter. A new heat pipe system design, which improved heating performance over the original, is the focus of Chapter Three. A prototype of the new model was also constructed, and both models were tested side-by-side in a passive solar test facility, constructed on campus grounds. Exclusive focus on heating loads in Chapters Two and Three shifts to total space conditioning loads in Chapter Four. The heat pipe wall is still the subject of this

chapter, in which the effectiveness of implemented system mechanisms in reducing unwanted thermal gains to the room during the cooling season was investigated. Chapter Five focuses on the cooling season only, and lays the groundwork for space cooling solutions by studying the potential of four different ambient sources to meet annual space cooling loads. This final chapter also considers the theoretical thermal storage that would be required, for each respective ambient source, to serve cooling loads throughout the US.

TABLE OF CONTENTS

ABSTRACT.....	iii
LIST OF TABLES.....	viii
LIST OF FIGURES.....	ix
CHAPTER 1: INTRODUCTION	1
1.1. The Fossil Fuel Dilemma.....	1
1.2. Dissertation Objectives	5
1.3. Dissertation Organization	7
CHAPTER 2: HEATING SEASON PERFORMANCE OF A FULL-SCALE HEAT PIPE ASSISTED SOLAR WALL	9
2.1. Chapter 2 Overview	9
2.2. The Heat Pipe Augmented Solar Space Heating System.....	10
2.2.1 System Fundamentals	10
2.2.2 Previous Work	12
2.3. Chapter 2 Methods.....	13
2.3.1 Prototype Design and Construction	13
2.3.2 Instrumentation	16
2.3.3 Data Analysis.....	16
2.3.4 Error Propagation.....	22
2.4. Chapter 2 Results	23
2.5. Chapter 2 Discussion	26
CHAPTER 3: HEATING SEASON PERFORMANCE IMPROVEMENTS FOR A SOLAR HEAT PIPE SYSTEM	29
3.1. Chapter 3 Overview	29
3.2. Chapter 3 Introduction	30
3.3. Chapter 3 Methods.....	33
3.3.1 Computer Modeling.....	33
3.3.2 Passive Solar Test Facility (PSTF)	37

3.3.3 Heat Pipe System Modifications.....	39
3.3.4 Instrumentation	41
3.3.5 Data Analysis	41
3.3.6 Error Propagation.....	47
3.3.7 Matching Simulations to Full-scale Performance	49
3.4. Chapter 3 Results & Discussion	50
3.4.1. Computer Simulations	50
3.4.2. Passive Solar Test Facility	53
3.4.3. Heat Pipe Systems Experiments	55
3.4.4 Matching Simulations and Experiments	59
3.5. Chapter 3 Conclusions	63
CHAPTER 4: REDUCING UNWANTED THERMAL GAINS DURING	
THE COOLING SEASON FOR A SOLAR HEAT PIPE SYSTEM.....	65
4.1 Chapter 4 Overview	65
4.2. Chapter 4 Introduction	66
4.3. Chapter 4 Methods.....	69
4.3.1 Computer Modeling.....	69
4.3.2 Experimental Setup.....	78
4.3.3 Instrumentation	80
4.3.4 Data Analysis	82
4.3.5 Error Propagation.....	88
4.4. Chapter 4 Results & Discussion	91
4.4.1 Bench-scale Experiments.....	91
4.4.2. Simulations	91
4.4.3 Full-scale Experiments.....	98
4.5. Chapter 4 Conclusions	102
CHAPTER 5: U.S. SPACE COOLING POTENTIALS FOR AMBIENT	
SOURCES WITH THERMAL ENERGY STORAGE	105
5.1. Chapter 5 Overview	105
5.2. Chapter 5 Introduction	105
5.3. Chapter 5 Methods.....	109
5.3.1. Annual Cooling Potential.....	110

5.3.2. Cooling Potential with Diurnal Storage	113
5.3.3. Storage Capacity for 100% Ambient Source Cooling	114
5.4. Chapter 5 Results	117
5.5. Chapter 5 Discussion	128
5.6. Chapter 5 Conclusions	132
CONCLUSIONS	135
REFERENCES	136
APPENDICES	140
Supplementary Analysis of Matching Simulations with Experimental Results for the New Heat Pipe System	140
Nomenclature for Chapter 2: “Heating Season Performance of a Full-Scale Heat Pipe Assisted Solar Wall”	142
Nomenclature for Chapter 3: “Heating Season Performance Improvements for a Solar Heat Pipe System”	144
Nomenclature for Chapter 4: “Reducing Unwanted Thermal Gains during the Cooling Season for a Solar Heat Pipe System”	148
Nomenclature for Chapter 5: “U.S. Space Cooling Potentials for Ambient Sources with Thermal Energy Storage”	152
CURRICULUM VITAE	154

LIST OF TABLES

Table 3.1. Description of thermal conductance values used for heat pipe wall thermal network models.	36
Table 3.2. Value for each derivative associated with overall uncertainty in calculated system efficiency.	49
Table 3.3. Rated R-values and calculated UA values for key components of one room.	54
Table 3.4. Conductances before and after matching with experiments.	62
Table 4.1. Description of thermal conductance values used for heat pipe wall thermal network models.	70
Table 4.2. Value for each derivative associated with overall uncertainty in calculated system efficiency for the bench-scale experiments.	90
Table 4.3. Value for each derivative associated with overall uncertainty in calculated system thermal gains for the full-scale prototype.	90
Table 4.4. Cooling season for eight locations based on SD ratio.	94
Table 5.1. Description of ASHRAE-defined climate subzones within the continental US, and the representative cities used for this study.	113
Table 5.2. Specific heat values for the thermal storage mediums.	117
Table 5.3. Louisville, KY maximum and average daily cooling potentials for $T_{c,hi} = 72^{\circ}\text{F}$	121

LIST OF FIGURES

Figure 2.1. Isolated gain passive solar system with thermosyphoning collector.....	10
Figure 2.2. Isolated gain passive solar heating system with five heat pipes between the absorber and thermal mass.....	11
Figure 2.3. Schematic of heat pipe operation.....	11
Figure 2.4. Isometric sketch of the prototype and 2D schematic of one unit.	14
Figure 2.5. Thermal resistance network from the thermal mass to the room.	18
Figure 2.6. Average hourly values for insolation, room gain, and tank, room & ambient temperatures for January 28 & 29.....	23
Figure 2.7. Average hourly values for system trends for February 22-26.....	24
Figure 2.8. Plot of hourly average useful gains versus hourly average solar input from 9 am – 5 pm for each day of the selected heating season.	25
Figure 2.9. System efficiency versus loss potential/insolation ratio.....	26
Figure 3.1. Schematic of full-scale heat pipe assisted solar wall prototype.	30
Figure 3.2. Schematic of heat pipe operation.....	31
Figure 3.3. Thermal network for the heat pipe assisted solar wall.	34
Figure 3.4. Thermal network for the heat pipe assisted solar wall with one or more condensers exposed directly to room air.....	35
Figure 3.5. South view of the passive solar test facility..	38
Figure 3.6. Schematic of a new model of the heat pipe wall prototype highlighting significant design modifications of the previous model.	40
Figure 3.7. Thermal resistance network used to calculate q_{out} for heating units with a thermal storage tank.....	43
Figure 3.8. Thermal resistance network used to calculate q_{out} for a heating unit with the condenser exposed directly to room air.	45
Figure 3.9. Solar fraction for the previous prototype and modifications implemented for the new prototype.....	51
Figure 3.10. Simulated solar fractions on January 15 for three condenser unit configurations.	52
Figure 3.11. Annual solar fraction for each condenser configuration.	53
Figure 3.12. Annual solar fraction for the new system at four different Load-to-Collector ratios.....	54

Figure 3.13. Average hourly values for insolation, ambient temperature, and absorber and evaporator temperatures for both experimental prototypes for January 15 through 18.	55
Figure 3.14. Average hourly values for insolation, ambient temperature, and tank and room temperatures for both experimental prototypes for February 14 through 16.	57
Figure 3.15. Average and maximum tank and room temperatures for both experimental prototypes over the entire testing period.	58
Figure 3.16. New system efficiency versus loss potential/insolation ratio.	59
Figure 3.17. Simulated and experimental evaporator, tank and room temperatures, from January 5 – 7, after matching.	62
Figure 4.1. Schematic of the solar heat pipe system highlighting design modifications relative to the previous model.	68
Figure 4.2. Thermal network for the heat pipe assisted solar wall.	69
Figure 4.3. Shading (blocking of beam radiation) to reduce unwanted gains.	72
Figure 4.4. Opaque cover (blocking all solar radiation) to reduce unwanted gains.	73
Figure 4.5. Valve to reduce unwanted gains.	73
Figure 4.6. Switching to reduce unwanted gains.	74
Figure 4.7. Schematic of model used for bench-scale experiments.	78
Figure 4.8. Thermal resistance network used to calculate \dot{q}_{in} for heating units with a thermal storage tank.	83
Figure 4.9. Thermal resistance network used to calculate q_{out} for a heating unit with the condenser exposed directly to room air.	86
Figure 4.10. Collector efficiency data for the PSTF prototype using data collected during normal operation on January & February 2013.	88
Figure 4.11. Annual loads for four locations without the heat pipe wall.	91
Figure 4.12. Annual unwanted gains, auxiliary heating and total energy load for Louisville utilizing the heat pipe wall (without reduction mechanisms) for room comfort ranges of 18.3-23.9°C (65-75°F), 20.0-22.2°C (68-72°F) & 20.6-21.7°C (69-71°F)	93
Figure 4.13. Annual loads for four locations with the heat pipe wall.	93
Figure 4.14. Annual loads for four locations for each control strategy using the cover mechanism.	95
Figure 4.15. Annual loads in Louisville for unwanted gains reduction mechanisms with ambient temperature based control.	97
Figure 4.16. Total annual loads with different mechanisms with ambient temperature-based control strategy.	98
Figure 4.17. Prototype efficiency with and without the valve mechanism on August 22 - 24, 2013.	99

Figure 4.18. Prototype efficiency with and without the cover mechanism on September 9 - 11, 2013.	99
Figure 4.19. Prototype efficiency with and without the combination of valve and cover mechanisms on August 28 - 30, 2013.	100
Figure 4.20. Simulated annual and experimental three-day unwanted gains reductions in Louisville.	101
Figure 4.21. Prototype exposed condenser temperatures using the valve mechanism on August 22, 2013, and without the valve mechanism on January 3, 2013.	102
Figure 5.1. Average monthly temperatures of ambient energy sources relative to indoor comfort temperatures in Louisville, KY.	108
Figure 5.2. Annual cooling load (CDD) for $T_b = 65^\circ\text{F}$	118
Figure 5.3. Annual cooling load (CDD) for $T_b = 72^\circ\text{F}$	119
Figure 5.4. Annual dry-bulb cooling capacity for $T_{c,hi}=72^\circ\text{F}$	119
Figure 5.5. Annual wet-bulb cooling capacity for $T_{c,hi}=72^\circ\text{F}$	120
Figure 5.6. Annual ground temperature cooling capacity for $T_{c,hi}=72^\circ\text{F}$	120
Figure 5.7. Annual sky temperature cooling capacity for $T_{c,hi}=72^\circ\text{F}$	121
Figure 5.8. Ambient potential to cooling load ratio for dry-bulb (DB), wet-bulb (WB), ground temperature (GT) and sky temperature (ST) ambient sources.	122
Figure 5.9. Cooling load and cooling capacity (degree days F) from ambient air for Denver, CO.	123
Figure 5.10. Cooling load and cooling capacity (degree days F) from sky for Denver, CO.	123
Figure 5.11. Annual ambient potential fraction, $F_{as,ld}$, for all possible combinations of ambient sources for 11 locations.	124
Figure 5.12. Storage capacity to building overall loss coefficient ratio C^* for ambient sources requiring thermal mass for 11 locations.	125
Figure 5.13. Values throughout the year for CDD_{nas} and C^* for dry-bulb in Albuquerque, NM.	126
Figure 5.14. Values throughout the year for CDD_{nas} and C^* for dry-bulb in New Orleans, LA.	126
Figure 5.15. F_{as} versus C/C^*_{max} for Albuquerque, NM.	127
Figure 5.16. F_{as} versus C/C^*_{max} for New Orleans, LA and Phoenix, AZ.	127
Figure 5.17. Required mass per square meter of floor area and for four different storage materials for a building that meets the PassivHaus standard.	128
Figure 5.18. Required thickness per square meter of floor area and for four different storage materials for a building that meets the PassivHaus standard.	128

CHAPTER 1: INTRODUCTION

1.1. The Fossil Fuel Dilemma

The United States Energy Information Administration (EIA) states that 82% of the world's production is sourced by fossil fuels (i.e. coal, petroleum and natural gas) [<http://www.eia.gov/totalenergy/data/monthly/previous.cfm>]. The burning of fossil fuels is the primary source of deleterious pollution in our atmosphere. The negative combustion byproducts of fossil fuels include carbon dioxide (considered by many to be the most threatening of greenhouse gases), carbon monoxide, nitrous oxides, unburned hydrocarbons, particulate matter and smoke. Dangerous side effects resulting from these emissions include sulfuric acid rain, respiratory related biological disease and skin cancer from ozone depletion. Perhaps the most alarming consequence of these emissions is global climate change due to the deposition of greenhouse gases into our atmosphere. Climate change introduces additional damaging consequences such as the melting of polar ice caps, rising sea levels and provincial extremes of precipitation and drought.

Considering these consequences that are detrimental to the ecology and climate of the planet, greenhouse gas emissions show disturbing trends over the past two centuries. The National Oceanic and Atmospheric Administration (NOAA) states that for the vast majority of the last several centuries, carbon dioxide (CO₂) levels ranged between 100 and 300 parts per million by volume (ppmv) [<http://www.esrl.noaa.gov/gmd/ccgg>]

[/trends/history.html](#)]. Prior to the start of the Industrial Revolution, CO₂ levels were at 280 ppmv [Trenbert *et al.*, 2007]. CO₂ levels in the year 2000 were at 380 ppmv and increasing at a rate of nearly 2 ppmv per year [Trenbert *et al.*, 2007]. Over the last decade, average worldwide emission of CO₂ has increased annually by 2.5% [EIA Annual Energy Review, 2011].

Despite objections from a dwindling contingent of citizens, politicians and even scientists, research overwhelming suggests that the earth is warming. The average temperature of the last 50 year period has been warmer than any other 50 year period for the last 1,300 years [Hegerl *et al.*, 2007]. Viewed by many as the authority on global warming trends and climate change concerns, the Intergovernmental Panel on Climate Change (IPCC) has revealed that CO₂ emissions over the past century has raised global temperature by about 0.74 °C [https://www.ipcc.ch/publications_and_data/ar4/wg1/en/tssts-3-1-1.html]. Although this increase may initially seem inconsequential, it is anything but in light of the extreme sensitivity concerning polar ice cap melting rates, global air currents, oceanic salinity and associated undersea currents.

It is also evident that current energy production and consumption trends, if not curbed by alternative energy sources, will quickly deplete the planet's resources and endanger the survival of future generations. Moreover, the finite nature of fossil fuel resources will have negative impacts on U.S. economy. The decrease in fossil fuel production will increase the need for energy imports and accelerate the rising costs of fuel. The law of supply and demand dictates that the price of oil products will continue to increase, and these trends have become more apparent in the last decade, especially over the past few years. As fossil fuel costs increase, it should be anticipated that new technology will

cause alternative energy costs to decrease – but the impetus for technological development is *now*.

The desperate state of dependence our nation has on foreign energy imports creates yet another crucial disadvantage. Not only do these levels of dependence pose a large threat to U.S. economic stability, but they also endanger U.S. national security. The fact that a significant portion of our nation's fossil fuel imports originate in geographical regions that have historically had some form of (often times quite serious) conflict with the U.S., furthermore provides a legitimate motive for developing alternative solutions.

Recognizing the economic strains resulting from a fossil fuel dependent population, it is also pertinent to note the promising economic potential in an alternative energy sourced nation. Presently, the U.S. is recovering from a rather considerable economic recession. While noteworthy recessions such as this may not be common, this nation still had to suffer a handful of recessive periods in the 20th century alone. A key factor in economic recovery from virtually all of these setbacks was the establishment of new industry; such as the auto industry in the early 20th century, the airlines industry in the mid 20th century, and the information technology industry in the late 20th century. As for the current economic state, it is the author's opinion that no contemporary candidate for a prosperous new industry has more significance or potential than the alternative energy industry.

Compared to any previous time in recorded human history, present day energy consumption and concerns for meeting demand are at an all time high. World energy production experienced slow growth all the way through the 18th century, but the onset of the Industrial Revolution in the early 19th century has radically increased world energy

demand ever since. In 1998 Dahl and McDonald [1998] predicted that, by 2028, world energy demand will triple. Over the last fifty years, world energy production has increased tenfold, yet energy per capita has barely tripled [Vanek & Albright, 2008], thus demand has more than tripled (since world population has also increased). This is a consequence of the vast majority of the world's energy production and consumption being concentrated primarily within those nations that embraced the Industrial Revolution, while the remainder of the world lagged behind. However, with each passing decade in the nearly 200 years since, more nations continue to stake their claim in the global economy, resulting in rapid economic development to meet modern standards and, in turn, immense increases in world energy demand.

Perhaps the greatest predicament of all that society, eventually and inevitably, will need to address is the fact that fossil fuels are a limited resource on our planet. North American oil production is expected to decline by 80% by the year 2030 [Zittel and Schindler, 2007] and the rest of the world is following the same trend. Coupled with increasing global populations, global industrialization and geopolitical concerns, the stress on global energy demand will only become greater. In today's modern world, few scenarios can be envisioned that would cause greater international conflict than that of a worldwide energy crisis.

Obviously, to suggest that world economies should regress from modernization as a solution to the impending energy crisis is both undesirable and unrealistic. These issues caused by overwhelmingly increasing energy demand in conjunction with dwindling fossil fuel resources can nevertheless be rectified if alternative forms of energy can account for a greater percentage of consumable energy; slowing the depletion rate of

fossil fuel resources until, hopefully, a new age when alternative energy effectively accounts for 100% of world production and consumption. Over the past several decades, more and more leaders within the scientific and political communities have acknowledged this crucial obligation and related research has improved accordingly. However, the abundant types of energy end use within each sector has been and will likely continue to be addressed separately, whereas the most advantageous alternative energy source and application for meeting demand may vary from one category of end use to the next.

One of the more significant forms of energy end use is building space conditioning (i.e. space heating and cooling). Although the U.S. accounts for approximately 5% of the world population, it consumes nearly 25% of the world's energy production [Tester *et al.*, 2005]. The residential, commercial and industrial energy sectors of the U.S. accounts for 22%, 19% and 31% of the national energy demand, respectively [EIA, 2011]. For each of these sectors, building space heating and cooling demand represents 54% of the residential load, 18% of the commercial load and 9% of the industrial load [EIA, 2011]. Therefore, supplanting fossil fuel based energy production for building space conditioning with alternative energy solutions would account for nearly 18.1% of total U.S. energy demand and nearly 5% (4.5%) of the entire planet's energy demand!

1.2. Dissertation Objectives

Advancements in alternative energy applications for space conditioning is the focus of the research conducted for this dissertation. It will be shown in the following text that building heating loads account for a much larger percentage of the total space conditioning loads than do cooling loads in most climates across the US. Hence, the

primary focus for most of the studies within this dissertation is on the heating season. Studies on space heating were focused exclusively on a novel passive solar energy application – the heat pipe assisted solar wall. Research objectives for this system included the design, construction, and operational analysis of an original full scale heat pipe system prototype. Based on experimental results for the original prototype, a new model was designed with the objective to further enhance system heating performance. Computer simulations were used to confirm enhanced performance of the new design and a new prototype was constructed. Additionally, a two-room passive solar test facility (PSTF) was constructed with the objective of comparative system performance evaluation between the original and new prototype, respectively, under ideal solar testing conditions. The next research objective was to significantly reduce and/or eliminate unwanted additional thermal gains from the heat pipe system to the room during the cooling season. This was addressed by using computer simulations and experimental research for control mechanisms and strategies utilized in conjunction with the new heat pipe model. Research exclusive to space cooling included a study, using computer algorithms, to establish the cooling capabilities of four different ambient sources. Specific objectives for this study, focused on climates throughout the continental U.S., were to assess the annual cooling potential of each ambient source and the cooling potential for each respective source utilizing diurnal storage. In addition, the amount of thermal storage, for each respective ambient source, that would be theoretically required to serve annual cooling loads throughout the nation was assessed.

1.3. Dissertation Organization

Each of the following chapters contains individual journal publications that constitute research pertaining to this dissertation. Chapter 2 consists of the first publication, “Heating Season Performance of a Full Scale Heat Pipe Assisted Solar Wall,” which details the operation of the original heat pipe assisted solar wall prototype. The second paper, “Heating Season Performance Improvements for a Solar Heat Pipe System,” is found in Chapter 3 and details the benefits of a modified heat pipe system over the previous, including side-by-side experimental results for each system installed in the PSTF. The fourth chapter contains “Reducing Unwanted Thermal Gains during the Cooling Season for a Solar Heat Pipe System,” and this study details the effectiveness of four different control mechanisms and three different control strategies in reducing thermal gains from the system to the room. This paper also shifts the focus in the direction of the total space conditioning load, which includes the cooling season. The cooling season is the exclusive focus for the final paper, titled “U.S. Space Cooling Potential for Ambient Sources with Thermal Energy Storage” and found in Chapter 5. This paper lays the groundwork for passive alternative space cooling solutions by investigating the cooling potential of four different alternative ambient sources that could be used for cooling.

The first paper (Chapter 2) has been published in *Solar Energy* and the last paper (Chapter 5) has also been published online in the *Journal of Ambient Energy* (the printed version will be available in a future journal issue later this year). Full references for both these articles are found in the appendices. The remaining two papers (Chapters 3 and 4) have been submitted to *Solar Energy* and are currently under review.

The content within the following chapters are identical to each respective publication, with the following exceptions:

- To comply with university dissertation guidelines, this document is restricted to one official abstract summarizing the entire dissertation. Thus, the opening section in each chapter is titled “Overview”, and these sections are identical to the actual abstract(s) from each individual publication.
- To comply with university dissertation guidelines, individual references from each publication have been removed from their respective chapters and consolidated into the section directly after the body of this dissertation.
- A modification was made to the error propagation methodology in section 2.3.4 that resulted in a calculated uncertainty (for thermal efficiency) that was different than the value reported in the actual publication.
- Numerical changes have been made for figures, tables and equations to provide uniformity within this document.
- Many of the figures are shown in color; whereas all figures in the publications were grayscale.
- To avoid reader confusion, some of the variables have been changed to ensure uniformity amongst individual chapters. (For example, useful thermal gains into the heat pipe system, used to calculate system efficiency, were represented as \dot{Q}_{in} for one paper, and \dot{Q}_u was used to represent the same parameter in another paper; thus the latter variable was selected to replace the former in this document.)
- Listings of nomenclature for each individual paper are found in the appendices.

CHAPTER 2: HEATING SEASON PERFORMANCE OF A FULL-SCALE HEAT PIPE ASSISTED SOLAR WALL

2.1. Chapter 2 Overview

Previous computer simulations and bench-scale experiments showed that the heat pipe assisted solar wall had the potential for significantly improved performance relative to conventional passive space heating systems. To further test this potential, a full-scale prototype of the heat pipe system was designed, built and installed in a classroom on the University of Louisville campus in Louisville, KY. During the spring heating season of 2010 (January – April), maximum daily peak thermal efficiency was 83.7% and average daily peak thermal efficiency was 61.4%. The maximum hourly average room gain achieved during the season was 163 W/m². On days with good solar insolation, the thermal storage was heated to temperatures sufficient to provide significant energy to the classroom, even during the coldest days of the season. During the longest period (4 days) of low insolation during the season, average hourly heat delivery to the room from storage remained positive, and was never less than 16.6 W/m². During good insolation days following a period of consecutive low insolation days, thermal storage temperature was quickly restored to levels comparable to those obtained during consecutive good insolation days. Estimated heat removal factor * transmittance absorptance product, $F_R(\tau\alpha)$, and heat removal factor * overall loss coefficient, $F_R U_L$, values for the system were comparable to those for glazed liquid active collectors.

2.2. The Heat Pipe Augmented Solar Space Heating System

2.2.1 System Fundamentals

The heat pipe augmented solar space heating system [Corliss, 1979; Susheela and Sharp, 2001] is a type of isolated gain passive heating system. Isolated gain systems experience solar gains via a collector system that does not cause increased losses through the south wall of the building, as glass windows do in direct and indirect gain systems. This “thermal diode” effect significantly improves system performance. Conventional systems (Figure 2.1) require a substantial elevation difference between the collector and storage/room to drive thermosyphoning of a single-phase fluid. However, two-phase heat transfer in a heat pipe allows the system to operate with a small elevation difference so that the entire system can be installed in the south wall (Figure 2.2).

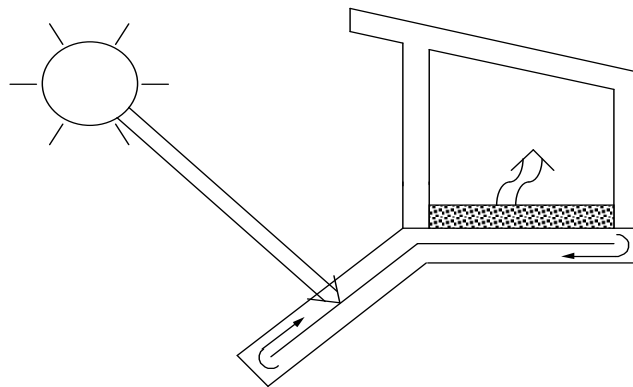


Figure 2.1. Isolated gain passive solar system with thermosyphoning collector.

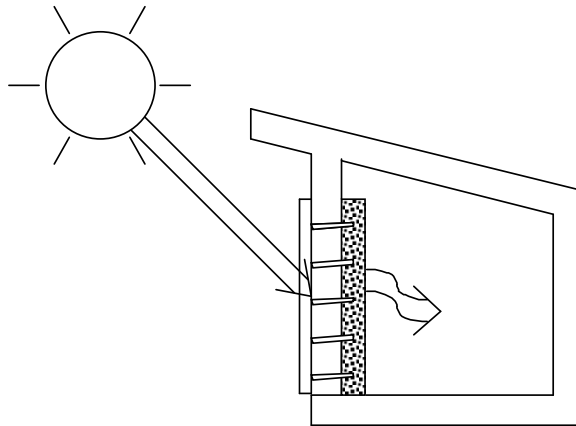


Figure 2.2. Isolated gain passive solar heating system with five heat pipes between the absorber and thermal mass.

When insolation on the absorber raises the temperature of the evaporator section above that of the condenser section, the liquid inside is boiled into a vapor (Figure 2.3). The vapor then rises through the adiabatic (vapor) section, which passes through the insulated wall of the building, and reaches the condenser end where the vapor condenses and transfers its energy to the thermal mass. The condensed liquid then flows back to the evaporator section by gravity, completing the cycle.

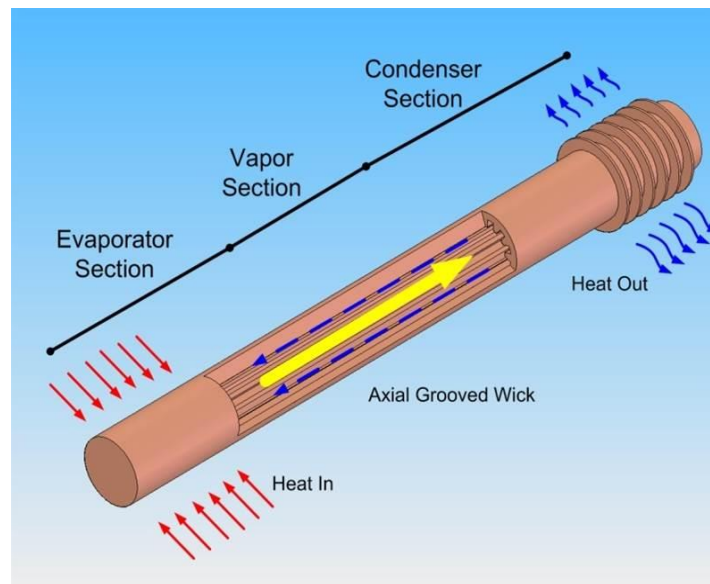


Figure 2.3. Schematic of heat pipe operation.

2.2.2 Previous Work

Susheela and Sharp [2001] designed and tested a heat pipe system that could be installed on existing homes without demolishing the wall of the building. The absorber portion was mounted on the outside of a south-facing wall, with water contained in tanks as the thermal mass on the inside of the wall. Holes were drilled in the existing wall for the adiabatic sections of the heat pipes to pass through, connecting the absorber and water tanks. The heat pipes had a 5 degree slope throughout and were made from copper pipe with 1 inch inner diameter, with DuPont SUVA-124 refrigerant (chlorotetrafluoroethane) as the working fluid and a stainless steel wire wicking structure. Experiments were performed outdoors, and system efficiencies (defined as the ratio of power delivered to the room over incident insolation) reached 60–80% during sunny days. Computer simulations were also performed to model the performance of the unit.

Albanese et al. [2012] followed Susheela and Sharp's recommendations for improvements on their design, and developed computer simulations for similar heat pipe systems. Computer simulations were run for a large number of variations in system parameters, including glazing characteristics, selective surfaces, absorber thicknesses, insulation properties, and the number and material of heat pipes. Parametric studies showed that several parameters had minimal effect on system performance relative to the baseline design, including number of covers, absorber thickness and material, collector edge insulation, heat pipe material, number of heat pipes, tank wall conductivity and thickness, tank to room conductance, condenser fins, and wall insulation. Therefore, compromises in these areas to reduce system cost while maintaining good thermal performance are possible. Parameters with greater effect on system performance were

cover thickness and extinction coefficient, thermal storage capacity, a thin low-iron glass cover, a high-performance selective absorber surface and large storage capacity being favorable.

Additionally, Albanese et al. [2012] constructed a bench-scale experimental model to further assess parametric heat pipe system performance. A fill level of 120% of the evaporator volume produced the highest system efficiency and insulating the adiabatic section of the heat pipe improved efficiency for all fill levels. The addition of condenser fins did not significantly improve system performance. Utilizing the optimal parameter values, a system efficiency of 85% was attained.

To better understand system performance in realistic weather conditions, in particular, the relatively cloudy and cool conditions in Louisville, KY, a full-scale experimental prototype was constructed and installed in a classroom on campus, facing 10° east of south. This paper will outline prototype design and construction, and report prototype performance for the spring 2010 heating season in Louisville.

2.3. Chapter 2 Methods

2.3.1 Prototype Design and Construction

The design (Figure 2.4) consisted of five individual heating units, each with an absorber plate, heat pipe and water tank [Chmielewski, 2009]. The evaporator section was glued and clamped to an aluminum absorber. The adiabatic section of the heat pipe extended through a layer of thermal insulation to the condenser, which was placed within a water tank for thermal mass. An aluminum frame supported and enclosed the five sets of absorbers, heat pipes, and water tanks, as well as a glazing on the south side of the

assembly. The north side of the system was faced with a screen that allowed free convection and radiation from the thermal mass to the room.

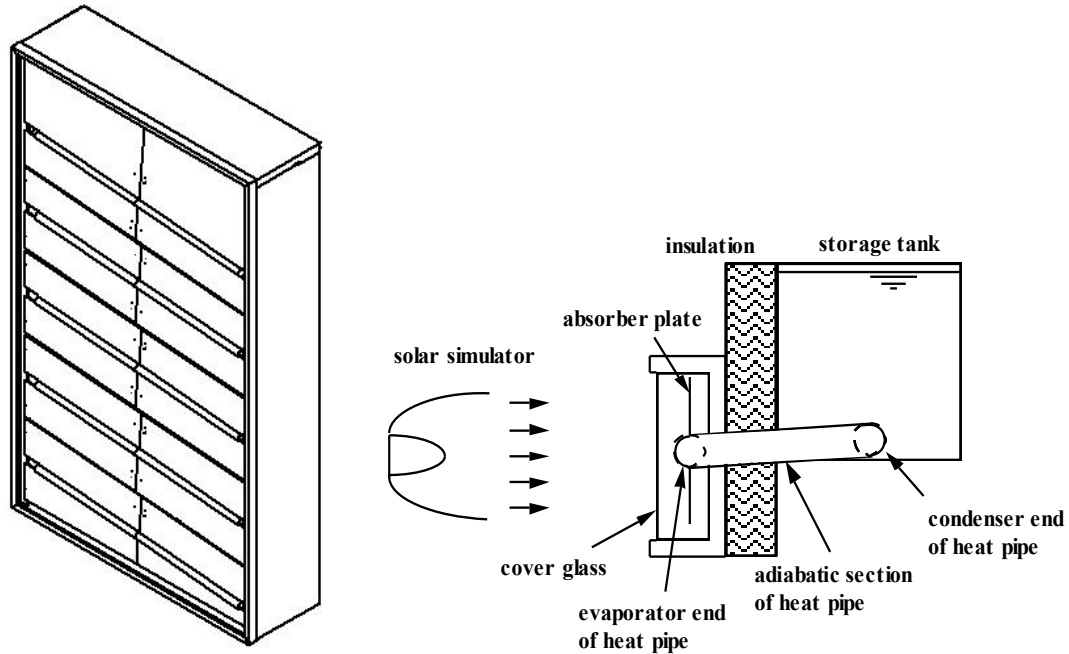


Figure 2.4. Left: isometric sketch of the prototype. On the front are the five slanted evaporator sections and absorber plates as seen through the cover glass. The interior components are not visible. Right: 2D schematic of one unit.

The 1.588 mm thick frame was 2.09 m tall x 1.25 m wide x 0.394 m deep and was constructed with a 0.0191 m wide mounting flange to seal around the glass glazing on the south side of the system. The 2.06 m (81 in.) x 1.22 m (48 in.) glazing consisted of 3.18 mm (1/8 inch) thick low-iron glass with an anti-reflective coating. The glazing edges were protected with a silicone rubber extrusion and were clamped into place using a front mounting flange along the outer edge of the frame.

The absorber plates of the unit consisted of 3.18 mm thick aluminum plated with black chrome over a nickel substrate. Semi-circular grooves were formed in the absorber

plates to receive the heat pipes. The outside edges of the absorber plates were mounted to the support frame with aluminum screws with insulating plastic spacers. The gap between the absorber plates and the glazing was 0.0254 m. The total receiving face of the absorber plates was 2.02 m (79½ in.) tall x 1.194 m (47 in.) wide.

The heat pipes were constructed from 0.0254 m (1 in.) inner diameter and 0.0286 m outer diameter copper pipes. The lengths of the evaporator, adiabatic and condenser sections were 1.16 m (45½ in.), 0.229 m (9 in.), and a 1.09 m (43 in.), respectively. All sections of the heat pipe were mounted at 5 degrees from the horizontal. A 6.35 mm diameter fitting for filling the heat pipes was formed in the adiabatic section.

Filling of the heat pipes was achieved using a charging system consisting of a vacuum pump, refrigerant tank, vacuum gauge, and several control valves. The entire charging system was drawn to a vacuum of 86.4 kPa (648 mmHg) with the vacuum pump. Each heat pipe was filled with 957 g of DuPont SUVA-124. This amount corresponded to a liquid volume of 120% of the evaporator section, as recommended by Albanese et al. [2012]. The heat pipes were glued into the grooves in the absorber plates with high thermal conductivity epoxy. In addition, 3.18 mm thick aluminum clamps, 1.09 m long x 0.102 m wide, held the heat pipes in place while the glue set, and were left in place.

Plastic tanks 1.11 m long x 0.356 m tall x 0.203 m thick (43½ in. x 14 in. x 8 in.) contained water as the thermal mass. A threaded bulkhead fitting on the end of the tank near the bottom allowed for the heat pipe entrance. Water capacity was 65.1 liters per tank. Total weight of the system was 487 kg, consisting of 326 kg of water and an installation or “dry” weight of 161 kg.

Insulation of the unit included 0.0508 m of mineral wool (RSI-1.41 K·m²/W, (R-8.0 h·ft²·°F/Btu)) next to the absorber plates to prevent outgassing in case of overheating, three layers of 0.0217 m Styrofoam (RSI-0.528 K·m²/W (R-3.0 h·ft²·°F/Btu) per panel), and 0.0254 m thick mineral wool pipe wrap was used around the adiabatic section of the heat pipes.

2.3.2 Instrumentation

Eight T-type thermocouples were placed in the center water tank, four each at two different depths, to assess stratification as well as temperature variations in the horizontal direction. Single thermocouples were placed in each of the other tanks. An additional thermocouple was placed in the room to measure room temperature. Two Kipp & Zonen CM3 solar pyranometers were used to measure insolation values, with one centered directly above the unit and the second directly below the unit. All data was collected using a National Instruments SCXI platform in conjunction with a low-voltage thermocouple-designed SCXI-1102 module. A SCXI-1600 analog to digital converter was used for the analog data inputs. LabVIEW software was used to sample and log the data at a sampling rate of 0.01667 Hz (one sample each minute). Hourly ambient temperature data was obtained from nearby Bernheim Arboretum and Research Forest.

2.3.3 Data Analysis

Data was collected and analyzed for January through April of 2010. Thermal efficiency of the system, η , was calculated by

$$\eta = \frac{\dot{Q}_u}{SA_c} \quad (2.1)$$

where \dot{Q}_u represents the useful gain transferred to the thermal mass by the heat pipe, S is the insolation received by the collector and A_c is the collector area. Days for which the hourly average radiation was less than 100 W/m^2 included hours in which \dot{Q}_u was negative, signifying rainy or very cloudy conditions, and were discarded from the analysis. All hourly values of \dot{Q}_u were positive during every day in which the hourly average radiation was greater than 100 W/m^2 .

An existing overhang caused shading on the prototype when the solar zenith angle, θ_z , was less than 48.2° , which occurred from February to October. When the system was shaded, insolation on the system was estimated by

$$S = xS_{diffuse} + (1-x)S_{total} \quad (2.2)$$

where x was the fraction of shading, and $S_{diffuse}$ was measured by the shaded upper pyranometer and S_{total} was measured by the unshaded lower pyranometer. The fraction of shading is given by

$$x = \frac{\frac{a}{\tan \theta_z} - b}{h} \quad (2.3)$$

where the horizontal overhang distance $a = 0.711 \text{ m}$ (28 in.), the vertical distance between the aperture and the overhang $b = 0.768 \text{ m}$ (30.25 in.), the aperture height $h = 2.02 \text{ m}$ (79.5 in.) and the solar zenith angle is

$$\theta_z = \cos^{-1}[\cos \phi \cos \delta \cos \omega + \sin \phi \sin \delta] \quad (2.4)$$

where the latitude is $\phi = 38.3^\circ$, δ is the declination and ω is the hour angle. The shading fraction during the period of analysis ranged from zero to 0.75.

To determine \dot{Q}_u , conservation of energy applied to the tank gives

$$\dot{Q}_u = \dot{Q}_s + \dot{Q}_{sr} \quad (2.5)$$

where \dot{Q}_s represents the rate of increase of energy in the thermal mass and \dot{Q}_{sr} is the rate of energy transfer from the tank to the room. \dot{Q}_s is

$$\dot{Q}_s = \frac{Mc_p \Delta T_s}{\Delta t} \quad (2.6)$$

where M is the mass of the water used for thermal storage, c_p is the specific heat of the water, and ΔT_s is the water temperature change during time interval Δt , which was one hour. \dot{Q}_{sr} is

$$\dot{Q}_{sr} = \frac{T_s - T_r}{R_{sr}} \quad (2.7)$$

where T_s and T_r are the average temperature during the hour for the water and room, respectively, and R_{sr} is the total thermal resistance from the thermal mass to the room air. Temperature in the room could not be controlled in these experiments, and varied according to the use of the room for classes and thermostat setbacks when the room was not in use. A thermal resistance network for R_{sr} is shown in Figure 2.5.

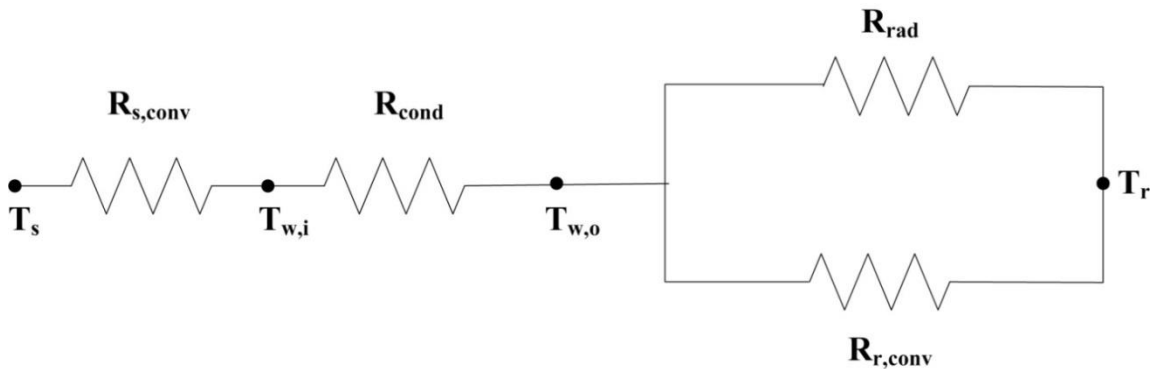


Figure 2.5. Thermal resistance network from the thermal mass to the room.

The network included convection on the inside surface of the tank wall, $R_{s,conv}$, conduction through the tank wall, R_{cond} , parallel radiation, R_{rad} , and convection, $R_{r,conv}$, from the wall of the tank to the room. Applying the resistance network shown in Figure 2.5, R_{sr} is

$$R_{sr} = R_{s,conv} + R_{cond} + \left(\frac{1}{R_{rad}} + \frac{1}{R_{r,conv}} \right)^{-1} \quad (2.8)$$

where $R_{s,conv}$ and $R_{r,conv}$, respectively, are

$$R_{s/r,conv} = \frac{1}{h_{s/r}A_s} \quad (2.9)$$

where A_s is the total heat transfer surface area of the tank wall(s) and the convection coefficient for water or air is

$$h_{s/r} = \frac{k_{s/r}Nu_{s/r}}{L} \quad (2.10)$$

where $k_{s/r}$ is the thermal conductivity for water or air, L is the tank wall height, and the Nusselt number, $Nu_{s/r}$ (developed for free convection from a vertical plate [Incropera & DeWitt, 2011]), for water or air is dependent on whether tank conditions are laminar or turbulent. Transition depended on the Rayleigh number

$$Ra_{s/r} = \frac{g\beta_{s/r}\Delta T_{sw/wr}L^3}{\nu_{s/r}\alpha_{s/r}} \quad (2.11)$$

where g is the acceleration due to gravity, $\beta_{s/r}$ is the volumetric thermal expansion coefficient for the water or air, $\nu_{s/r}$ is kinematic viscosity for water or air, $\alpha_{s/r}$ is thermal diffusivity for water or air, and the temperature difference between mediums is

$$\Delta T_{sw} = T_s - T_w \quad (2.12)$$

or

$$\Delta T_{wr} = T_w - T_r \quad (2.13)$$

where tank wall temperature, T_w , was approximated as the average temperature between the tank water and room air. For $Ra_{s/r} < 10^9$ (laminar), the Nusselt number is

$$Nu_{s/r} = 0.68 + \frac{0.67(Ra_{s/r})^{1/4}}{\left(1 + (0.492/Pr_{s/r})^{9/16}\right)^{4/9}} \quad (2.14)$$

where $Pr_{s/r}$ is the Prandtl number. When $Ra_{s/r} > 10^9$ (turbulent), the Nusselt number is

$$Nu_{s/r} = \left[0.825 + \frac{0.387(Ra_{s/r})^{1/6}}{\left(1 + (0.492/Pr_{s/r})^{9/16}\right)^{8/27}} \right]^2 \quad (2.15)$$

The conductive resistance through the tank wall is

$$R_{cond} = \frac{t_w}{k_w A_s} \quad (2.16)$$

where t_w is the tank wall thickness and k_w is the thermal conductivity of the tank wall.

Finally, the radiative resistance is

$$R_{rad} = \frac{1}{h_{rad} A_s} \quad (2.17)$$

where

$$h_{rad} = \varepsilon \sigma (T_w + T_r)(T_w^2 + T_r^2) \quad (2.18)$$

where ε is the radiative emissivity of the water tank wall and σ is the Stefan-Boltzmann constant.

The thermophysical properties of the water in the tank and the air in the room were determined by interpolation from thermophysical property tables [Incropera & DeWitt, 2011] at the average temperatures over the course of that hour. The volumetric thermal expansion coefficient β was also interpolated in the same manner for water, while β for air, assumed to be an ideal gas, was calculated using

$$\beta = \frac{1}{T_r} \quad (2.19)$$

Thermal diffusivity is

$$\alpha = \frac{k}{\rho c_p} \quad (2.20)$$

where ρ is the density. Kinematic viscosity is

$$\nu = \frac{\mu}{\rho} \quad (2.21)$$

where μ is the absolute viscosity. The mass of the water in each tank is

$$M = \rho V \quad (2.22)$$

where V is the volume of each tank.

Energy gain rates were calculated for each heating unit and summed to obtain total system gains to calculate system efficiency. To estimate the characteristic performance of the system for clear sky radiation normal to the aperture, a time constant for the collector was estimated by applying exponential curve fits to the decay in absorber temperature after sundown ($S \leq 0 \text{ W/m}^2$). Only nights with ambient temperature variation less than \pm

1.5 °C (from ASHRAE standard 93 [2010] for testing active solar collectors) and coefficient of determination (R^2) > 0.96 were included.

Efficiency versus loss potential to insolation ratio, $(T_s - T_a)/S$, was also calculated (where T_a is the ambient temperature.) Note that this ratio is similar to that used to determine a performance curve for an active solar collector, $(T_i - T_a)/S$, where T_i is the inlet temperature the active collector. Thermal storage temperature, T_s , is a close analog of inlet temperature to the absorber in this passive system. Conditions for these efficiency estimates were selected to conform as closely as possible to ASHRAE standard 93 [2010], including variations in insolation less than $\pm 32 \text{ W/m}^2$ for intervals of 10 minutes or two collector time constants, whichever is greater.

2.3.4 Error Propagation

System thermal efficiency (Equation 2.1) depended on measurements of storage and room temperatures (Equations 2.6 and 2.7) and of insolation. Therefore, the uncertainty in calculated system efficiency, μ_η , was found using

$$\mu_\eta = \sqrt{\left(\frac{\partial \eta}{\partial \Delta T_s} \mu_{\Delta T_s}\right)^2 + \left(\frac{\partial \eta}{\partial \Delta T_{sr}} \mu_{\Delta T_{sr}}\right)^2 + \left(\frac{\partial \eta}{\partial S} \mu_S\right)^2} \quad (2.23)$$

where ΔT_s is the storage temperature difference from Equation 2.6, and ΔT_{sr} is the temperature difference between storage and room ($T_s - T_r$) from Equation 2.7. The estimated uncertainty in system efficiency was $\pm 3.08\%$.

2.4. Chapter 2 Results

Hourly average insolation on the system SA_c , room gain \dot{Q}_{sr} , tank temperature, room temperature and ambient temperature are shown for two conditions in Figs. 2.6 and 2.7 to illustrate the range of system response. First, system response is shown for consecutive days (January 28 and 29) with high and low insolation, respectively, in Figure 2.6. January 28 (Julian hours 649-672) represented the best insolation during the heating season. The following day (Julian hours 673-696) had little insolation and was also the coldest day of the heating season. Tank temperature rose sharply to as high as 24 K (43 °F) above the room temperature on January 28, however on January 29, the gradual decline in tank temperature was continuous throughout the day, dropping to about 10 K (18 °F) above room temperature. The room gain followed this trend.

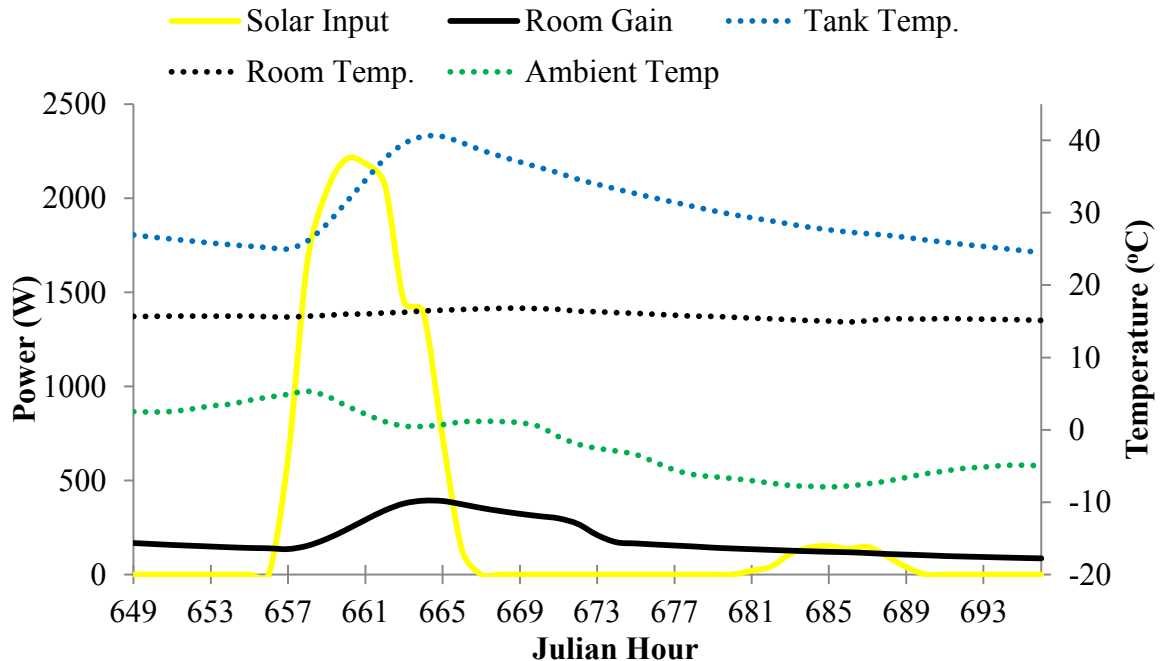


Figure 2.6. Average hourly values for insolation, room gain, and tank, room & ambient temperatures for January 28 & 29.

Second, the same hourly average powers and temperatures are shown for a series of five consecutive days with low insolation in Figure 2.7. These days followed four consecutive days of good insolation, thus the difference between tank and room temperatures began on the first day (February 22, Julian hours 1249 – 1272) at 13 K (23 °F). The gradual decline in this temperature difference is only slightly interrupted on February 22 and 23 (Julian hours 1273-1296), two days with very low insolation. For the following two days with low insolation, February 24 (Julian hours 1297-1320) and 25 (Julian hours 1321-1344), small gains occur sufficient to maintain the temperature difference above 5 K (9 °F). On February 26 (Julian hours 1345-1368), with peak hourly insolation on the unit exceeding 830 W/m^2 , the temperature difference was restored to 17 K (31 °F). Heat transfer to the room remained positive throughout this period, never dropping below 40 W.

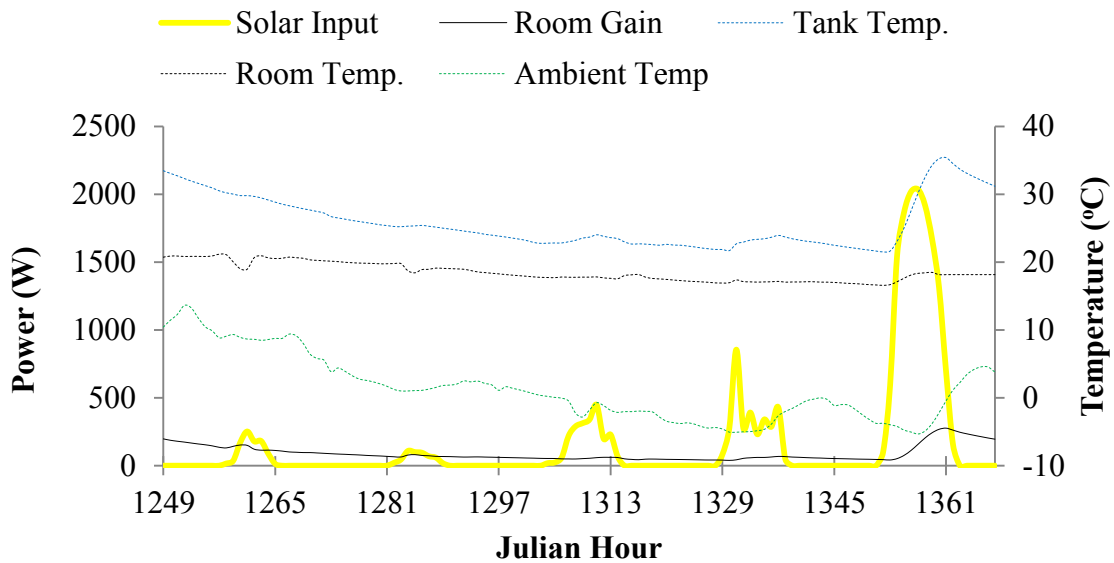


Figure 2.7. Average hourly values for system trends for February 22-26.

Hourly average useful gain per square meter of collector area versus hourly average solar input S for hours from 9 am to 5 pm, are shown in Figure 2.8. Peak system efficiencies were calculated for each day. The maximum daily peak efficiency calculated was 83.7%, and the average daily peak efficiency calculated was 61.4%. The maximum daily peak efficiency was achieved on February 8, an unusually warm day with an average ambient temperature of 21.4 °C (70.6 °F) versus an average storage temperature of 20.6 °C (69.1 °F). (Thus for these conditions, the absorber gained energy not only from insolation, but also from ambient air, which raises the potential for efficiencies defined in terms of the insolation source only (Equation 2.1) to be greater than 100%. Such conditions also frequently occur during the summer for domestic water heating and pool heating systems.) This was the only day during the heating season in which average ambient temperature exceeded average storage temperature.

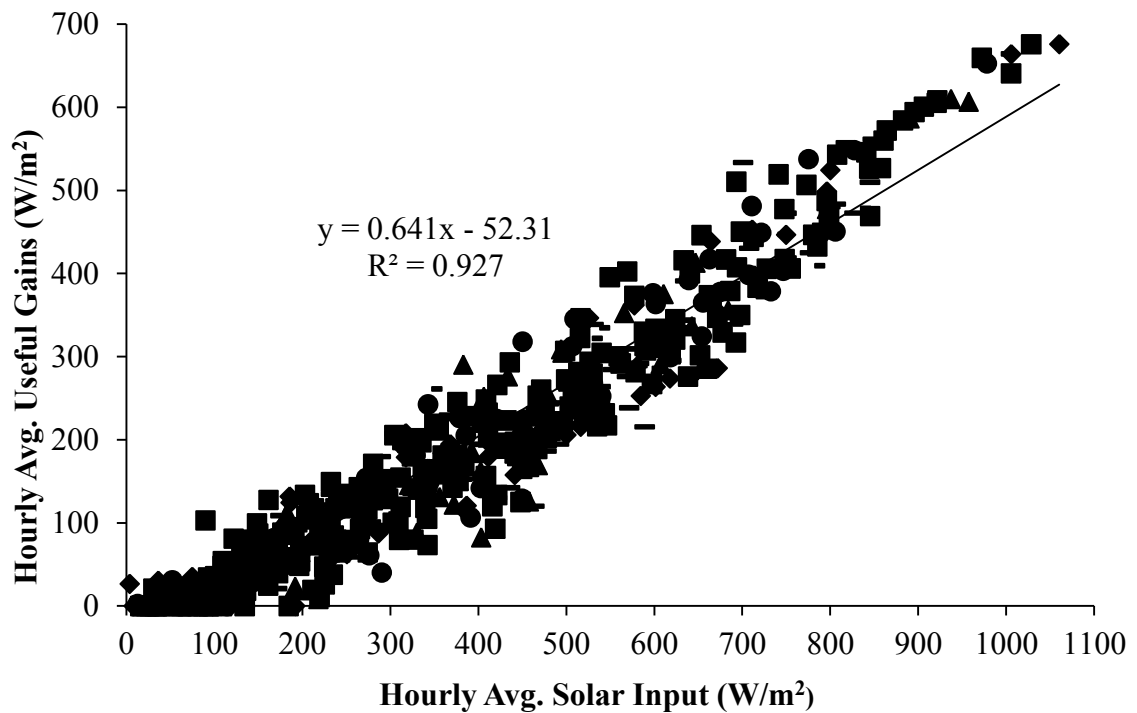


Figure 2.8. Plot of hourly average useful gains versus hourly average solar input from 9 am – 5 pm for each day of the selected heating season.

Collector efficiency is plotted in Figure 2.9 versus the ratio of the temperature difference between storage and ambient over absorbed insolation. Because the collector is nontracking, the ASHRAE 93 [2010] limit on insolation variation during two time constants (the collector time constant was calculated to be 90 min) could not be met. Fifty-minute intervals met all other ASHRAE 93 criteria and provided a reasonable number of samples for the plot. To meet the insolation variation limit, all samples were near solar noon. The curve fit implies a system efficiency of 74.1% when storage temperature equals ambient temperature. The angle of incidence of beam radiation on the system at solar noon varied from 31.7° (Jan. 13) to 62.7° (Apr. 18).

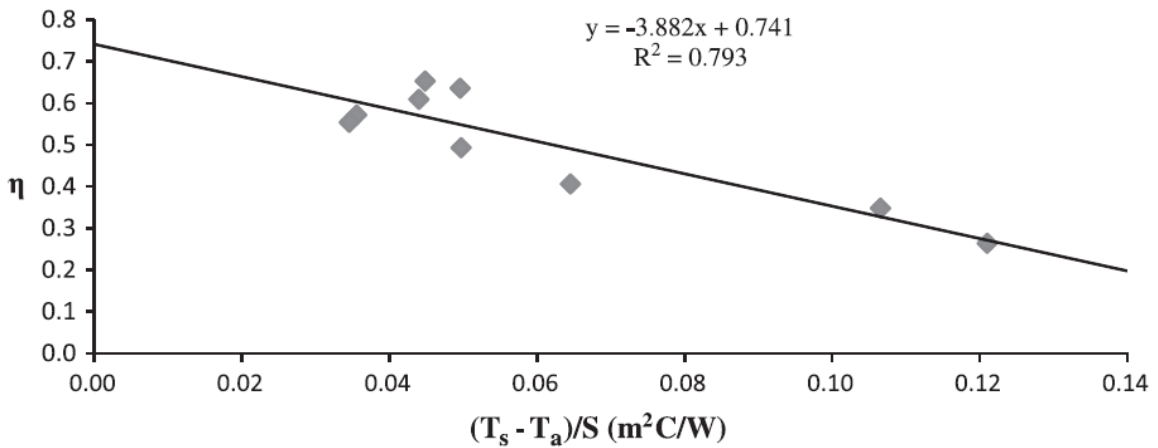


Figure 2.9. System efficiency versus loss potential/insolation ratio.

2.5. Chapter 2 Discussion

Even though the average ambient temperature was a cold 2 °C (36 °F) on January 28, the tank temperature still reached a peak hourly value of 41 °C (105 °F) (Figure 2.6) which highlights the effectiveness of solar energy collection and heat transfer of the heat pipe system. Room gains, which are primarily driven by the temperature difference

between the tank and room, reached 163 W/m^2 – the highest hourly average value during the heating season.

The sequence of four cloudy days in Figure 2.7 represents a near worst-case scenario for the period of data collection regarding available solar resource and system contributions to room heating. Yet for this sequence, small useful solar gains occurred, and room gain remained significant. Another sequence of three very cloudy days on February 27 – Mar 1 (not shown) caused tank temperature to come even closer to room temperature, decreasing room gain to near zero. Larger thermal capacity could bridge longer spans of unfavorable weather, but would seldom be required and would increase system cost. This tradeoff is typical for utilization of an intermittent energy resource to meet an unpredictable load and warrants scrutiny as a design parameter for a commercial product.

The trendline shown in Figure 2.8 suggests that useful gains will occur when solar input exceeds a mean of 83 W/m^2 . The slope of the trendline represents an asymptotic thermal efficiency of 64% compared to the calculated system average peak efficiency of 61.4%. While the coefficient of determination for the curve fit of this data is good, the threshold for utilizable insolation varies from zero to over 200 W/m^2 . In addition, useful gain varies by a factor of two or more for low insolation. This wide range is explained in part by the omission in this graph of the dependence of useful gains on ambient and absorber temperatures.

Figure 2.9 accounts for this temperature dependence in a way that is novel for passive solar systems, but is standard for active solar collectors. For a heat pipe, the temperature of the condensate entering the evaporator section is nearly equal to the storage

temperature. Thus storage temperature represents an accessible analog of collector inlet temperature, which makes the parameter on the abscissa of Figure 2.9 comparable to that used for active collectors. The intercept and slope of the trendline (0.741 and $-3.88\text{W/m}^2\text{K}$) are analogous to the heat removal factor * transmittance absorptance product $F_R(\tau\alpha)$ and heat removal factor * overall loss coefficient $F_R U_L$, respectively, for active collectors. These parameter values for the passive system compare favorably to average values for glazed liquid active collectors, which are $F_R(\tau\alpha) = 0.703$ and $F_R U_L = -4.74\text{ W/m}^2\text{K}$ [SRCC, 2012]. The incidence angle modifier, another standard index of active collector performance, could not be determined for the passive system because data was not available for low angles of incidence.

The time constant for the passive collector is considerably longer than that for active collectors, which typically ranges from 1 to 15 minutes. Several factors account for this, including the increased thermal capacity associated with additional collector material (3.18 mm thick aluminum absorbers plus the copper heat pipes), a higher specific heat for HCFC-124 than for water or antifreeze solutions, and additional enthalpy associated with latent heat of the phase change fluid.

Potential improvements to the experimental setup include testing in a facility where overhangs and shading can be eliminated, where the surface azimuth is perfectly south, and where room use and energy gains can be controlled. Improvements in system performance may also be possible with increased insulation between the thermal mass and the absorber, as well as by modifying the design of the frame to reduce losses to ambient and a less thermally-conductive material for the adiabatic section to eliminate losses from storage during cloudy and nighttime conditions.

CHAPTER 3: HEATING SEASON PERFORMANCE IMPROVEMENTS FOR A SOLAR HEAT PIPE SYSTEM

3.1. Chapter 3 Overview

An improved model of a heat pipe augmented passive solar space heating system was tested. Computer simulations showed that the new model, featuring key design modifications including a copper absorber, thicker insulation, a rubber adiabatic section, and one condenser exposed directly to room air, has significantly improved heat delivery to the room and reduced losses. The new prototype was tested alongside the previous prototype in a two-room passive solar test facility during January through February of 2013. Results showed that modifications implemented for the new model contributed to increased rate of useful thermal gains to thermal storage and to the room and decreased rate of thermal losses to ambient. Average daily peak efficiencies for the previous system and the new system were 80.7% and 85.0%, respectively. Furthermore, the average storage temperature for the new model, over the entire testing period, was 13.4% higher than that of the previous model; while the average room temperature over the same period was 24.6% greater for the new system. Simulations matched well with experimental data from the new prototype after parametric adjustments were made to the thermal capacitance of the room and conductances between evaporators and condensers, storage tank and room, solar wall insulation, and the load to collector ratio.

3.2. Chapter 3 Introduction

The heat pipe augmented solar wall (Figure 3.1) is a type of isolated gain passive space-heating system that significantly outperforms direct and indirect gain systems by taking advantage of the thermal diode effect of heat transfer in heat pipes [Corliss, 1979; Susheela & Sharp, 2001; Albanese et al., 2012; Robinson et al., 2013]. The heat pipe units operate by boiling fluid in the evaporator section connected to a solar absorber and condensing vapor in the condenser section within a thermal storage tank (Figure 3.2). Two-phase heat transfer in the heat pipe allows the system to operate with a small elevation difference so that the entire system can be installed in a south wall.

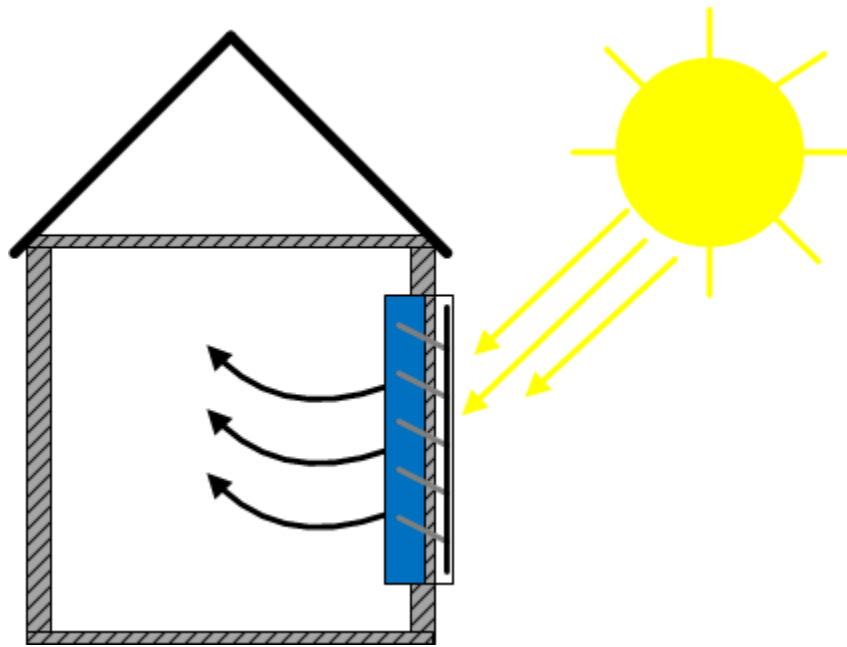


Figure 3.1. Schematic of full-scale heat pipe assisted solar wall prototype.

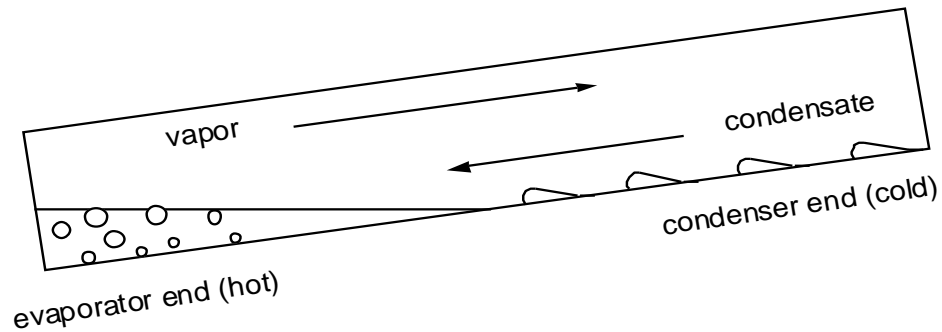


Figure 3.2. Schematic of heat pipe operation.

When the evaporator section is colder than the condenser section, the liquid heat transfer fluid remains in the evaporator and essentially no heat transfer takes place along the heat pipe. The result is low losses of heat flow away from the condenser. The large difference between forward and reverse heat transfer has caused heat pipes to be labeled as thermal diodes. Additionally, because of the effectiveness of boiling and condensing heat transfer, the heat pipe operates with small temperature gradients throughout. The result is extraordinary thermal conductance properties, with values 700 times greater than conduction in copper being reported [Dunn, 1994].

A full-scale heat pipe system that could be retrofitted onto existing walls was designed and tested by Susheela and Sharp [2001] with system efficiencies ranging from 60-80% during sunny days. A bench-scale experimental model was tested by Albanese, et al. [2012], primarily based on design improvements recommended by Susheela and Sharp. A low-iron glass cover, a high-performance selective absorber surface, and a refrigerant fill level of 120% of the evaporator volume resulted in the highest average system thermal efficiency of 85%.

Robinson, et al. [2013] continued the research of Albanese, et al. by testing a full-scale experimental prototype of similar design. The unit consisted of five individual heating units, each containing an absorber plate, heat pipe and storage tank (Figure 3.1).

The absorber material was aluminum coated with a black chrome selective surface, the heat pipes were 1 inch nominal diameter copper tubes, and each storage tank contained approximately 17 gallons of water. A maximum daily peak thermal efficiency of 83.7% and average daily peak thermal efficiency of 63.4% were measured. On cold, sunny days, the thermal storage was heated to temperatures well above the threshold for providing significant energy to the room. It was observed that useful gains typically commenced two to three hours after sunrise. The longest consecutive period of significant daytime cloud coverage was four days, yet heat delivery to the room from storage remained positive and was never less than 40 Watts. For sunny days following any period of cloudy days, thermal storage temperatures were quickly restored to levels observed prior to the onset of the low-insolation period. Undesirable characteristics of the testing site included a surface azimuth 10° east of south, an existing overhang and side protrusion shading the absorbers at times during the testing period, and no independent control of room temperature (an auxiliary heater provided additional internal gains to the room).

Based on these results, computer simulations were used to model significant modifications to the Robinson, et al. [2013] prototype, and an improved full-scale prototype was designed and constructed. In addition, a passive solar test facility, designed to provide better testing conditions, was constructed on the campus of the University of Louisville. The facility consisted of two 12' by 12' rooms, with the previous full-scale model [Robinson, et al. 2013] and the new design installed in each room, respectively. This paper will compare the performance of the two systems tested under identical conditions during January and February of 2013.

3.3. Chapter 3 Methods

3.3.1 Computer Modeling

A thermal network approach was used, similar to Albanese et al. [2012], who adapted the methods of Susheela and Sharp [2001] and Corliss [1979]. The thermal network for the heat pipe system with all condenser sections immersed in water tanks is shown in Figure 3.3.

The heat transfer rate \dot{q}_{ij} per unit of collector area between nodes i and j is given by

$$\dot{q}_{ij} = k_{ij}(T_j - T_i) \quad (3.1)$$

where k_{ij} is the heat transfer coefficient between nodal temperatures T_j and T_i , respectively. The energy balance equation for the i^{th} node is

$$m_i \frac{dT_i}{dt} = \sum_j [k_{ij}(T_j - T_i)] + S_i \quad (3.2)$$

where m_i is the capacitance (product of the mass of the node and its specific heat) per unit collector area, S_i is the solar power received per unit collector area at node 1 (Figure 3.3), and t is time. Using a central difference discretization scheme over time step Δt , Equation 3.2 becomes

$$\left(\frac{2m_i}{\Delta t} + \sum_j k_{ij} \right) T_i - \sum_j (k_{ij} T_j) = \frac{2m_i T_{io}}{\Delta t} + \sum_j [k_{ij}(T_{jo} - T_{io})] + (S_i + S_{io}) \quad (3.3)$$

where the zero subscript denotes the previous time step. All nodes were simultaneously solved as a function of time from a set of initialized temperatures and using Typical Meteorological Year weather data (TMY3). For heat transfer coefficients dependent on nodal temperatures, iterations were used accordingly. Room nodal temperature was

restricted, to simulate auxiliary heating and venting, within a defined room comfort range of 18.33 to 23.9°C (65 to 75°F).

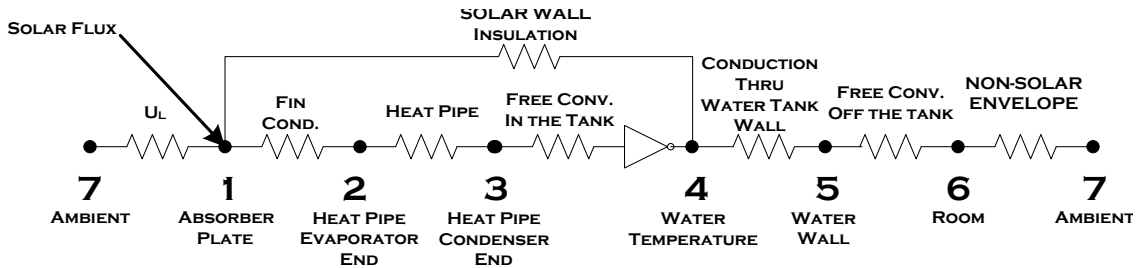


Figure 3.3. Thermal network for the heat pipe assisted solar wall.

The potential to provide increased heat to the room during early-morning hours was investigated by modifying the heat pipe system so that one or more condensers were exposed directly to room air. This change provided a quicker transient response at the onset of insolation, for early morning energy transfer from the absorbers directly to the room when outdoor temperature is typically low and thermal mass has been depleted. To simulate the free condenser, a conductance was added between the condenser end of the heat pipe and the room (Figure 3.4). The conductance between the condenser and the water, the mass of the water and the conductances through the tank wall and to the room were all decreased to represent the fewer number of tanks.

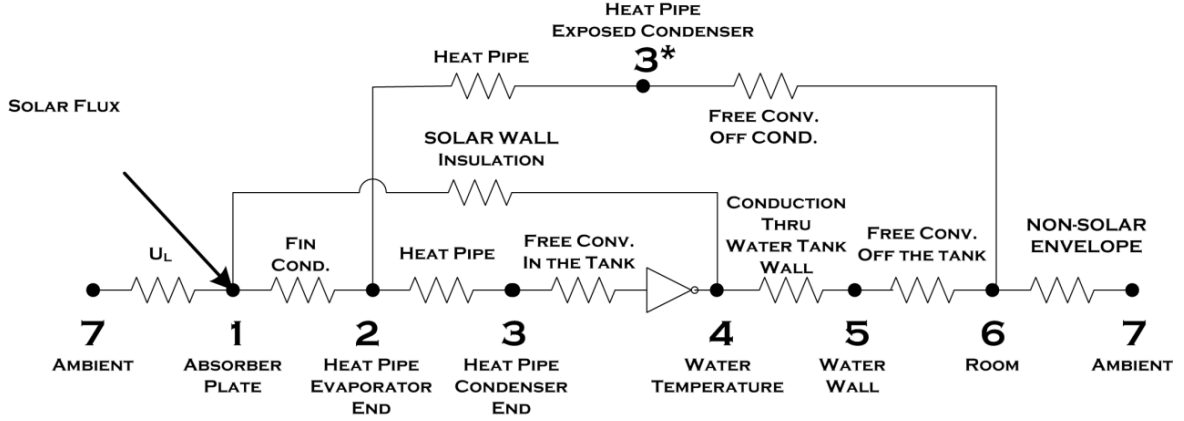


Figure 3.4. Thermal network for the heat pipe assisted solar wall with one or more condensers exposed directly to room air.

The heat transfer from the exposed condenser to room air was represented by a free convection Nusselt number for a heated tube [Incropera & Dewitt, 2011]

$$Nu_D = \left[0.60 + \frac{0.387 Ra_D^{1/6}}{\left(1 + (0.559 / Pr_r)^{9/16}\right)^{8/27}} \right]^2 \quad (3.4)$$

where Pr_r is the Prandtl number and the Rayleigh number is [Incropera & Dewitt, 2011]

$$Ra_D = \frac{g\beta(T_3 - T_6)D^3}{\nu\alpha} \quad (3.5)$$

where g is the acceleration due to gravity, β is the volumetric coefficient of thermal expansion for the room air (taken as the inverse of the film temperature between the condenser and room), D is the outside diameter of the condenser, ν is the kinematic viscosity, α is the thermal diffusivity, and T_3 and T_6 are the temperatures of the condenser and room, respectively (Figure 3.4). Using the Nusselt number of Equation 3.4, the normalized heat transfer coefficient, k_{3*6} , between the exposed condenser and room air was

$$k_{3*6} = N_{exp} \left(\frac{Nu_D k_r}{D} \right) \frac{A_{cond}}{A_c} \quad (3.6)$$

where N_{exp} is the number of condensers exposed directly to room air, k_r the thermal conductivity of the room air, A_{cond} is the condenser area, and A_c is the collector area. Thermal conductance values for the networks shown in Figures 3.3 and 3.4 are provided in Table 3.1. All conductance values are normalized by the collector area.

Table 3.1. Description of thermal conductance values used for heat pipe wall thermal network models.

Conductance Value (W/m ² K)	Description
k_{71}	Overall collector loss coefficient
k_{12}	Absorber fin conduction to the working fluid
k_{23} and k_{23*}	Fluid heat transfer from evaporator to condenser, thermal conduction through heat pipe wall & insulated wall - when $T_1 > T_4$ for condenser in storage and $T_1 > T_6$ for condenser in room air
k_{41}	Thermal conduction through heat pipe wall and insulated wall - when $T_1 < T_4$
k_{34}	Convection between condenser and storage water
k_{3*6}	Convection between condenser and room air
k_{45}	Conduction through water tank wall
k_{56}	Convection between tank wall and room
k_{67}	System Load-to-Collector Ratio (LCR)

Key parameters used for the simulations were a load to collector ratio (the ratio of the UA value for the space to the collector area; conductance k_{67} in Figures 3.3 and 3.4, and Table 3.1) of LCR = 10 W/m²K and a defined room comfort temperature range of 18.3°C to 23.9°C (65 °F to 75 °F). All additional baseline parameters and calculated thermal network heat transfer coefficients were identical to Albanese, et al. [2012].

Annual heating load per unit collector area, $q_{a,hl}$, was

$$q_{a,hl} = \sum_{year} k_{67}(T_b - T_7)^+ \Delta t \quad (3.7)$$

when ambient temperature (T_7) was below the commonly used base temperature (T_b) of 18.33°C (65°F), and was zero otherwise. Annual auxiliary heating load per unit collector area, $q_{a,aux}$, was

$$q_{a,aux} = \sum_{year} \left[k_{67}(T_6 - T_7) - k_{56}(T_5 - T_6)^+ - k_{3*6}(T_{3*} - T_6)^+ \right] \Delta t \quad (3.8)$$

when ambient temperature was less than room temperature ($T_7 < T_6$), and room temperature dropped to the lower comfort limit ($T_6 = 18.3^\circ\text{C}$). The asterisk superscript for T_3 in the third term (within the summation brackets) denotes only the temperature of condenser(s) directly exposed to room air. The second and third term on the right hand side of Equation 3.8 (within the summation brackets) represents the contribution from the heat pipe system to serving the heating load, and the difference between these terms and the first term (which is different from the heating load in that room temperature T_6 may exceed T_b) represents the auxiliary requirement. The calculated auxiliary heat was added during each time step to maintain the room at the lower comfort limit. System solar fraction, SF , represents the percentage of the annual heating load that is served by the heat pipe system

$$SF = 1 - \frac{q_{a,aux}}{q_{a,hl}} \quad (3.9)$$

3.3.2 Passive Solar Test Facility (PSTF)

The 12' by 24' facility is divided into two identical 12' by 12' rooms to allow two systems to be compared side-by-side under the same weather conditions. Structural

insulated panels (SIPs) were used for the building envelope, 12” thick panels with an R-value of 7.93 m²*K/W (45 ft²F*hr/Btu) for the floor and walls, and 16” for the roof with an insulating value of 11.10 m²*K/W (R-63). A 12” thick panel separates the two rooms. To reduce infiltration, all joints between panels were caulked on both the interior and exterior. Rough openings in the south wall were provided to accommodate passive solar systems. The overhang above the south openings is short to eliminate shading during the heating season. An image of the south wall of the building with the previous prototype in the west room and the new prototype in the east room is shown in Figure 3.5.



Figure 3.5. South view of the passive solar test facility. The collector for the previous prototype can be seen on the west (left) side of the wall, and the collector for the new prototype is on the east (right) side.

Doors were installed on the east and west for access to the rooms. A 39" by 27" four-pane window of $1.7 \text{ m}^2 \cdot \text{K}/\text{W}$ (R-9) was installed on the north side of each room for ventilation and emergency egress. Two 15" by 39" four-pane windows were installed in the clerestory section of each room for ventilation and daylighting. The overhang of the roof above the clerestory windows allows beam insolation to enter the windows during the winter months (October through April) and shades them during the summer. These windows were covered with an opaque material to eliminate additional solar gains during tests of the heat pipe systems. Electricity was supplied to the building for powering data acquisition hardware only. No auxiliary heating was supplied to the rooms.

The overall building heat loss coefficient (UA) was calculated from the rated loss coefficients for the components of the envelope and from measured infiltration using a blower door test apparatus. The number of air changes per hour (ACH) was found in accordance with ASTM International Standard E-779 [2010]. Half the overall UA was assigned to each system. Heat exchange between the two rooms through the interior wall was neglected (further supporting information is in Section 3.4.2.).

3.3.3 Heat Pipe System Modifications

A schematic highlighting significant design modifications made to the new prototype is shown in Figure 3.6. Compared to the previous prototype (Figure 3.1) [Robinson et al. 2013], the new design included copper absorbers soldered to the evaporator sections, instead of aluminum absorbers bonded with epoxy, reducing thermal resistance between the absorbers and evaporators. A new glass cover was used with improved solar transmittance at normal incidence of 93%, versus 89% for the previous system. While the thermal diode effect prevents heat transfer by convection within the heat pipes when the

condenser is warmer than the evaporator, conduction along the copper adiabatic section accounted for 39% of thermal losses between the absorber and storage for the previous design [Robinson et al. 2013]. Replacing the copper (thermal conductance of 401 W/m*K) adiabatic sections with DPM rubber (0.06 W/m*K) decreased this source of thermal bridging by 99.98%. The adiabatic sections were also extended to allow 12” of insulation (the same as the SIPS panels) between the absorber and storage. The previous unit had 3.5” of insulation.

In the new prototype, one of the five condenser sections was exposed directly to room air to increase heating of the room during early-morning hours. All other design parameters, including heat pipe, working fluid, and storage tank dimensions and materials were identical to the previous model [Robinson et al. 2013].

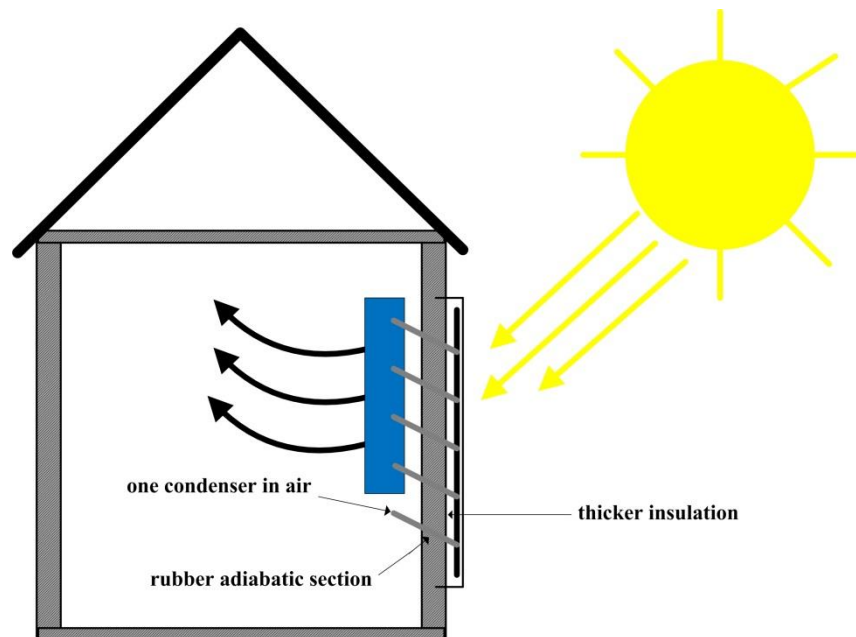


Figure 3.6. Schematic of a new model of the heat pipe wall prototype highlighting significant design modifications of the previous model.

3.3.4 Instrumentation

A data acquisition system was placed in each room of the solar test facility. A National Instruments chassis was used in conjunction with an SCXI 1600 16 bit digitizer and an SCXI 1102B isolation amplifier with an SCXI 1303 thermocouple module. LabVIEW software was used to log the data at a sampling rate of 0.01667 Hz (once every minute). Two pyranometers were mounted between the south wall openings, one aligned with the top and the other with the bottom of the openings.

For each prototype, four T-type thermocouples were placed on the central absorber, three on each central evaporator, and two inside each individual storage tank. Additional placement of thermocouples included one attached to each tank wall to measure tank surface temperature, two placed in each room to measure room temperature, and two placed outside to measure ambient air temperature. The new prototype contained an additional two thermocouples placed on the exposed condenser.

3.3.5 Data Analysis

Data was collected and analyzed for the new prototype from January through February of 2013. All measured temperatures were averaged over hourly intervals. Thermal efficiency of the system, η , was calculated using

$$\eta = \frac{\dot{Q}_u}{SA_c} \quad (3.10)$$

where S is the solar power received by the collector per unit area and \dot{Q}_u is the useful power delivered by the heat pipes to storage and to the room. For each prototype, power

was calculated for each heating unit, whether to a storage tank or the single condenser directly exposed to air. Thus, the total useful power for each system is

$$\dot{Q}_u = \sum \dot{Q}_s + \sum \dot{Q}_{out} \quad (3.11)$$

where \dot{Q}_s represents the net power to the storage tank and \dot{Q}_{out} is the power transfer from the storage tanks (and exposed condenser for the new model) to the room. Days for which \dot{Q}_u was negative between 9am and 5pm signified cloudy conditions, and were discarded from the analysis. \dot{Q}_s is

$$\dot{Q}_s = \frac{Mc_p \Delta T_s}{\Delta t} \quad (3.12)$$

where M is the mass of the water in the storage tank, c_p is the specific heat of the water, and ΔT_s is the water temperature change during the one hour time interval Δt . For heating units utilizing a storage tank, \dot{Q}_{out} is

$$\dot{Q}_{out} = \frac{T_s - T_r}{R_{sr}} \quad (3.13)$$

where T_s and T_r are the temperatures for the water and room, respectively, and R_{sr} is the total thermal resistance from the thermal mass to the room air. A thermal resistance network for R_{sr} is shown in Figure 3.7.

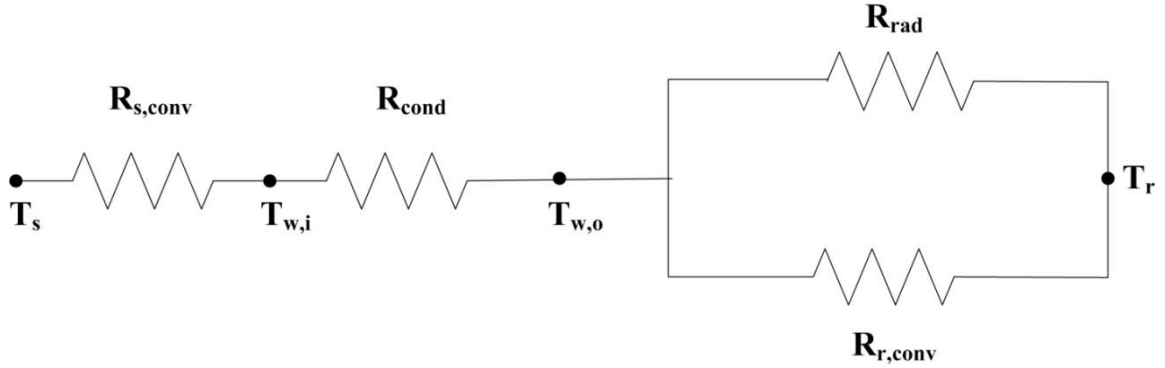


Figure 3.7. Thermal resistance network used to calculate \dot{Q}_{out} for heating units with a thermal storage tank.

The network included convective heat transfer to the inside surface of the tank wall, $R_{s,conv}$, conduction through the tank wall, R_{cond} , parallel radiation, R_{rad} , and convection, $R_{r,conv}$, from the wall of the tank to the room. Applying the resistance network shown in Figure 3.7, R_{sr} is

$$R_{sr} = R_{s,conv} + R_{cond} + \left(\frac{1}{R_{rad}} + \frac{1}{R_{r,conv}} \right)^{-1} \quad (3.14)$$

where $R_{s,conv}$ and $R_{r,conv}$, respectively, are

$$R_{s/r,conv} = \frac{1}{h_{s/r,conv} A_s} \quad (3.15)$$

where A_s is the total heat transfer surface area of each tank exposed to room air, and the convection coefficient for water or air is

$$h_{s/r} = \frac{k_{s/r} Nu_{s/r}}{L} \quad (3.16)$$

where $k_{s/r}$ is the thermal conductivity for water or air, L is the tank wall height, and the Nusselt number, $Nu_{s/r}$ (developed for free convection from a vertical plate [Incropera &

DeWitt, 2011]), for water or air is dependent on whether convection conditions are laminar or turbulent. For laminar flow, the Nusselt number is

$$Nu_{s/r} = 0.68 + \frac{0.67 Ra_{s,r}^{1/4}}{\left(1 + (0.492 / Pr_{s,r})^{9/16}\right)^{4/9}} \quad (3.17)$$

where $Pr_{s/r}$ is the Prandtl number. For turbulent conditions, the Nusselt number is

$$Nu_{s/r} = \left[0.825 + \frac{0.387 (Ra_{s/r})^{1/6}}{\left(1 + (0.492 / Pr_{s/r})^{9/16}\right)^{8/27}} \right]^2 \quad (3.18)$$

Laminar to turbulent transition depends on the Rayleigh number

$$Ra_{s/r} = \frac{g \beta_{s/r} \Delta T_{sw/wr} L^3}{\nu_{s/r} \alpha_{s/r}} \quad (3.19)$$

where g is the acceleration due to gravity, $\beta_{s/r}$ is the volumetric thermal expansion coefficient for the water or air, $\nu_{s/r}$ is kinematic viscosity for water or air, and $\alpha_{s/r}$ is thermal diffusivity for water or air, and the temperature difference between mediums is

$$\Delta T_{sw} = T_s - T_w \quad (3.20)$$

or

$$\Delta T_{wr} = T_w - T_r \quad (3.21)$$

where T_w is the tank wall temperature. For $Ra_{s/r} < 10^9$, free stream conditions are laminar and when $Ra_{s/r} > 10^9$ they are turbulent.

The conductive resistance through the tank wall is

$$R_{cond} = \frac{t_w}{k_w A_s} \quad (3.22)$$

where t_w is the tank wall thickness and k_w is the thermal conductivity of the tank wall. Finally, the radiative resistance is

$$R_{rad} = \frac{1}{h_{rad}A_s} \quad (3.23)$$

where

$$h_{rad} = \varepsilon\sigma(T_w + T_r)(T_w^2 + T_r^2) \quad (3.24)$$

where ε is the radiative emissivity of the water tank wall and σ is the Stefan-Boltzmann constant.

For a condenser exposed directly to room air, \dot{Q}_{out} is

$$\dot{Q}_{out} = \frac{T_{cnds r} - T_r}{R_{cnds r}} \quad (3.25)$$

where $T_{cnds r}$ is the temperature of the exposed condenser and the thermal resistance network for $R_{cnds r}$ is shown in Figure 3.8.

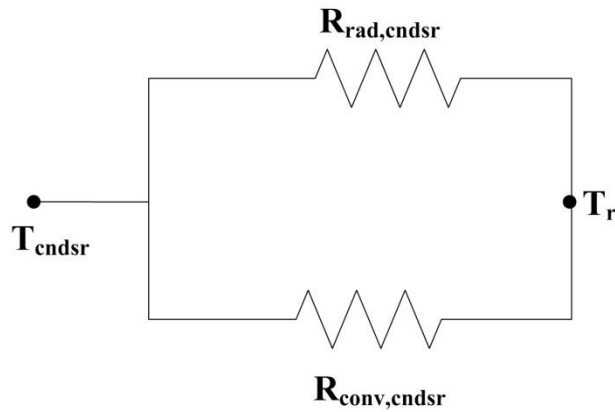


Figure 3.8. Thermal resistance network used to calculate \dot{Q}_{out} for a heating unit with the condenser exposed directly to room air.

Applying the resistance network shown in Figure 3.8, $R_{cnds r}$ is

$$R_{cnds r} = \left(\frac{1}{R_{rad,cnds r}} + \frac{1}{R_{conv,cnds r}} \right)^{-1} \quad (3.26)$$

where $R_{conv,cnds r}$ is

$$R_{conv,cnds r} = \frac{1}{h_{cnds r} A_{cnds r}} \quad (3.27)$$

where $A_{cnds r}$ is the surface area of the condenser and $h_{cnds r}$ is

$$h_{cnds r} = \frac{k_r Nu_D}{D} \quad (3.28)$$

The radiative resistance from the condenser and the radiative heat transfer coefficient are

$$R_{rad,cnds r} = \frac{1}{h_{rad,cnds r} A_{cnds r}} \quad (3.29)$$

and

$$h_{rad,cnds r} = \varepsilon_{cnds r} \sigma (T_{cnds r} + T_r) (T_{cnds r}^2 + T_r^2) \quad (3.30)$$

where $\varepsilon_{cnds r}$ is the radiative emissivity of the copper condenser. The properties of the water in the tank and the air in the room were determined by interpolation from thermophysical property tables [Incropera & DeWitt, 2011] at the average tank and room temperature(s) over the course of that hour.

Efficiency versus loss potential to insolation ratio, $(T_s - T_a)/S$, for the new system was also calculated (where T_a is the ambient temperature.) Conditions were determined in the same manner as Robinson et al. [2013] and were selected to conform as closely as possible to ASHRAE standard 93 [2010]. Because of the additional enthalpy associated

with latent heat of the phase change fluid, a higher specific heat for the fluid (versus typically used water or antifreeze solutions), and the additional thermal capacity of the collectors, the time constant for these passive systems was much larger than those for active systems. Thus ASHRAE 93 criterion that requires that insolation varies no more than $\pm 32 \text{ W/m}^2$ over intervals of 10 minutes or two collector time constants – whichever is greater – could not be met. However, using two-hour intervals centered around solar noon, variation in insolation was limited to no more than 32 W/m^2 per 10 minutes and incidence angles were also lowest.

3.3.6 Error Propagation

System efficiency (Equation 3.10) depends on measurements of storage, room and condenser temperatures (Equation 3.11 with Equations 3.12, 3.13 and 3.25) and of insolation. In addition, each of these measurements is subject to digitization error by the data acquisition system. Therefore, the uncertainty in calculated system efficiency, μ_η , was found using

$$\mu_\eta = \sqrt{\left(\frac{\partial \eta}{\partial \Delta T_A} \mu_{\Delta T_A}\right)^2 + \left(\frac{\partial \eta}{\partial \Delta T_B} \mu_{\Delta T_B}\right)^2 + \left(\frac{\partial \eta}{\partial \Delta T_C} \mu_{\Delta T_C}\right)^2 + \left(\frac{\partial \eta}{\partial S} \mu_S\right)^2} \quad (3.31)$$

where ΔT_A is the storage temperature difference (ΔT_s) from Equation 3.12, ΔT_B is the temperature difference between storage and room ($T_s - T_r$) from Equation 3.13, ΔT_C is the temperature difference between the exposed condenser and room ($T_{cnds} - T_r$) from Equation 3.25, and μ represents the uncertainty in temperature and insolation measurements, respectively.

For any arbitrary value of $\Delta T = T_1 - T_2$, we have

$$\left(\frac{\partial \Delta T}{\partial T_1}\right)^2 = \left(\frac{\partial \Delta T}{\partial T_2}\right)^2 = 1 \quad (3.32)$$

therefore the uncertainty for any ΔT is

$$\mu_{\Delta T, digit/tc} = \sqrt{\left(\frac{\partial \Delta T}{\partial T_1} \mu_{T_1}\right)^2 + \left(\frac{\partial \Delta T}{\partial T_2} \mu_{T_2}\right)^2} = \sqrt{2\mu_T^2} = \sqrt{2}\mu_{digit/tc} \quad (3.33)$$

where μ_{digit} is the digitization error in each temperature measurement, which for the SCXI-1600 and SCXI-1102 modules was ± 0.027 K/level, and thermocouple uncertainty, μ_{tc} , is roughly 0.1 K up to approximately 100°C [Ripple et al., 1994]. Thus

$$\mu_{\Delta T_A} = \mu_{\Delta T_B} = \mu_{\Delta T_C} = \sqrt{\mu_{\Delta T,tc}^2 + \mu_{\Delta T,digit}^2} \quad (3.34)$$

resulting in an overall uncertainty in temperature measurement of 0.146 K.

The pyranometers have an overall error of $\pm 3\%$ of the measured value, as specified by the manufacturer Kipp and Zonen. Accordingly, the maximum μ_η occurred at the maximum value of insolation measured during the testing period - equal to 934.5 W/m² and resulting in a maximum μ_S of 28.04 W/m². Values for each respective derivative from Equation 3.32 are shown in Table 3.2. The derivative associated with \dot{Q}_{st} represented the greatest uncertainty and the derivative associated with pyranometer measurement (insolation) represented the least uncertainty. The estimated uncertainty in system efficiency from Equation 3.31 was $\pm 3.50\%$.

Table 3.2. Value for each derivative associated with overall uncertainty in calculated system efficiency.

Derivative	Value
$\partial\eta / \partial\Delta T_A$	0.2190
$\partial\eta / \partial\Delta T_B$	0.0012
$\partial\eta / \partial\Delta T_C$	0.0018
$\partial\eta / \partial\Delta S$	0.0005

3.3.7 Matching Simulations to Full-scale Performance

To provide partial confirmation of computer simulations and acquire a better understanding of the full-scale PSTF prototype performance, simulation variables were adjusted to match the temperature trends obtained by the prototype over a 72-hour period from January 5 – 7. This period consisted of two sunny days (January 5 and 7) with a cloudy day in between (January 6). Initial modifications to the baseline algorithms consisted of matching dimensional parameters to those of the prototype and PSTF, including absorber, evaporator, condenser, adiabatic and tank dimensions, solar wall insulation materials and thicknesses, and an LCR equivalent to its calculated value. Additionally, since baseline simulations only accounted for the capacitance (product of the material specific heat and mass) of the water storage (node 4 in Figure 3.4), the effects of capacitance for additional nodes were evaluated. Initial capacitance added for the thermal mass in the room (node 6) consisted of the room air and OSB sheathing for the walls, floor and roof. This capacitance was increased from the initial value to achieve matching.

The overall collector loss coefficient, k_{71} , (Figure 3.4, Table 3.1) is sensitive to forced convection due to wind velocity. Since wind speed was not measured during experimentation, k_{71} could not be effectively calculated; thus measured temperatures - for each hour during the 72-hour period - for the prototype absorber (node 1 in Figure 3.4) were imported into the matching simulations. Since certain nodal conductances in the thermal model were calculated based on well-established, empirically-validated correlations and formulas, these values were left unchanged, including absorber fin conduction k_{12} , condenser-to-water convection k_{34} , and water wall conduction k_{45} . The remaining parameters had lower certainty in their values and were adjusted accordingly for matching.

The parameters adjusted included the capacitance of the room and the conductances for: working fluid heat transfer from the evaporator to condenser k_{23} , conduction through the solar wall k_{41} , heat transfer from the tank wall to the room k_{56} , and the LCR (k_{67}). These values were adjusted until the average difference in temperature, over the 72-hour period, between simulated and experimental values for the evaporators, tanks, and room were less than or equal to 0.5 K.

3.4. Chapter 3 Results & Discussion

3.4.1. Computer Simulations

The annual solar fraction for the previous system and the effect that each significant modification for the new system had on solar fraction is shown in Figure 3.9. The higher thermal conductivity for copper over aluminum resulted in a slight increase in solar fraction by 0.50%. The thicker wall reduced thermal losses from both storage and room to the cold ambient air, increasing solar fraction by an additional 4.92%. Reductions in

thermal bridging created by the rubber adiabatic section resulted in the greatest increase in solar fraction by an additional 5.32%. The total improvement for all three changes was 10.7%

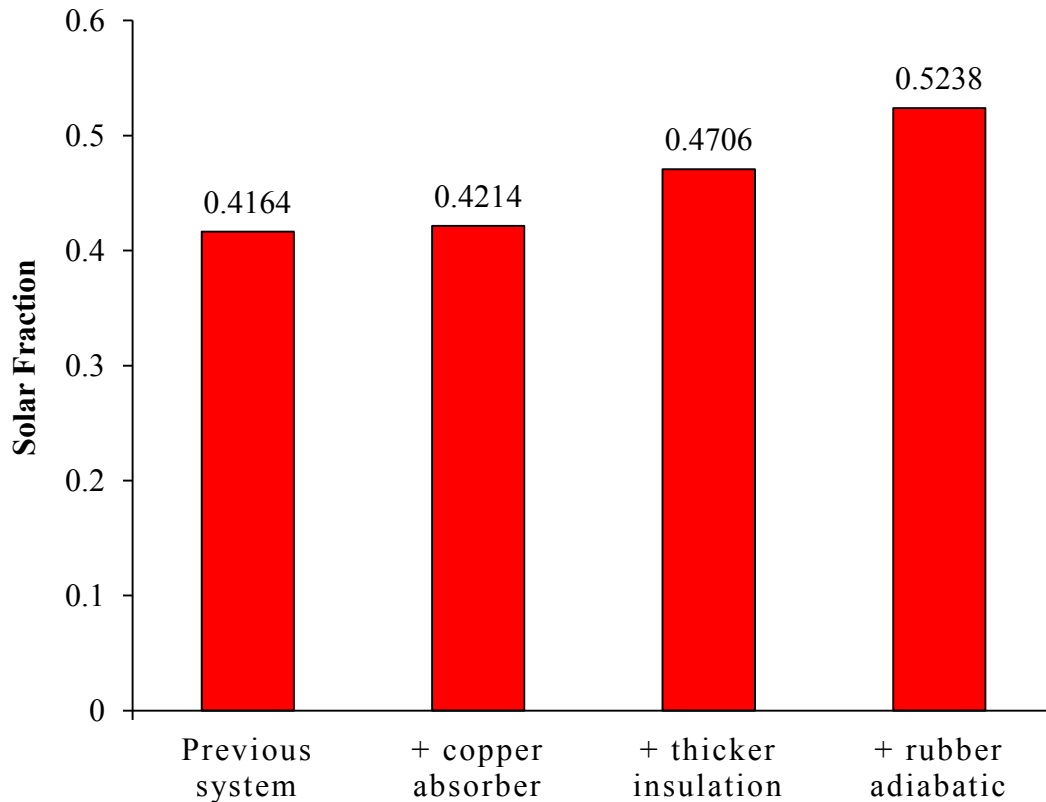


Figure 3.9. Solar fraction for the previous prototype and modifications implemented for the new prototype.

A plot of solar fraction for each hour of the day for January 15 (in Louisville, KY) for systems with (1) all five unit condensers inside the thermal mass storage tanks, (2) four condensers in tanks and one exposed directly to air, and (3) three condensers in tanks and two exposed directly to air, is shown in Figure 3.10. Exposing one or two condensers to room air increased the solar fraction in the morning more rapidly than the system with all condensers in tanks. However, the system with one condenser exposed to room air

delivered more heat to the room in the early evening hours than either of the other two systems. Because of its smaller thermal capacity, the system with four tanks lost solar fraction during the night at a greater rate, and by morning, its contribution was approximately the same as the baseline system. Simulations also confirmed that exposing condenser sections to the room improved annual performance of the heat pipe system (Figure 3.11). The condenser configuration with four in tanks and one exposed to room air achieved the best balance between early-morning heating and thermal storage for nighttime heating, and combined with the improvements shown in Figure 3.9, achieved an increase in solar fraction of 20.9%.

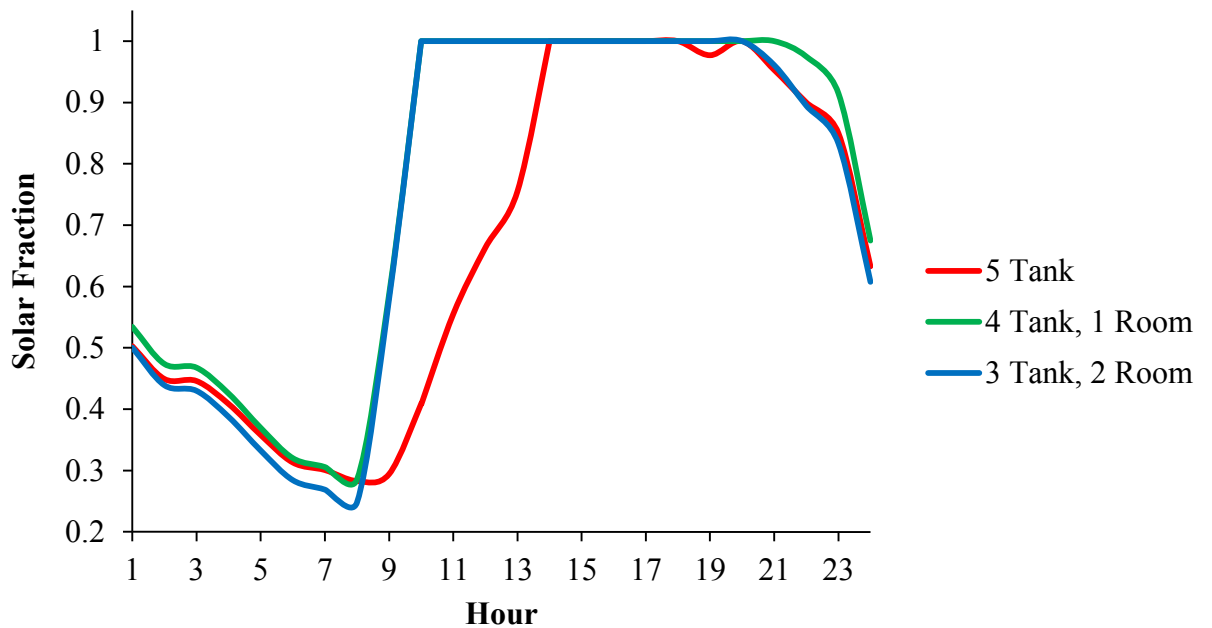


Figure 3.10. Simulated solar fractions on January 15 for three condenser unit configurations.

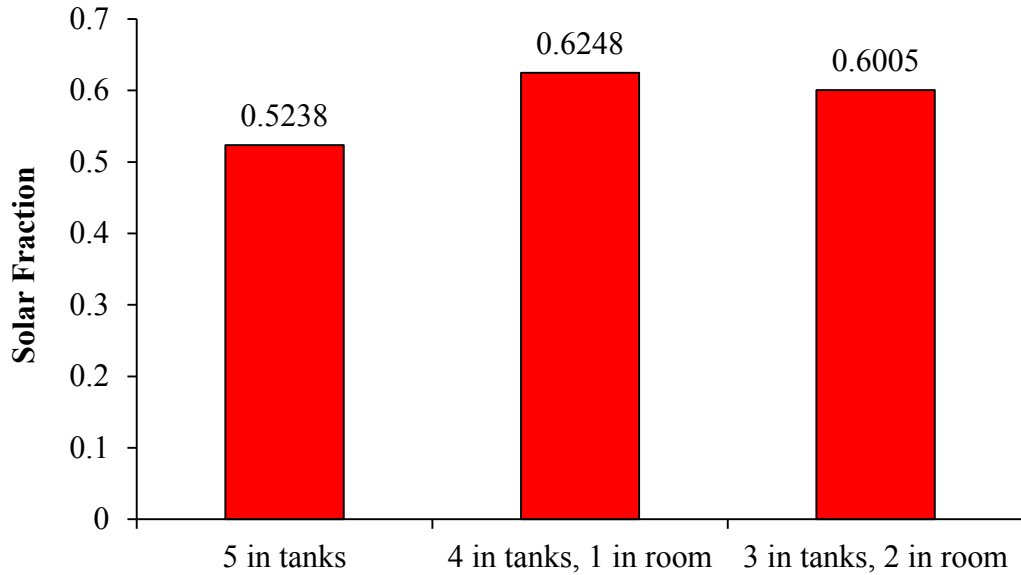


Figure 3.11. Annual solar fraction for each condenser configuration.

3.4.2. Passive Solar Test Facility

The power transfer between each room through the joining wall, calculated using the temperature difference between average room temperatures over the testing period, was a mere 9.7 W. Using the maximum measured temperature (36.3°C) for the room with the new heat pipe system and setting an arbitrary value of 10°C for the room with the old model (approximated as the minimum temperature of the room if the heat pipe system wasn't running) results in a theoretical maximum power transfer through the wall of 55.4 W. This *maximum theoretical* transfer is still less than 5% of the *average* useful gains accrued daily from the heat pipe systems. Thus consideration regarding heat loss or gains between rooms was deemed negligible.

The calculated loss coefficients (UA) for the major components of the envelope for the solar test facility (for each room) are shown in Table 3.3. Blower door testing found an ACH of 0.1. With a collector area for the heat pipe system prototypes of

approximately 2.41 m², the LCR for the prototypes installed in the passive solar test facility was approximately 3.7 W/m²K. This LCR is significantly lower than that used for previous simulations characterizing typical buildings (LCR = 10 W/m²K). The simulated annual solar fraction for the new, four-tank design, with the LCR reduced from 10 W/m²K to 8, 5, and 3.7 W/m²K, respectively, is shown in Figure 3.12. Decreasing the building UA alone (or alternatively, increasing the collector area for a fixed building UA) can greatly increase the solar fraction.

Table 3.3. Rated R-values and calculated UA values for key components of one room.

Building Component	R-value (m ² *K/W)	UA value (W/K)
Clerestory Windows	1.59	0.48
North Window	1.59	0.43
Door	1.85	1.00
Floor	7.93	1.23
Roof	11.10	0.92
Walls	7.93	3.06
Infiltration	-	1.81
-	Room Nonsolar UA:	8.93

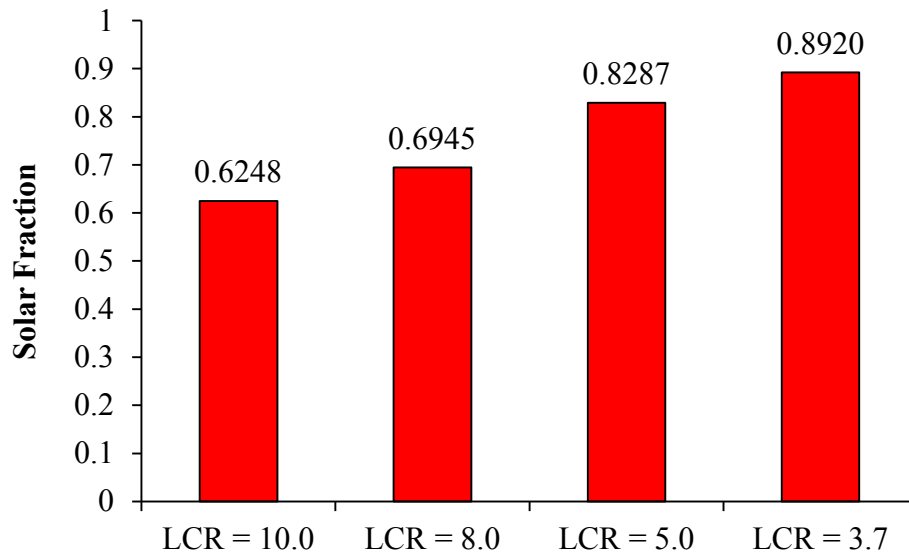


Figure 3.12. Annual solar fraction for the new system at four different Load-to-Collector ratios.

3.4.3. Heat Pipe Systems Experiments

A plot of typical hourly average values for insolation, ambient temperature, and absorber and evaporator temperatures for both prototypes from January 15 to 18 is shown in Figure 3.13. Both the aluminum (old prototype) and copper (new prototype) absorbers exhibited similar rates of increase in temperature during the onset of insolation, but the peak temperature and the difference between absorber and evaporator temperatures were both considerably smaller for the modified system during sunny days due to the higher conductivity of the copper absorber and of the soldered joint between the absorber and the evaporator. Although higher absorber temperatures were obtained for the previous design, the new design achieved greater evaporator temperatures indicating greater heat transfer to the working fluid in the heat pipe. The absorber for the modified system cooled to ambient temperature during the night, while the absorber for the previous system remained warm because of thermal bridging along its copper adiabatic section.

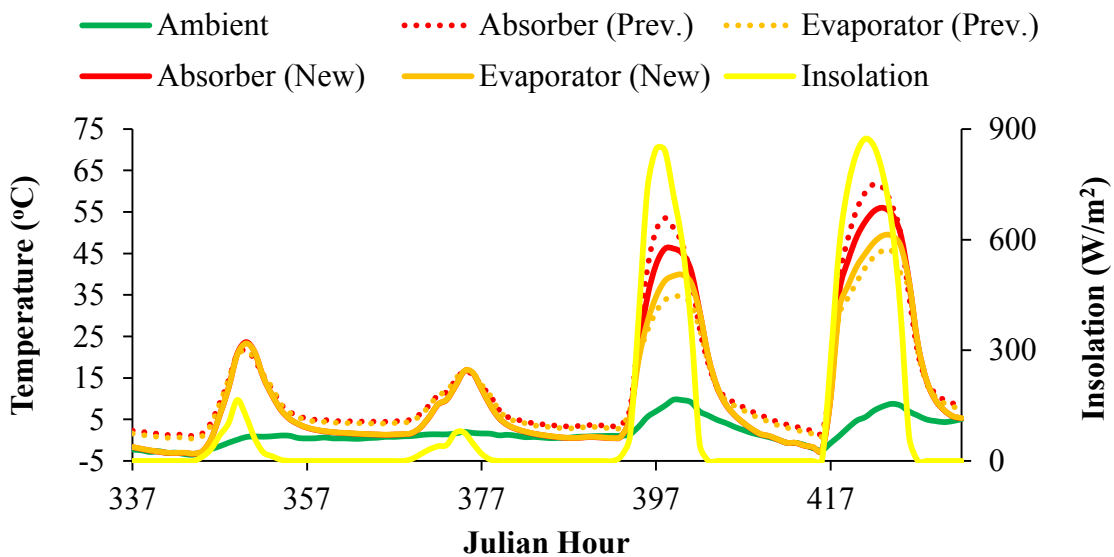


Figure 3.13. Average hourly values for insolation, ambient temperature, and absorber and evaporator temperatures for both experimental prototypes for January 15 through 18.

A plot of hourly average values for insolation, ambient temperature, and tank and room temperatures for both experimental prototypes from February 14 to 16 is shown in Figure 3.14. These days represented three consecutive days of good insolation. For each day, at the onset of insolation, the temperature in the tanks increased at a greater rate for the new design than that of the previous design due to its greater conductance between absorber and evaporator. The directly exposed condenser, as well as more convective surface area between the storage tanks and the room, contributed to the higher rate of increase in room temperature for the new system. (With the thicker insulation of the new design, the thermal storage tanks extended entirely into the room, whereas the tanks of the previous model were recessed into the wall.) The total convective surface area for the four tanks of the new system was 3.64 m². The previous system contained an additional tank, yet had a total convective surface area of only 1.99 m². Even though it contained less thermal mass, a greater temperature difference between the tanks and ambient, and more convective surface area for heat transfer to the room, the rate of temperature decrease during nighttime for the new system was nearly equivalent to the previous model – primarily due to reduced nighttime losses from increased insulation and less thermal bridging. This trend of higher energy gains during sunny days and similar losses during cloudy days and nighttime compounded net gains over time. Room temperature was higher in the new system by 3.9°C at the beginning of February 14 (22.7°C for the previous vs. 26.6°C for the new), 5.1°C at the end of February 14 (25.2°C vs. 30.3°C), 5.5°C at the end of February 15 (21.8°C vs. 27.3°C), and 8.1°F (19.7°C vs. 27.8°C) by the end of February 16.

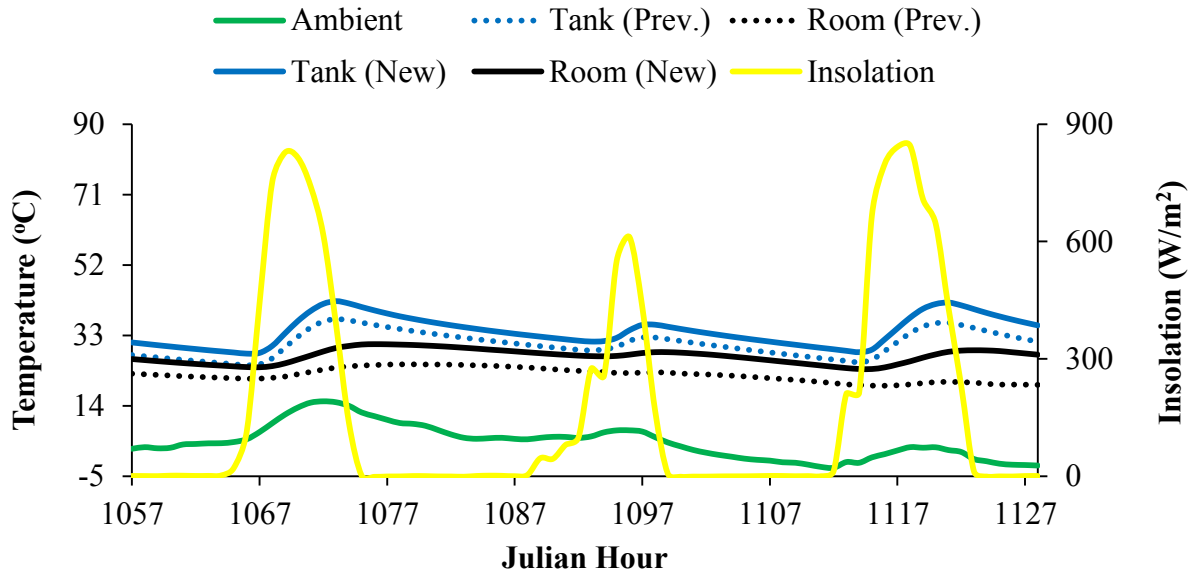


Figure 3.14. Average hourly values for insolation, ambient temperature, and tank and room temperatures for both experimental prototypes for February 14 through 16.

A plot comparing average and maximum tank and room temperatures, respectively, over the entire testing period is shown in Figure 3.15. The average ambient temperature during the entire testing period was 4.1°C (39.4°F). The longest period of cloudy days with insignificant insolation was five days (January 27 – 31). During this period, the new system maintained hourly average tank and room temperatures of 22.6 and 21.0°C, respectively, while the previous system had temperatures of 20.2 and 17.9 °C, respectively. Over the entire testing period, average tank temperatures for the new system was 13.4% higher than the previous system, and average room temperature was 24.6% higher. The average daily peak thermal efficiency for the new and previous models were 85.0% and 80.7%, respectively, with the new system attaining a maximum peak thermal efficiency of 92.7% compared to 90.6% for the previous.

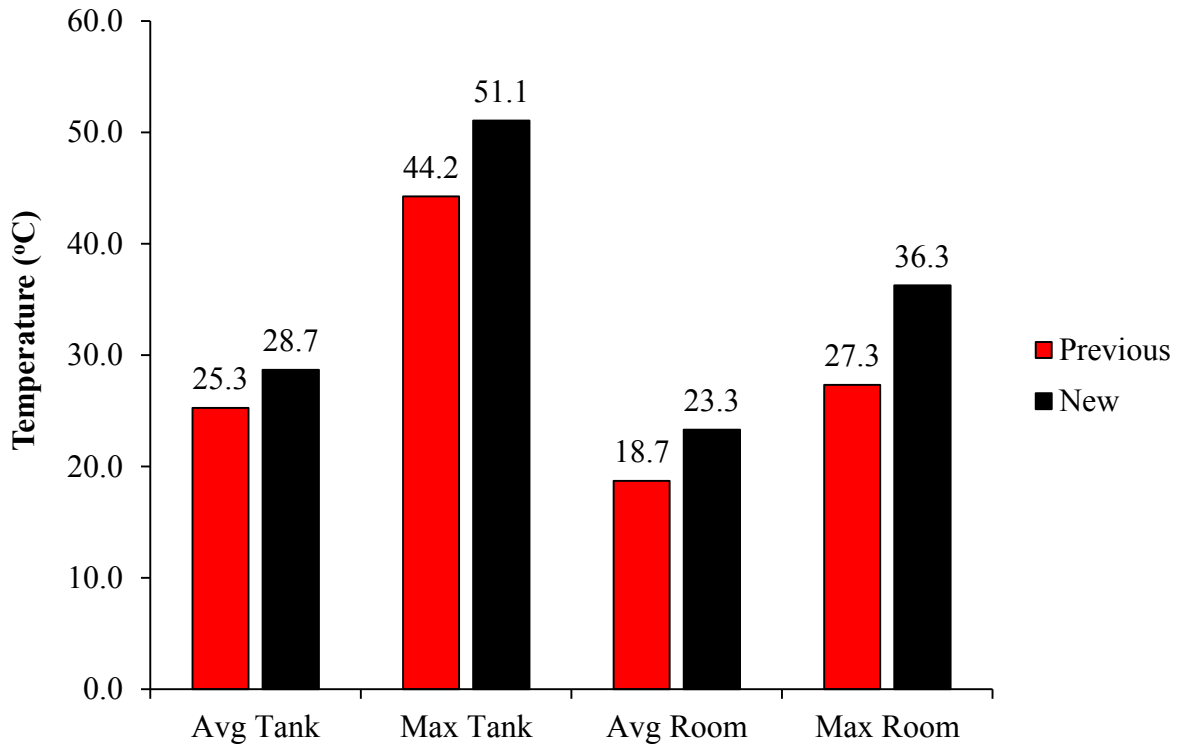


Figure 3.15. Average and maximum tank and room temperatures for both experimental prototypes over the entire testing period.

Efficiency versus loss potential to insulation ratio for the new system is plotted in Figure 3.16. Using the criterion specified in Section 3.3.5 resulted in a reasonable number of samples for the plot. Data points for the plot were centered around solar noon, where beam radiation angle of incidence varied from 30.6° (January 3) to 40.3° (February 17). Partial compliance with ASHRAE 93 was achieved by selecting data with insolation variation no greater than $\pm 32 \text{ W/m}^2$ per 10 minutes. The curve fit implies a collector efficiency of 79.3% when ambient temperature is equal to storage temperature – versus a 74.1% efficiency for the old system at its initial location (prior to installation in the PSTF). The slope and intercept of the trendline are similar to the heat removal factor * overall loss coefficient, $F_R U_L$, and heat removal factor * transmittance absorptance product, $F_R(\tau\alpha)$, respectively, for active collectors. For the heat pipe system, the intercept

is on the high end, and the slope closer to the average, of the range of $F_R(\tau\alpha)$ and $F_R U_L$ values, respectively, for glazed flat plate collectors [SRCC, 2014]. This high intercept is likely the result of the enhancement of heat transfer by the thick copper absorbers and boiling heat transfer in the evaporator.

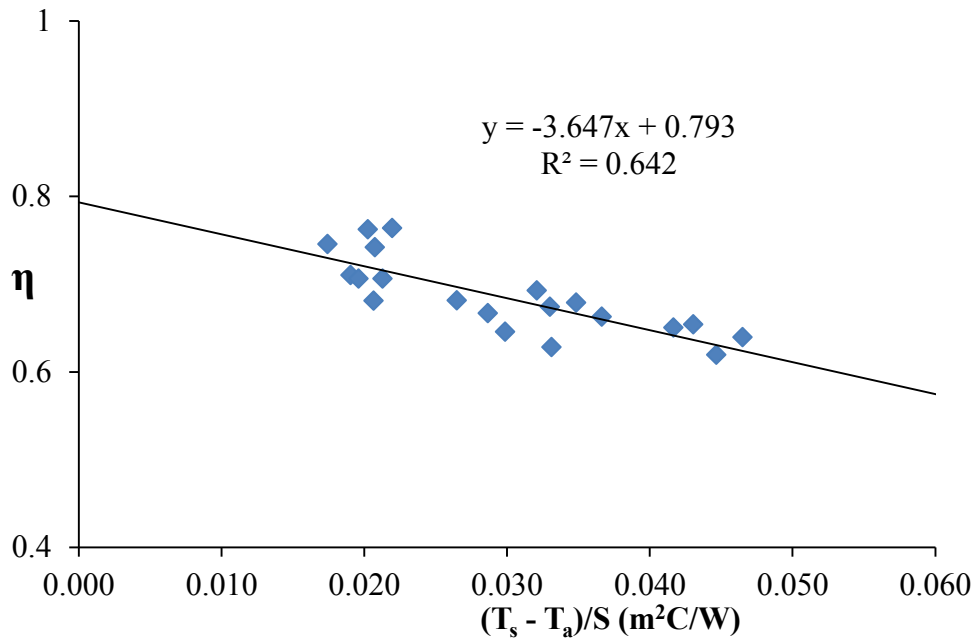


Figure 3.16. New system efficiency versus loss potential/insolation ratio.

3.4.4 Matching Simulations and Experiments

Figure 3.17 shows the simulated and experimental evaporator, tank and room temperatures, from January 5 – 7, after matching. Conductances that were changed as a result of the matching process are shown in Table 3.4. Conductance k_{56} was adjusted but is temperature-dependent, thus minimum and maximum values for this conductance are also reflected in Table 3.4. Results showed that simulated behavior was unaffected by the added capacitances for the evaporators, condensers, and tank wall (nodes 2, 3 and 5, respectively from Figure 3.4), thus these capacitances were removed to regain simplicity of the model. Figure 3.17 confirms absorber fin conduction k_{12} (Figure 3.4), since

simulated and experimental evaporator temperatures are nearly identical over the 72-hour period – with the exception of periods with high insolation on January 5 and 7. This may be a result of the new absorber fin design in which the fins are soldered into each evaporator centerline, thus leaving a portion of the evaporator directly exposed to insolation and, accordingly, resulting in slightly higher experimental temperatures than simulated temperatures that only account for k_{12} heat transfer from the absorber. Although the experimental evaporator temperatures are as much as 3.07 K higher during these times, the remaining experimental and simulated temperatures (during periods of lower insolation) are very close and the average difference in temperatures over the 72-hour period is still only 0.5 K.

The matching study conducted by Albanese, et al. [2012], in which simulated temperatures were matched to experimental bench-scale model temperatures, was used as a guideline for adjustments made to conductance k_{23} . Albanese achieved best fit when k_{23} was reduced to 6% of its baseline value; the best fit for the full-scale prototype was obtained when k_{23} was reduced to 4%. Large changes in k_{23} are necessary to affect the response of the thermal network because the initial value of k_{23} was nearly 35 times larger than all other conductances. With the applied 96% reduction, the conductance for k_{23} was 1.4 times larger than the next largest conductance in the network: conduction through the thin tank wall k_{45} (286.8 W/m²K), and 3.8 times larger than the maximum conductance for temperature-dependent convection from the condenser to tank, k_{34} (104.2 W/m²K). Conductances for k_{23} , k_{45} and k_{34} are the only ones in the thermal network that were greater than 100 W/m²K.

While the conductance between the tank wall and room, k_{56} , was based on well-established formulas for free convection from a vertical flat surface, radiation effects were unaccounted for. The best fit was obtained when k_{56} was increased by a factor of 2, while retaining the same temperature-dependent functional form. This implies that radiation is a significant component of k_{56} due to high emissivity of the flat black surface of the tanks and a higher temperature difference between the tank wall and room walls, floor and ceiling (driving radiative heat transfer) than that between the tank wall and adjacent boundary layer (driving convective heat transfer). Additionally, the solar wall conductance k_{41} was increased to match the rate of decrease in tank temperature during cloudy and/or nighttime periods. The best fit was obtained by increasing k_{41} by a factor of 4, and most likely was a result of imperfect insulation in the solar wall. However, the increased value of k_{41} remained low at 0.6586 W/m²K. The maximum difference between simulated and experimental tank temperatures over the 72-hour period was 1.45 K and the average difference was 0.41 K.

Finally, adjustments were made to the room capacitance and LCR to obtain the best fit for room temperature. Room capacitance was increased by a factor of 4.75 to match the rate of room temperature increases and decreases. With thermal mass of only the room air and OSB sheathing initially added for matching, it was expected that an increase in the thermal mass would be required. Additional room components included 11.25” of EPS core for all walls and the floor, 16” of EPS core in the roof, 2 x 12 connection posts at the end of each panel, a computer desk, and data acquisition hardware. Once the temperature rates in the room were matched, the best fit for the room was obtained at an LCR equal to 8.0 W/m²K. Potential reasons for a higher LCR value than that calculated

are infiltration through the door (which was sealed by the blower door apparatus during infiltration measurements) and uncertainty in R-value ratings for envelope components. After matching, the maximum difference between simulated and experimental room temperatures over the 72-hour period was 0.71 K and the average difference was 0.19 K. For further validation of these adjusted thermal network parameters, two additional days from the testing period were selected using the adjusted parameters shown in Table 3.4. Results of this analysis can be found in the appendices.

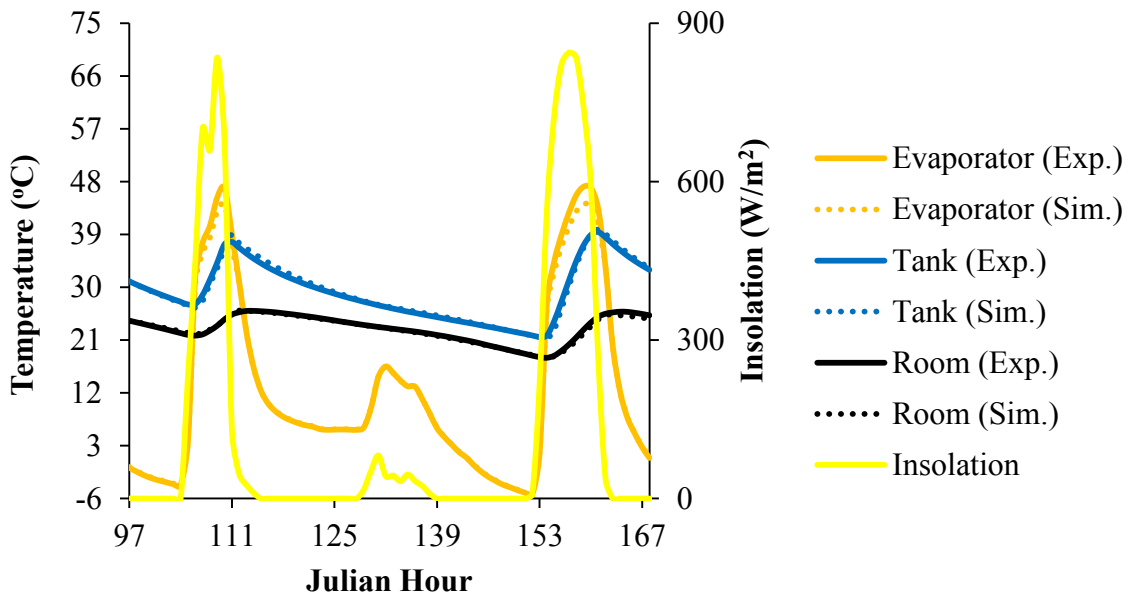


Figure 3.17. Simulated and experimental evaporator, tank and room temperatures, from January 5 – 7, after matching.

Table 3.4. Conductances before and after matching with experiments.

Conductance	Before Matching (W/m ² K)	After Matching (W/m ² K)
k_{23}	9861.1	394.4
k_{56}	5.0 / 6.6	6.4 / 12.5
k_{41}	0.1646	0.6586
k_{67}	3.7	8.0
Capacitance	Before Matching (J/K)	After Matching (J/K)
Room	5.0×10^5	2.4×10^6

3.5. Chapter 3 Conclusions

The performance of the solar heat pipe system, previously shown to already have significant thermal performance advantages over other conventional passive systems, has been further enhanced with several key design modifications. These modifications, including a copper absorber, soldered joint between absorber and evaporator, rubber adiabatic section, thicker insulation, and one condenser exposed directly to room air, increased the rate of useful gains and reduced thermal losses, leading to greater system efficiency and higher room temperature.

These results also highlight the potential for very high solar fraction in well-insulated buildings, such as the passive solar test facility used in this study. The decrease in load to collector ratio LCR from 10 W/m²K, characteristic of typical buildings, to 3.7 W/m²K, estimated for the PSTF, resulted in a simulated increase in solar fraction from 62.5% to 89.2%, even in the cool and moderately sunny climate of Louisville, KY. However, a challenge for utilizing low LCR is evident in the elevated room temperatures in Figure 3.15. Note that the maximum (and average) temperatures exceeded the upper comfort limit, indicating the need to vent excess heat during these winter months. While ventilation may be effective during the winter when ambient temperature can provide cooling, more problematic is unwanted gains during the spring, fall and summer, when ambient temperature is too high to allow cooling. Thus, to effectively utilize low values of LCR, measures must be taken to reduce unwanted thermal gains during periods when ambient temperature exceeds the upper comfort limit, for instance by passive and/or active control mechanisms.

After adjustments to conductances within the thermal network model for heat transfer between the evaporators and condensers (k_{23}), between the tank wall and room (k_{45}), solar wall insulation (k_{41}), and the LCR (k_{67}), simulated system temperatures matched well with experimental data. It was also necessary to add additional thermal mass in the room to achieve the best fit. While the capacitances for the evaporators, condensers, and tank wall were negligible with respect to simulation results, it is pertinent to note that since absorber temperatures were fixed using experimental data in the matching study, thermal mass for the absorber was not considered.

A thorough economic analysis has yet to be performed to evaluate tradeoffs between system efficiency and overall cost. An example of a compromise that may reduce the cost per unit of energy saved is the absorber design. While the copper absorber improved system efficiency slightly compared the previous aluminum absorber, the greater cost must be taken into account. Similar tradeoffs exist in each component, as well as in the integrated design, for reducing manufacturing, transportation and installation costs.

CHAPTER 4: REDUCING UNWANTED THERMAL GAINS DURING THE COOLING SEASON FOR A SOLAR HEAT PIPE SYSTEM

4.1 Chapter 4 Overview

The heat pipe augmented solar heating system significantly reduces heating loads relative to other conventional passive space heating systems. However, thermal gains from the system during the cooling season increase cooling loads and tend to increase overall space conditioning loads. The effectiveness of several design modifications and control strategies for the heat pipe wall to reduce unwanted gains was investigated. Computer algorithms were used to simulate four different unwanted gains reduction mechanisms: shading, an opaque cover, a mechanical valve, and switching the elevations of the evaporator and condenser sections to provide heat transfer *out* of the room during the cooling season. For each mechanism, three different control strategies were evaluated: 1) *Seasonal control*, for which the prescribed mechanism was deployed at the beginning and removed at the end of the cooling season, 2) *ambient temperature-based control*, for which the mechanism was deployed if the forecast for the next hour was greater than 18.3°C (65°F), and 3) *room temperature-based control*, for which the mechanism was deployed if auxiliary cooling was required for the previous hour. For the seasonal strategy, a season determination (SD) parameter was defined and results suggested that SD may be a ‘universal’ parameter that can be applied across a range of climates for

quick cooling season assessment. The heat pipe system performed best with ambient temperature-based control strategy, and the cover and valve were the best single mechanisms. Experiments on a full-scale heat pipe wall prototype using valve and cover control mechanisms confirmed significant reductions in unwanted thermal gains with little to no increase in room temperature during the testing periods.

4.2. Chapter 4 Introduction

The heat pipe augmented passive solar space heating system greatly improves heating season performance relative to conventional passive space heating systems [Albanese et al. 2012]. The heat pipes consist of three main components: the evaporator, adiabatic section, and condenser. The evaporator is located on the building exterior and is connected to an absorber coated with a selective surface. As the evaporator heats up during insolation, a two-phase fluid within the evaporator boils and rises through the adiabatic section of the heat pipe, which transports the hot, gaseous fluid through the insulated building wall. The fluid next enters the cooler condenser, located in a thermal storage tank within the building interior. Heat is transferred to thermal storage, condensing the two-phase fluid back into liquid, which returns to the evaporator via gravity assistance. During periods of little to no insolation, when the evaporator is cooler than the condenser, the liquid fluid remains in the evaporator and no heat transfer takes place within the heat pipe. Utilizing this thermal diode effect results in high levels of heat transfer into the space and little heat transfer out of the space. Additionally, two-phase heat transfer allows the heat pipe to operate with small temperature gradients throughout and enables the system to operate with small elevation differences between the

evaporator and condenser sections so that the entire system can be installed on a south-facing wall.

In addition to studying simulated performance of heat pipe systems, Albanese et al. [2012] also constructed an experimental bench-scale model. This single unit achieved an average system thermal efficiency of 85.0% utilizing a low-iron glass cover, insulated adiabatic section, and a refrigerant (SUVA 124) as the heat pipe working fluid with a fill level of 120% of the evaporator volume. A full-scale prototype was constructed, retrofitted onto a classroom wall on campus, and tested by Robinson et al. [2013]. The unit contained five individual heating units with a total collector area of approximately 2.41 m², one inch nominal diameter copper heat pipes, and a total of approximately 0.322 m³ (85 gallons) of water for thermal storage. The system achieved a maximum daily peak thermal efficiency of 83.7% and an average daily peak thermal efficiency of 63.4%, while thermal storage delivered heat to the room throughout the testing period, including a sequence of four consecutive cloudy days. Robinson & Sharp [2014] implemented design modifications to the Robinson et al. model and constructed a new prototype (Figure 4.1). Key features of the new design included (1) a copper absorber with reduced thermal resistance between the absorber and evaporator compared to the previous model that used aluminum absorbers epoxy-bonded to copper evaporators, (2) thicker solar wall insulation and a rubber adiabatic section that reduced thermal losses from storage to outdoors, and (3) one condenser exposed directly to room air that significantly improved early-morning heating of the room and overall solar fraction. This new model and the previous model were installed in identical 12' by 12' rooms of a passive solar test facility (PSTF), and comparative testing was performed during January and February of 2013.

Average daily peak efficiency for the previous system under the improved conditions provided by the PSTF was 80.7%, while an efficiency of 85.0% was achieved by the new system. During the testing period, the new model also achieved average storage and room temperatures that were 13.4% and 24.6%, respectively, higher than those of the previous model.

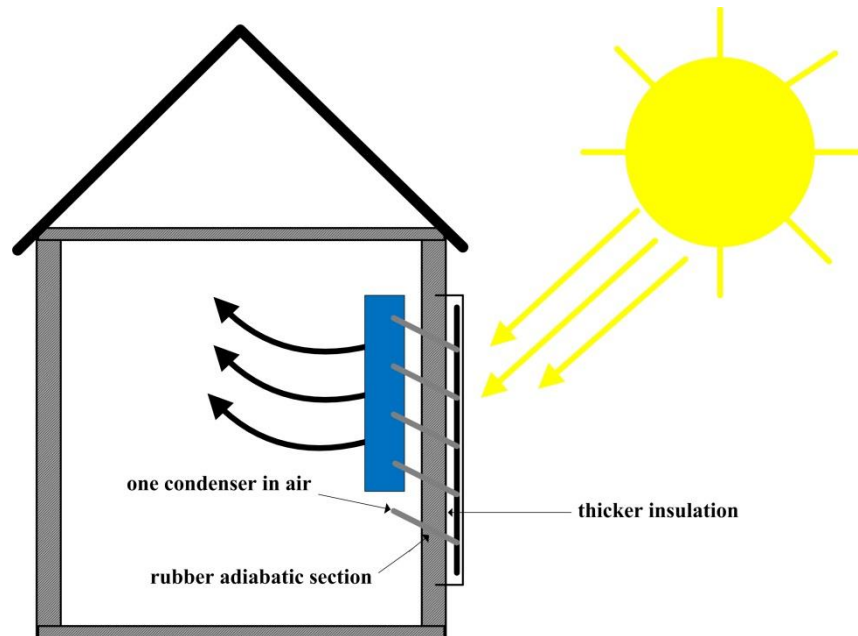


Figure 4.1. Schematic of the solar heat pipe system highlighting design modifications relative to the previous model.

While the overwhelming focus has been on performance during the heating season, previous investigators have recognized the potential for passive systems to overheat during the cooling season, which impacts the total annual energy required to both heat and cool the building [Zaheer-Uddin 1989, Athienitis & Ramadan 1999, Kummert et al. 2000, Raicu et al. 2002]. Features to provide cooling from systems designed primarily for heating have been studied [Ghrab-Morcus et al. 1993, Gan 1998, Mihalakakou 2002, Bataineh & Fayed 2011]. Similar to other passive systems, the solar heat pipe wall can generate thermal gains during the cooling season that may increase the cooling load, thus

offsetting energy savings achieved during the heating season. The objective of this study was to compare, using computer simulations, the effectiveness of four different mechanisms to reduce summertime solar gains from the heat pipe system, as well as three control strategies defining when the mechanisms are employed. Furthermore, mechanisms that simulations suggested were effective options for cooling season reductions were implemented into the new prototype installed in the PSTF [Robinson & Sharp 2014] and the system was tested during the cooling season (August and September, 2013) in Louisville, KY.

4.3. Chapter 4 Methods

4.3.1 Computer Modeling

Simulations were conducted using a thermal network model for the heat pipe system adapted and revised from previous investigators [Corliss 1979, Susheela & Sharp 2001, Albanese et al. 2012, Robinson & Sharp 2014]. The thermal network for the new heat pipe design that was tested for this study is shown in Figure 4.2. Descriptions for each conductance in Figure 4.2 are shown in Table 4.1.

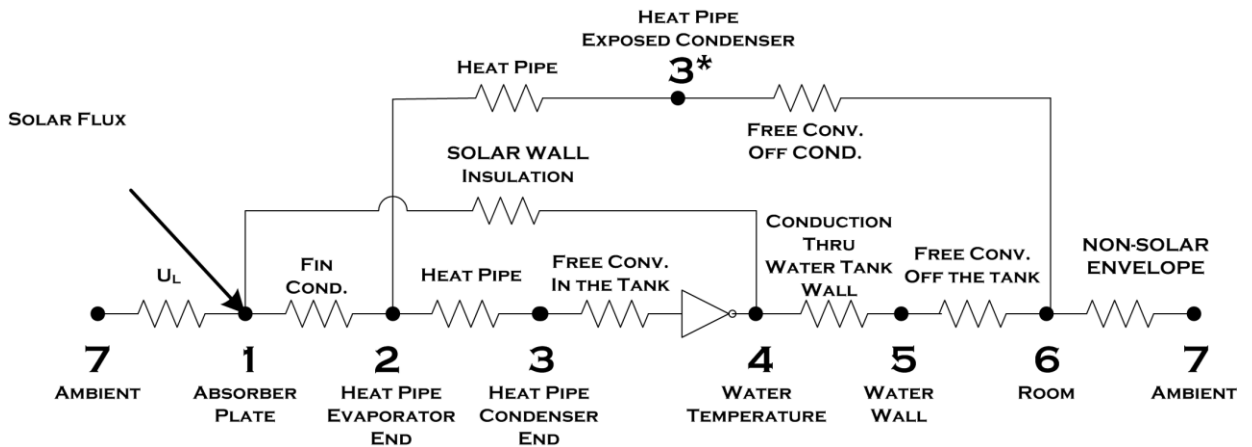


Figure 4.2. Thermal network for the heat pipe assisted solar wall.

Table 4.1. Description of thermal conductance values used for heat pipe wall thermal network models.

Conductance Value (W/m ² K)	Description
k_{71}	Overall collector loss coefficient
k_{12}	Absorber fin conduction and convection to the working fluid
k_{23} and k_{23}^*	Two-phase heat transfer from evaporator to condenser when $T_1 > T_4$ for condenser in storage and $T_1 > T_6$ for condenser in room air, continuous conduction along heat pipe wall
k_{41}	Conduction through insulated wall
k_{34}	Convection between condenser and storage water
k_{3*6}	Convection between condenser and room air
k_{45}	Conduction through water tank wall
k_{56}	Convection between tank wall and room
k_{67}	Building Load-to-Collector Ratio (LCR)

Between nodes i and j , the heat transfer rate \dot{q}_{ij} per unit of collector area is given by

$$\dot{q}_{ij} = k_{ij}(T_j - T_i) \quad (4.1)$$

where k_{ij} is the heat transfer coefficient between nodal temperatures T_j and T_i , respectively. For the i^{th} node, the energy balance equation is

$$m_i \frac{dT_i}{dt} = \sum_j [k_{ij}(T_j - T_i)] + S_i \quad (4.2)$$

where m_i is the capacitance (product of the mass of the node and its specific heat) per unit collector area, S_i is the solar power received per unit collector area (node 1 from Figure 4.2), and t is time. Using a central difference discretization scheme over time step Δt , Equation 4.2 becomes

$$\left(\frac{2m_i}{\Delta t} + \sum_j k_{ij} \right) T_i - \sum_j (k_{ij} T_j) = \frac{2m_i T_{io}}{\Delta t} + \sum_j [k_{ij} (T_{jo} - T_{io})] + (S_i + S_{io}) \quad (4.3)$$

where the previous time step is denoted by the zero subscript. Using MATLAB software and Typical Meteorological Year weather data (TMY3), all nodes were simultaneously solved as a function of time from a set of initial temperatures. Iterations were used for heat transfer coefficients dependent on nodal temperatures. Key baseline parameters included a Load to Collector Ratio (the ratio of the UA value for the nonsolar part of the building to the collector area; conductance k_{67} in Figure 4.2 and Table 4.1) of LCR = 10 W/m²K and a defined room comfort range of 18.3 to 23.9°C (65 to 75°F). To simulate auxiliary heating and cooling, room nodal temperatures were restricted within the room comfort range. Two additional room comfort ranges – 20.0 to 22.2°C (68 to 72°F) and 20.6 to 21.7°C (69 to 71°F) – were tested to study the effects that room comfort limits have on annual space conditioning loads. To represent a range of climates, including available insolation and seasonal temperatures, simulations were conducted for four different locations: Albuquerque, NM, Louisville, KY, Rock Springs, WY, and Madison, WI.

Four different unwanted gains reduction mechanisms were simulated:

- Shading – Beam insolation is eliminated, simulating an overhang above the collector (Figure 4.3). Diffuse and ground reflected insolation is still received by the collector.
- Cover – All insolation is eliminated, simulating an opaque cover over the collector (Figure 4.4).

- Valve – Phase change heat transfer in the heat pipe is turned ‘on’ or ‘off,’ simulating a valve in the adiabatic section of the heat pipe (Figure 4.5).
- Switching – The direction of heat transfer in the heat pipe is reversed, simulating the switching of the elevations of the evaporator and condenser sections of the heat pipe (Figure 4.6). Heat is thus transferred *out* of thermal storage when the absorber is cooler than storage, which tends to occur only during nighttime and cloudy days. A system design in which the evaporator and condenser sections of the heat pipe are leveled would make this mechanism more convenient to employ, thus a bench scale experiment with leveled evaporator and condenser sections was performed to examine the effects on heat pipe performance (Section 4.2.2).

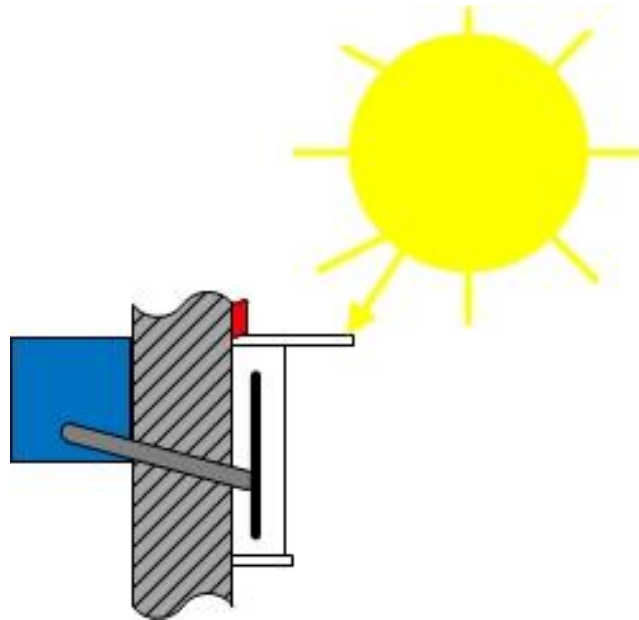


Figure 4.3. Shading (blocking of beam radiation) to reduce unwanted gains.

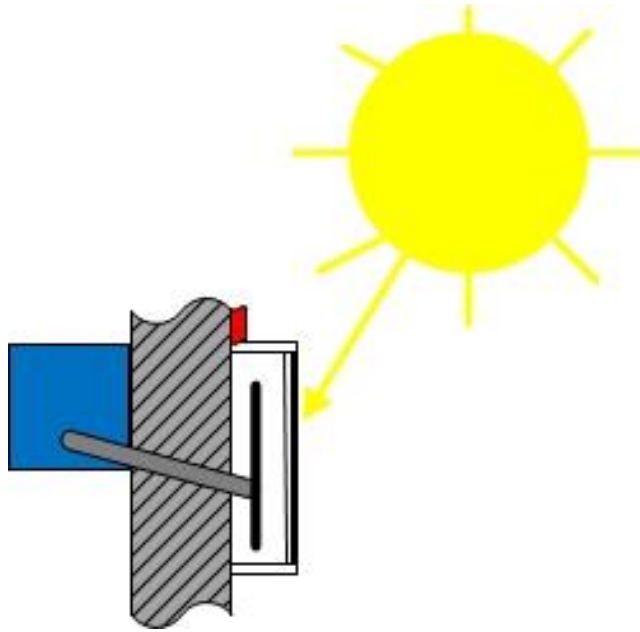


Figure 4.4. Opaque cover (blocking all solar radiation) to reduce unwanted gains.

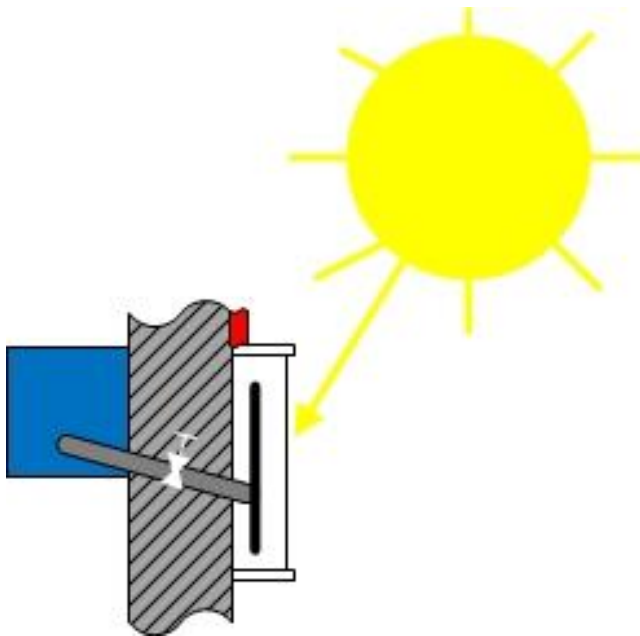


Figure 4.5. Valve to reduce unwanted gains.

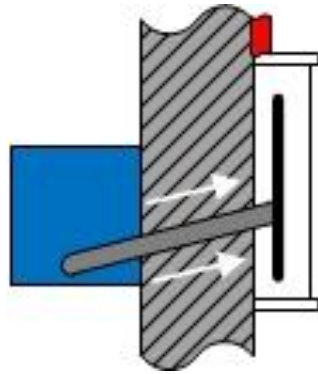


Figure 4.6. Switching to reduce unwanted gains.

For each mechanism, three different control strategies were evaluated:

- Seasonal Control – The mechanism is employed at the beginning of the cooling season and removed at the end of the cooling season. For the seasonal strategy, a parameter was derived for determining the optimal months in which the unwanted gains reduction mechanism should be deployed to minimize overall space conditioning loads.
- Ambient Temperature-Based Control – The mechanism is employed if the forecast for the *next* hour (based on TMY3 weather data) is greater than 18.3°C (65°F).
- Room Temperature-Based Control – The mechanism is employed if the room temperature for the *previous* hour reached the upper comfort limit of (23.9°C / 75°F). At the beginning of the current hour, control mechanism employment is dependent on the room temperature at the conclusion of the previous hour, thus this strategy is similar to a typical thermostat.

Solar energy absorbed by the collector is given by [Duffie and Beckman, 2006]

$$S = (I_b + I_d A_i) R_b (\tau\alpha)_b + I_d (1 - A_i) (\tau\alpha)_d * \left(\frac{1 + \cos \beta}{2} \right) \left[1 + f \sin^3 \left(\frac{\beta}{2} \right) \right] + I \rho_g (\tau\alpha)_g \left(\frac{1 - \cos \beta}{2} \right) \quad (4.4)$$

where the first group of terms on the right hand side of the equation represents the direct (beam) component of solar irradiation, the second group of terms represents the diffuse component, and the final group of terms represents the ground reflected component.

Unwanted gain reduction mechanisms were simulated as follows:

- Shading – The beam component of Equation 4.4 was removed.
- Cover – Equation 4.4 was set equal to zero.
- Valve – Conductances k_{23} and k_{23*} were reduced to only conduction along the pipe wall, regardless of temperature.
- Switching – Conductance k_{23} was set equal to the thermal conductance along the heat pipe wall when the outdoor end of the heat pipe (the evaporator in the normal mode) is hotter than the indoor end, $T_2 > T_3$. When $T_3 > T_2$, k_{23} the conductance of two-phase flow within the pipe was added. Conductance k_{23*} was set similarly, except that the indoor temperature is T_{3*} rather than T_3 .

Simulations calculated annual heating and cooling load and the total annual space conditioning load resulting from employing each individual mechanism, and feasible combinations of each, using each respective control strategy.

Annual heating load per unit collector area is

$$q_{a,hl} = \sum_{year} k_{67} (T_b - T_7)^+ \Delta t \quad (4.5)$$

and annual cooling load per unit collector area is

$$q_{a,cl} = \sum_{year} k_{67}(T_7 - T_b)^+ \Delta t \quad (4.6)$$

where T_7 is ambient temperature (from TMY3 data) and T_b was the commonly used base temperature of 18.3°C (65 °F). $q_{a,cl}$ is equivalent to annual auxiliary cooling. Annual auxiliary heating load per unit collector area is

$$q_{a,aux} = \sum_{year} \left[k_{67}(T_6 - T_7) - k_{56}(T_5 - T_6)^+ - k_{3*6}(T_{3*} - T_6)^+ \right] \Delta t \quad (4.7)$$

whenever ambient temperature was less than room temperature ($T_7 < T_6$), and room temperature dropped to the lower comfort limit ($T_6 = 18.33^\circ\text{C}$). The second and third term within the summation represents the contribution from the thermal storage and exposed condenser, respectively, to serving the heating load. The first term is different from the heating load (Equation 4.6) in that room temperature T_6 may exceed T_b .

For assessment of the cooling capabilities of the heat pipe system using the switching mechanism, annual heat transfer *out* of the system per unit collector area, is

$$q_{a,sw} = \sum_{year} \left[k_{34}(T_4 - T_3) + k_{3*6}(T_6 - T_{3*}) \right]^+ \Delta t \quad (4.8)$$

whenever the system is in cooling mode (all summer for seasonal control, when ambient temperature is greater than 65°F for ambient control, and when room temp is limited to 75°F for room control.) Annual unwanted thermal gains per unit collector area are

$$q_{a,uwg} = \sum_{year} \left[k_{56}(T_5 - T_6)^+ + k_{3*6}(T_{3*} - T_6)^+ \right] \Delta t \quad (4.9)$$

whenever room temperature reached the upper comfort limit, and ambient temperature is greater than room temperature.

System solar fraction, SF , is the fraction of annual heating load that is served by the heat pipe system

$$SF = 1 - \frac{q_{a,aux}}{q_{a,hl}} \quad (4.10)$$

For the seasonal strategy, a parameter that defines the cooling season was also developed. The first step of this method involved conducting simulations in which an opaque cover was added to the heat pipe system for every feasible sequence of months that could represent the cooling season. The best cooling season definition was that which minimizes total annual auxiliary energy use

$$q_{total} = q_{a,aux} + q_{a,cl} + q_{a,uwg} \quad (4.11)$$

The optimal cooling season was then compared to a new parameter, the season determination (SD) ratio

$$SD = \frac{q_{m,uwg}}{q_{m,hl}} \quad (4.12)$$

where the calculated unwanted gains for a respective month is

$$q_{m,uwg} = \sum_{month} \left[k_{56}(T_5 - T_6)^+ + k_{3*6}(T_{3*} - T_6)^+ \right] \Delta t \quad (4.13)$$

and heating load for a month is

$$q_{m,hl} = \sum_{month} k_{67}(T_b - T_7)^+ \Delta t \quad (4.14)$$

SD was calculated for each month of the year for the four initial locations used in simulations (Albuquerque, Louisville, Rock Springs and Madison), and four additional locations: Boston, MA, Chicago, IL, Denver, CO, and Seattle, WA. These locations were added to evaluate repeatability and validity of SD for identifying the optimal cooling season months, thereby reducing the number of simulations required to predict performance for systems using the seasonal control strategy.

4.3.2 Experimental Setup

4.3.2.1 Bench-scale Experiments

The bench-scale model (Figure 4.7) was identical to the one used by Albanese et al. [2012], except thicker insulation was added around the storage tank to reduce thermal losses from the tank to ambient air.

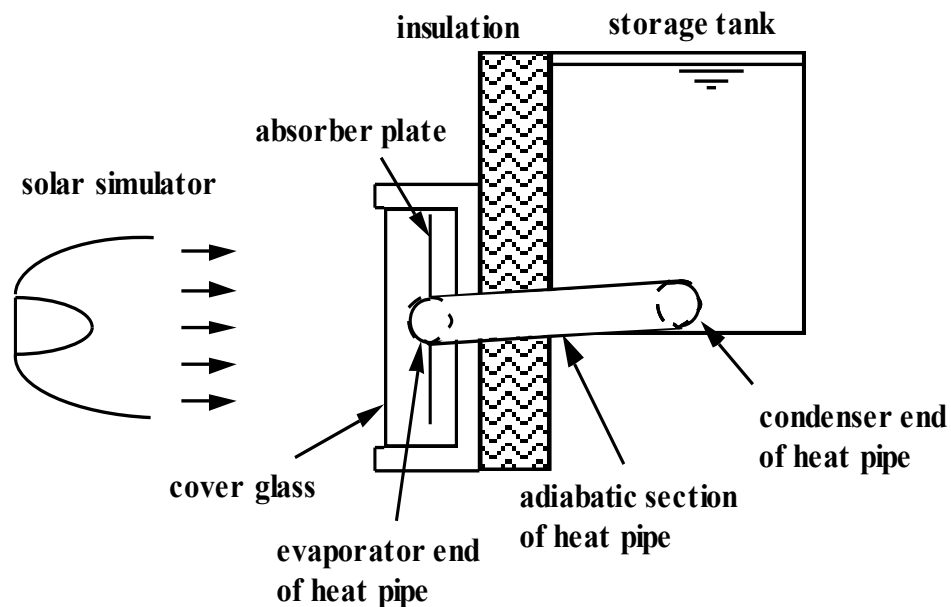


Figure 4.7. Schematic of model used for bench-scale experiments.

Important features of the bench-scale experiment(s) included:

- Three metal halide lamps, that approximate the solar spectrum, to simulate insolation on the collector.
- One 1/8 inch thick low-iron glass cover.
- One inch diameter copper heat pipe – evaporator end attached to absorber, condenser end immersed in water, insulated copper adiabatic section.
- Two copper absorber plate fins, each soldered to opposite center-lines of the copper evaporator pipe; both fins and the exposed half of the evaporator were plated with a black chrome selective surface.
- Insulated wall between the absorber/evaporator and tank.
- Heat pipe working fluid was SUVA-124 refrigerant filled to 120% of the evaporator volume.
- A 50-gallon plastic thermal storage water tank.

Experimental configurations included baseline experiments with each section of the heat pipe sloped at 5 degrees and experiments with leveled evaporator and condenser sections (for accommodating the switching mechanism). A minimum of three separate runs for each case were conducted to ensure repeatability.

4.3.2.2 Full-scale Prototype

The new model installed in the south-facing wall of the PSTF [Robinson & Sharp 2014] was used to test the effectiveness of control mechanisms in reducing unwanted thermal gains to storage and to the room. The PSTF was made of structural insulated panels (SIPs) consisting of 12” thick panels with an R-value of 7.93 m²*K/W (45

ft²F*hr/Btu) for the floor and walls, and 16” for the roof with an insulating value of 11.10 m²*K/W (R-63). The building incorporated a clerestory section and was constructed so that the south-facing wall and clerestory were oriented due south. During experimentation, the clerestory windows were covered with an opaque material to eliminate solar gains, so that the heat pipe system was the only source of heat added to the room. No auxiliary heating or cooling was used.

The cover mechanism consisted of an opaque white vinyl cover over the collector. For the valve mechanism, a valve was installed in each heat pipe between the adiabatic and condenser sections. Closing the valve isolated the adiabatic section from the condenser section. Experiments using individual mechanisms and a combination of both simultaneously were conducted during August 15 -24, August 26 – September 2, and September 4 -11 of 2013. Thermal gains to storage and room were then compared to gains that would have resulted using no control mechanisms, estimated using a procedure described in Section 4.3.4.2.

4.3.3 Instrumentation

4.3.3.1 Bench-scale Experiments

Instrumentation for the bench-scale experiments included 24 T-type thermocouples, with eight located on the absorber, three on the evaporator section, two on the adiabatic section, three on the condenser section, and eight placed within the tank. Data acquisition was accomplished using a National Instruments chassis in conjunction with an SCXI 1600 16 bit digitizer and an SCXI 1102B isolation amplifier with an SCXI 1303 thermocouple module, and LabVIEW software was used to log the data at a sampling rate of 0.01667 Hz (once per minute). Additionally, four pyranometers were mounted, one at

each corner of the collector, to measure modeled solar input from the metal halide lamps.

Prior to each experiment, the metal halide lamps were powered on for approximately one hour to ensure stabilization. Calibration of the light distribution across the collector aperture was accomplished using pyranometers to measure incident radiation across the collector at 15 different equidistant locations. Using combinations of mirrored reflectors and aluminum foil blinders, the lamps were placed in an orientation that yielded a light distribution with a maximum standard deviation normalized by mean radiation value of 5% in conjunction with a minimum mean radiation value of 750 W/m^2 . Also, a correction factor, cf , correlating radiation measured at the four corners to mean radiation across the entire absorber was calculated.

4.3.3.2 Full-scale Prototype

A data acquisition system and accompanying software identical to that used for the bench-scale experiments was used for the prototype experiments. Two pyranometers were mounted on the center of the south wall of the PSTF, one aligned with the top and the other with the bottom of the collectors. Four T-type thermocouples were placed on each central absorber, three on each central evaporator, and two inside each individual storage tank. Additional placements of thermocouples included one attached to the tank wall to measure tank surface temperature, one placed in the room to measure room temperature, two on the exposed condenser, and two placed outside to measure ambient air temperature.

4.3.4 Data Analysis

4.3.4.1 Bench-scale Experiments

Bench-scale system thermal efficiency, η , is given by

$$\eta = \frac{\dot{Q}_u}{SA_c} \quad (4.15)$$

where S is the measured radiation received by the collector and A_c is the collector area.

Useful power gain, \dot{Q}_u , was based on the rate of temperature increase in the tank given by

$$\dot{Q}_u = \frac{Mc_p \Delta T_s}{\Delta t} \quad (4.16)$$

where M is the mass of the water in the tank, c_p is the specific heat of water, and $\Delta T_s / \Delta t$ is the rate of change of tank temperature with time, which was found by fitting a line to experimental results over a 3 °C storage temperature rise from 25 to 28 °C.

4.3.4.2 Full-scale Prototype

All measured temperatures and insolation for the full-scale prototype were averaged over hourly intervals and used to calculate system efficiency by Equation 4.14. With mechanisms deployed to reduce unwanted gains (for these experiments, a cover or a valve in each heat pipe), the objective was to minimize useful power delivered by the heat pipes to storage and to the room, given by

$$\dot{Q}_u = \dot{Q}_s + \dot{Q}_{sr} + \dot{Q}_{cnds_r} \quad (4.17)$$

where \dot{Q}_s represents the net power retained in all four storage tanks, given by

$$\dot{Q}_s = \frac{Mc_p \Delta T_s}{\Delta t} \quad (4.18)$$

where M is the mass of the water in the storage tanks and ΔT_s is the water temperature change during the one-hour time interval Δt . \dot{Q}_{sr} is the power transfer from the storage tanks to the room

$$\dot{Q}_{sr} = \frac{T_s - T_r}{R_{sr}} \quad (4.19)$$

where T_s and T_r are the measured temperatures for the water and room, respectively, and R_{sr} is the total thermal resistance from the thermal mass to the room air. \dot{Q}_{cnds} is the power transfer from the exposed condenser to the room. A thermal resistance network for R_{sr} is shown in Figure 4.8.

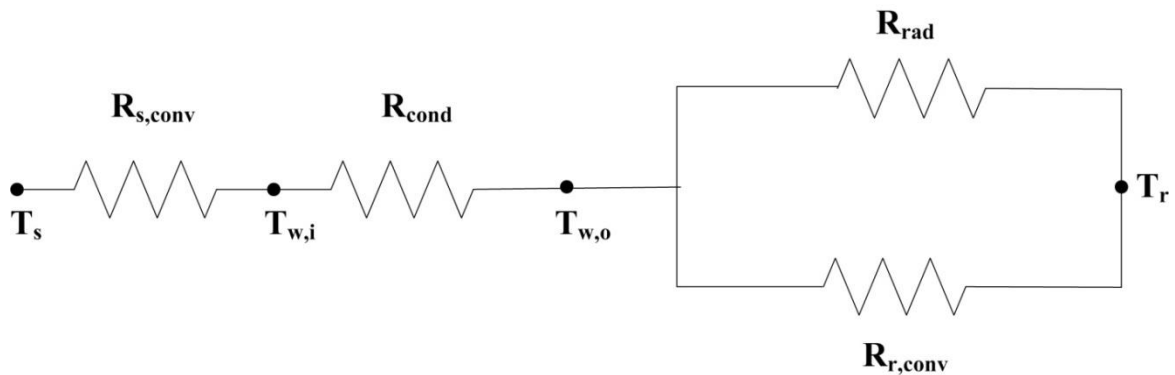


Figure 4.8. Thermal resistance network used to calculate for heating units with a thermal storage tank.

The network included convective heat transfer to the inside surface of the tank wall, $R_{s,conv}$, conduction through the tank wall, R_{cond} , parallel radiation, R_{rad} , and convection, $R_{r,conv}$, from the wall of the tank to the room. Applying the resistance network shown in Figure 4.8, R_{sr} is

$$R_{sr} = R_{s,conv} + R_{cond} + \left(\frac{1}{R_{rad}} + \frac{1}{R_{r,conv}} \right)^{-1} \quad (4.20)$$

where $R_{s,conv}$ and $R_{r,conv}$ are

$$R_{s/r,conv} = \frac{1}{h_{s/r}A_s} \quad (4.21)$$

where A_s is the total heat transfer surface area of the storage tanks, and the convection coefficient for water or air is

$$h_{s/r} = \frac{k_{s/r}Nu_{s/r}}{L} \quad (4.22)$$

where $k_{s/r}$ is the thermal conductivity for water or air, L is the tank wall height, and the Nusselt number, $Nu_{s/r}$ (developed for free convection from a vertical plate [Incropera & DeWitt, 2011]), for water or air is dependent on whether convection conditions are laminar or turbulent. For laminar flow, the Nusselt number is

$$Nu_{s/r} = 0.68 + \frac{0.67Ra_{s/r}^{1/4}}{\left(1 + (0.492/Pr_{s/r})^{9/16}\right)^{4/9}} \quad (4.23)$$

where $Pr_{s/r}$ is the Prandtl number. For turbulent conditions, the Nusselt number is

$$Nu_{s/r} = 0.825 + \frac{0.387Ra_{s/r}^{1/6}}{\left(1 + (0.492/Pr_{s/r})^{9/16}\right)^{8/27}} \quad (4.24)$$

The laminar to turbulent transition depends on the Rayleigh number

$$Ra_{s/r} = \frac{g\beta_{s/r}\Delta T_{sw/wr}L^3}{\nu_{s/r}\alpha_{s/r}} \quad (4.25)$$

where g is the acceleration due to gravity, $\beta_{s/r}$ is the coefficient of volumetric thermal expansion for the water or air, $\nu_{s/r}$ is the kinematic viscosity for water or air, and $\alpha_{s/r}$ is the thermal diffusivity for water or air. The temperature difference between mediums is

$$\Delta T_{sw} = T_s - T_w \quad (4.26)$$

or

$$\Delta T_{wr} = T_w - T_r \quad (4.27)$$

where T_w is the tank wall temperature. For $Ra_{s/r} < 10^9$, free stream conditions are laminar, and when $Ra_{s/r} > 10^9$, they are turbulent.

The conductive resistance through the tank wall is

$$R_{cond} = \frac{t_w}{k_w A_s} \quad (4.28)$$

where t_w is the tank wall thickness and k_w is the thermal conductivity of the tank wall.

Finally, the radiative resistance is

$$R_{rad} = \frac{1}{h_{rad} A_s} \quad (4.29)$$

where

$$h_{rad} = \varepsilon \sigma (T_w + T_r)(T_w^2 + T_r^2) \quad (4.30)$$

where ε is the radiative emissivity of the water tank wall and σ is the Stefan-Boltzmann constant.

For the condenser exposed directly to room air, $\dot{Q}_{cnds r}$ is

$$\dot{Q}_{cnds r} = \frac{T_{cnds r} - T_r}{R_{cnds r}} \quad (4.31)$$

where T_{cnds} is the temperature of the exposed condenser and the thermal resistance network for R_{cnds} is shown in Figure 4.9.

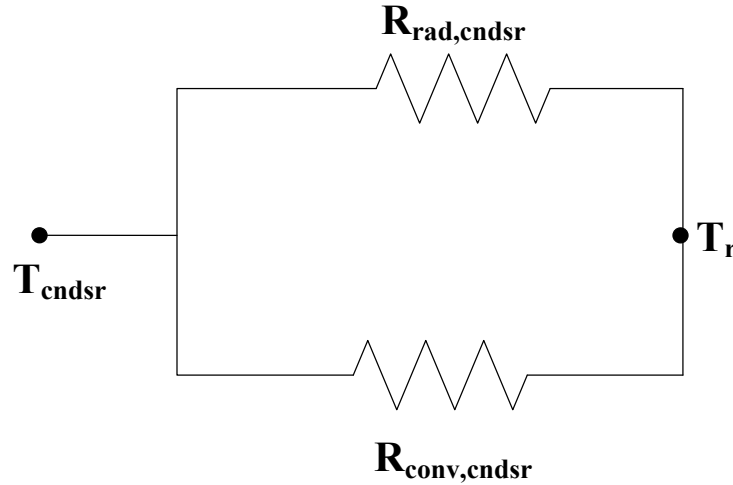


Figure 4.9. Thermal resistance network used to calculate \dot{Q}_{cnds} for a heating unit with the condenser exposed directly to room air.

Applying the resistance network shown in Figure 4.9, R_{cnds} is

$$R_{cnds} = \left(\frac{1}{R_{rad,cnds}} + \frac{1}{R_{conv,cnds}} \right)^{-1} \quad (4.32)$$

where $R_{conv,cnds}$ is

$$R_{conv,cnds} = \frac{1}{h_{cnds} A_{cnds}} \quad (4.33)$$

where A_{cnds} is the surface area of the condenser, and h_{cnds} is

$$h_{cnds} = \frac{k_r Nu_D}{D} \quad (4.34)$$

where D is the outside diameter of the condenser and Nu_D is [Incropera & Dewitt, 2011]

$$Nu_D = \left[0.60 + \frac{0.387 Ra_D^{1/6}}{\left(1 + (0.559 / Pr)^{9/16}\right)^{8/27}} \right]^2 \quad (4.35)$$

where Ra_D is [Incropera & Dewitt, 2011]

$$Ra_D = \frac{g\beta(T_3 - T_6)D^3}{\nu\alpha} \quad (4.36)$$

The radiative resistance from the condenser and the radiative heat transfer coefficient are

$$R_{rad,cndsr} = \frac{1}{h_{rad,cndsr}A_{cndsr}} \quad (4.37)$$

and

$$h_{rad,cndsr} = \varepsilon_{cndsr}\sigma(T_{cndsr} + T_r)(T_{cndsr}^2 + T_r^2) \quad (4.38)$$

where ε_{cndsr} is the radiative emissivity of the copper condenser.

The properties of the water in the tank and the air in the room were determined by interpolation from thermophysical property tables [Incropera & DeWitt 2011] at the average tank and room temperature over the course of that hour.

Useful gains that would have occurred in the full-scale prototype had mechanisms not been employed to reduce gains were estimated by characterizing system efficiency versus loss potential to insolation ratio (Figure 4.10). Experimental collector efficiency data in Figure 4.10 were collected during normal operation of the prototype during January and February of 2013 [Robinson & Sharp 2014]. Data points were selected around solar noon in accordance with ASHRAE standard 93 [2010] as described by Robinson et al. [2013]. Using the linear fit equation from Figure 4.10, system efficiency, without utilizing control mechanisms, was approximated using

$$\eta = 0.793 - 3.647 \frac{(T_s - T_a)}{S} \quad (4.39)$$

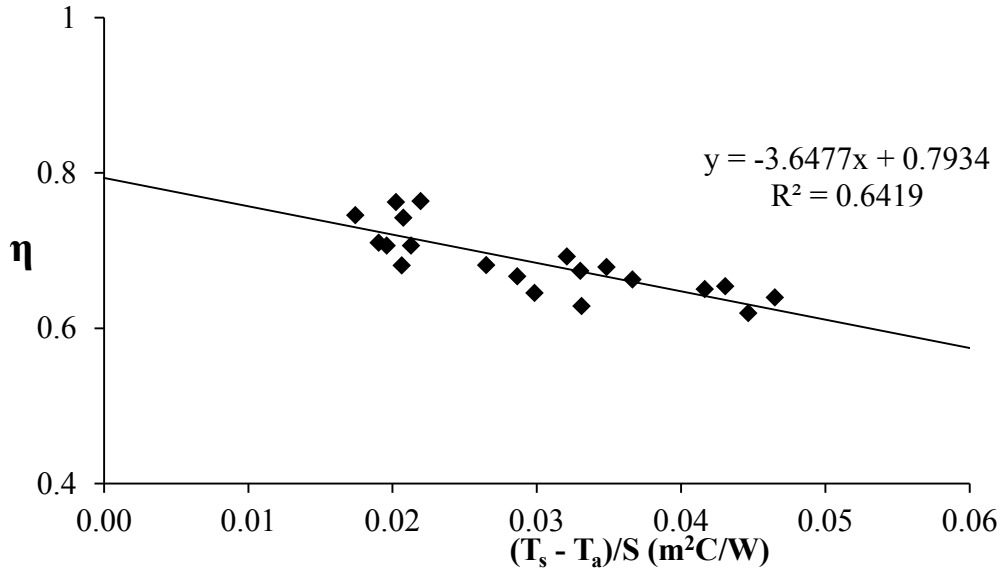


Figure 4.10. Collector efficiency data for the PSTF prototype using data collected during normal operation on January & February 2013.

4.3.5 Error Propagation

4.3.5.1 Bench-scale Experiments

Bench-scale thermal efficiency (Equation 4.15) depends on measurements of radiation received by the collector and storage temperatures (Equation 4.16). Each of these measurements was subject to digitization error in addition to rated uncertainty for the thermocouples and pyranometers. Therefore, the uncertainty in calculated system efficiency, μ_η , was found using

$$\mu_\eta = \sqrt{\left(\frac{\partial \eta}{\partial \Delta T_s} \mu_{\Delta T_s}\right)^2 + \left(\frac{\partial \eta}{\partial S} \mu_S\right)^2} \quad (4.40)$$

where ΔT_s is the storage temperature difference from Equation 4.16 and μ represents the uncertainty in temperature and radiation measurements, respectively.

For any arbitrary value of $\Delta T = T_1 - T_2$, we have

$$\left(\frac{\partial \Delta T}{\partial T_1}\right)^2 = \left(\frac{\partial \Delta T}{\partial T_2}\right)^2 = 1 \quad (4.41)$$

therefore the digitization uncertainty for any ΔT is

$$\mu_{\Delta T, digit/tc} = \sqrt{\left(\frac{\partial \Delta T}{\partial T_1} \mu_{T_1}\right)^2 + \left(\frac{\partial \Delta T}{\partial T_2} \mu_{T_2}\right)^2} = \sqrt{2\mu_T^2} = \sqrt{2}\mu_{digit/tc} \quad (4.42)$$

where μ_{digit} is the digitization error in each temperature measurement, which for the SCXI-1600 and SCXI-1102 modules was ± 0.027 K/level, and thermocouple uncertainty, μ_{tc} , is roughly 0.1 K up to approximately 100°C [Ripple et al., 1994]. Thus

$$\mu_{\Delta T_s} = \sqrt{\mu_{\Delta T, tc}^2 + \mu_{\Delta T, digit}^2} \quad (4.43)$$

resulting in an overall uncertainty in temperature measurement of 0.146 K.

The pyranometers have an overall error of $\pm 3\%$ of the measured value, as specified by the manufacturer Kipp and Zonen. Accordingly, the maximum μ_η occurred at the maximum value of radiation measured during the testing period - equal to 825.3 W/m² and resulting in a maximum μ_S of 24.76 W/m². Values for each derivative from Equation 4.39 are shown in Table 4.2. The derivative associated with change in storage temperature represented the greatest uncertainty while the derivative associated with radiation measurement represented the least uncertainty. The estimated maximum uncertainty in system efficiency from Equation 4.31 was $\pm 4.57\%$.

Table 4.2. Value for each derivative associated with overall uncertainty in calculated system efficiency for the bench-scale experiments.

Derivative	Value
$\partial\eta/\partial\Delta T_s$	0.2673
$\partial\eta/\partial\Delta S$	-0.0009

4.3.5.2 Full-scale Prototype

□

System thermal efficiency (Equation 4.15) depended on measurements of storage, room and condenser temperatures (Equations 4.18, 4.19 and 4.31) and of insolation. Therefore, the uncertainty in calculated system efficiency, μ_η , was found using

$$\mu_\eta = \sqrt{\left(\frac{\partial\eta}{\partial\Delta T_s} \mu_{\Delta T_s}\right)^2 + \left(\frac{\partial\eta}{\partial\Delta T_{sr}} \mu_{\Delta T_{sr}}\right)^2 + \left(\frac{\partial\eta}{\partial\Delta T_{cnds r}} \mu_{\Delta T_{cnds r}}\right)^2 + \left(\frac{\partial\eta}{\partial S} \mu_S\right)^2} \quad (4.44)$$

where ΔT_s is the storage temperature difference from Equation 4.18, ΔT_{sr} is the temperature difference between storage and room ($T_s - T_r$) from Equation 4.19, $\Delta T_{cnds r}$ is the temperature difference between the exposed condenser and room ($T_{cnds r} - T_r$) from Equation 4.31. Uncertainties for temperature difference and pyranometer measurements are the same as section 4.2.5.1. Values for each derivative from Equation 4.44 are shown in Table 4.3. The estimated uncertainty in system efficiency was $\pm 3.90\%$.

Table 4.3. Value for each derivative associated with overall uncertainty in calculated system thermal gains for the full-scale prototype .

Derivative	Value
$\partial\eta/\partial\Delta T_s$	0.3132
$\partial\eta/\partial\Delta T_{sr}$	0.0017
$\partial\eta/\partial\Delta T_{cnds r}$	0.0026
□ $\partial\eta/\partial\Delta S$	-0.0010

□

□

4.4. Chapter 4 Results & Discussion

4.4.1 Bench-scale Experiments

Modifications to the baseline bench-scale experiment increased system thermal efficiency to 89.1% (up from 85.1% obtained by Albanese et al. [2013]). Bench-scale experiments revealed a decrease in average system thermal efficiency (to 82.2%) of 6.9% when the evaporator and condenser sections were leveled. This decreased efficiency was applied to all simulations involving the switching mechanism.

4.4.2. Simulations

4.4.2.1. Baseline Simulations

Baseline annual heating, cooling and total loads without the heat pipe wall are shown in Figure 4.11 for each of the four locations representing different climate types. Madison and Rock Springs have substantially colder winters and higher heating loads, while Louisville and Albuquerque have warmer summers and higher cooling loads. It is evident that the heating load dominates in all locations.

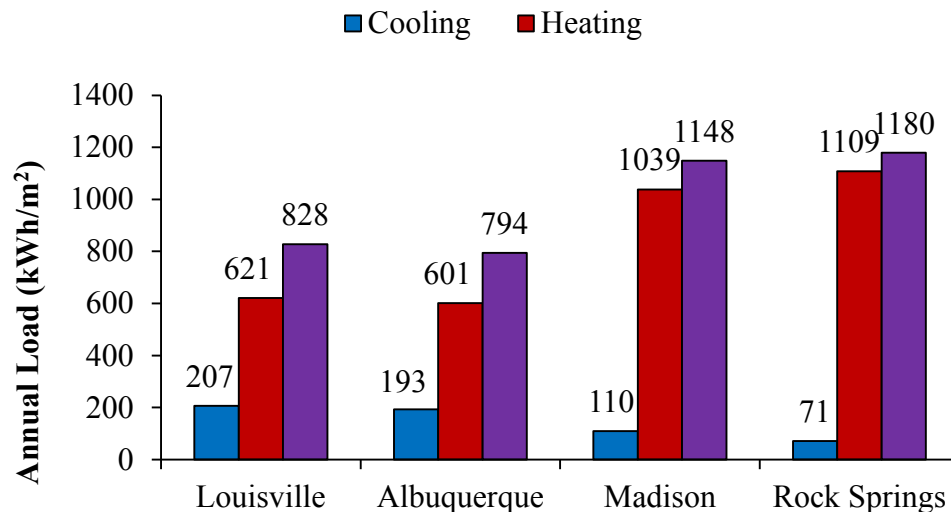


Figure 4.11. Annual loads for four locations without the heat pipe wall.

The effect of indoor comfort temperature range is shown in Figure 4.12, in which simulated annual unwanted gains ($q_{a,uwg}$), auxiliary heating ($q_{a,aux}$) and total energy (q_{total}) loads in Louisville are plotted for a building with the heat pipe wall. Without reduction mechanisms, unwanted gains in Figure 4.12 are larger than the baseline cooling load (Figure 4.11), and increase as the comfort temperature range is restricted. With the narrowest comfort range, the total load is larger with the heat pipe system than without (Figure 4.11). A 1.1 °C increase in acceptable range – from 20.6 – 21.7°C to 20.0 – 22.2°C – decreased the annual load by 10.2%. Increasing the range to 18.3 – 23.9°C decreased the annual load an additional 15.4%. Results were similar in the other climates. All of the following results use the larger 18.3 – 23.9°C range.

Energy use in buildings with heat pipe walls without mechanisms to reduce unwanted gains are shown in Figure 4.13. All components of energy are normalized by baseline totals without the heat pipe system (Figure 4.11). The heat pipe wall serves a substantial portion of the heating load, but the cooling load more than doubles in all locations due to unwanted gains from the system during the cooling season. In spite of the increased cooling load, the total load in each location is lower with the heat pipe system than without.

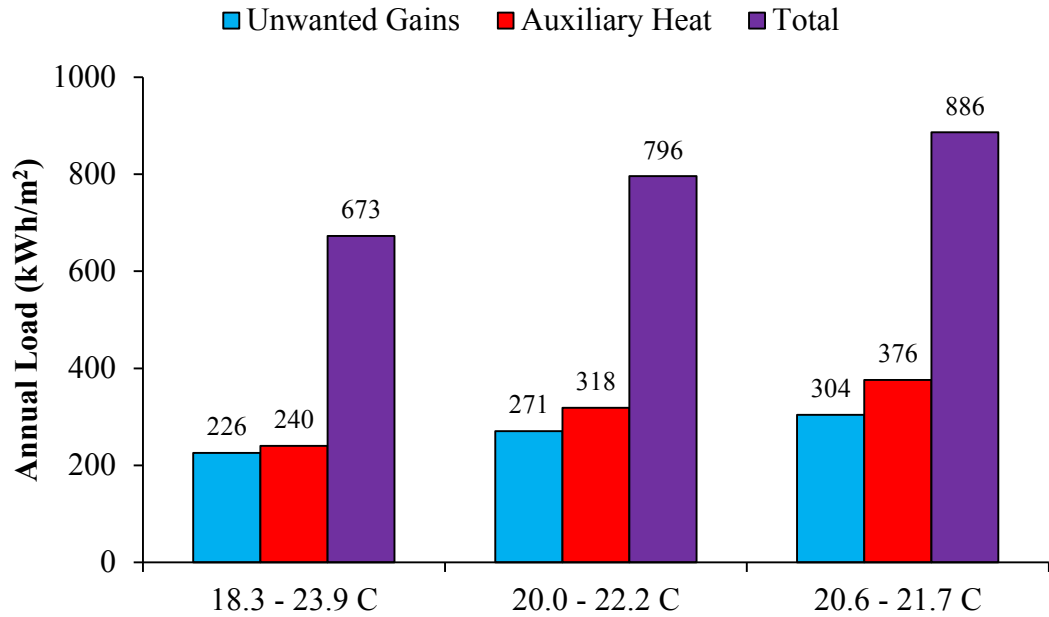


Figure 4.12. Annual unwanted gains, auxiliary heating and total energy load for Louisville utilizing the heat pipe wall (without reduction mechanisms) for room comfort ranges of 18.3-23.9°C (65-75°F), 20.0-22.2°C (68-72°F) & 20.6-21.7°C (69-71°F)

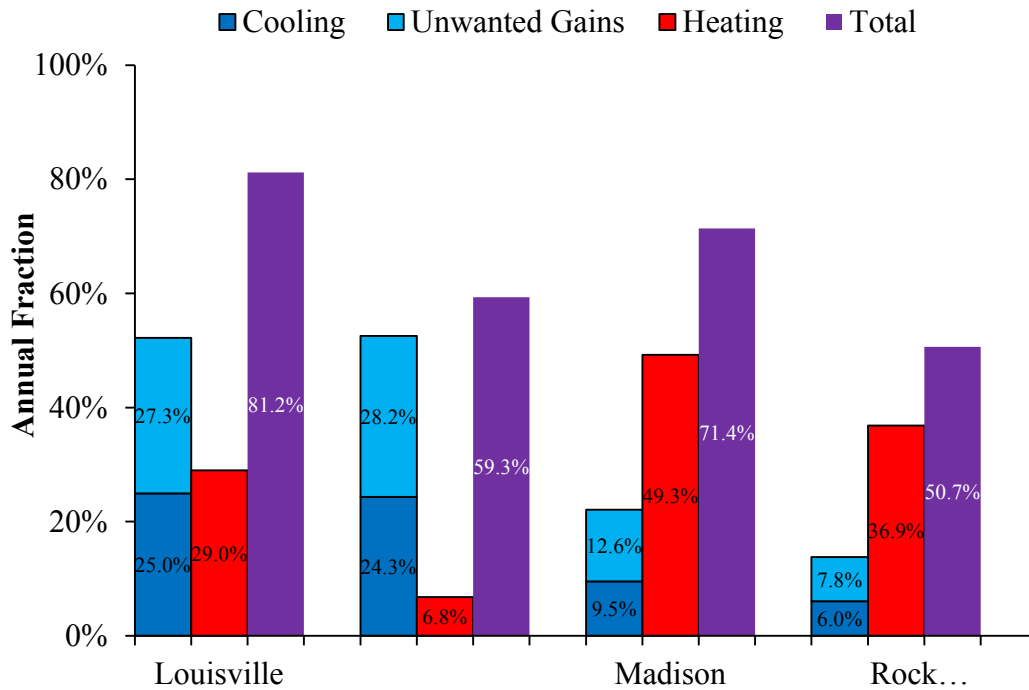


Figure 4.13. Annual loads for four locations with the heat pipe wall.

4.4.2.2. Control Strategies

For the seasonal control strategy, simulations showed that any month with $SD \geq 0.6$ should be included as part of the cooling season to minimize auxiliary energy use. This rule worked for all eight locations, suggesting that SD may be a ‘universal’ parameter that can be applied to a wide range of climates for quick assessment of its optimal cooling season. Cooling seasons, based on SD, for each of the eight locations are shown in Table 4.4.

The control strategy based on ambient temperature provided the lowest levels of unwanted gains for all locations and mechanisms (Figure 4.14). Even though auxiliary heat requirements were higher than for other control strategies in most cases, ambient temperature-based control produced the lowest total loads.

Table 4.4. Cooling season for eight locations based on SD ratio.

Location	Cooling Season
Albuquerque, NM	May - September
Boston, MA	June - September
Chicago, IL	June - September
Denver, CO	June - September
Louisville, KY	June - September
Louisville, KY	May - September
Madison, WI	June – August
Rock Springs, WY	July - August
Seattle, WA	July - August

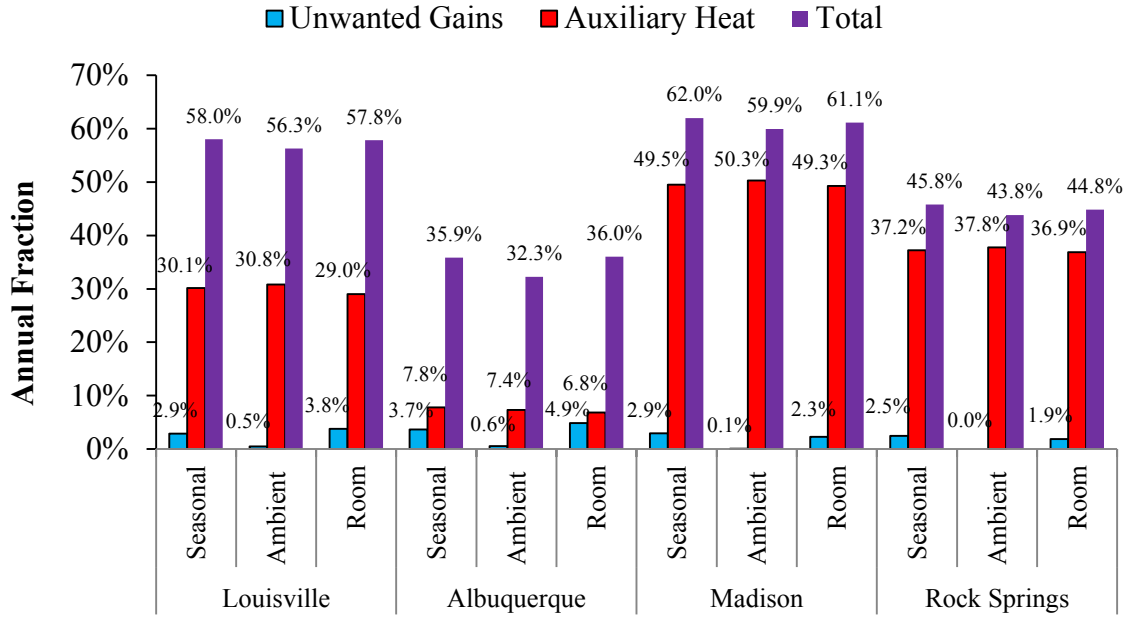


Figure 4.14. Annual loads for four locations for each control strategy using the cover mechanism.

Results for ambient temperature-based control in Louisville are shown in Figure 4.15 with each mechanism and their practical combinations. Trends in performance of mechanism combinations for the other three locations were similar to Louisville. The best single mechanism was the valve. The cover mechanism accumulated some unwanted gains during periods in which high ambient temperatures resulted in convective and conductive gains to the absorber. With no valve to stop two-phase heat transfer, small amounts of heat were occasionally transferred to the system even when insolation was eliminated by the cover. On the other hand, the valve mechanism was simulated as complete elimination of two-phase heat transfer within the heat pipes. Even though conduction along the adiabatic section pipe wall remained, simulated unwanted gains were near zero for the year.

The switching mechanism provided similarly reduced unwanted gains to that of the cover and valve. However, leveling the evaporator and condenser sections of the heat

pipe to accommodate switching reduced performance in the heating mode and resulted in higher auxiliary requirement, thus a 3.2% and 4.1% higher annual load than the cover and valve mechanisms, respectively. Also, while the switching mechanism was effective in minimizing unwanted gains, annual heat transfer out of the system (Equation 4.8) only increased by no more than 1 Wh/m² in all locations and for each control strategy. The heat pipe system was designed for heating with features, such as low IR emittance and transmittance for the selective absorber and glass cover, respectively, that reduce the potential performance of the system for the cooling mode. In addition in some climates, consistently warm ambient air during the cooling season greatly limited cooling potential. These limitations rendered the switching mechanism a poor choice in all locations. The ambient temperature based control strategy only allowed cooling when outdoor temperature was greater than 65°F. Forecast control based on prediction of cooling needs might better utilize the capability of the switching mechanism, particularly if optical properties of the system were more favorable for cooling. The combinations of mechanisms most effective in reducing annual load were those involving the valve (valve and cover, and valve and shading), but these combinations did not reduce the load below that of the valve alone.

The total annual space-conditioning loads for each of the four locations using the heat pipe wall with the best control strategy (ambient temperature) are shown in Figure 4.16. This graph presents the clearest comparison of mechanisms based on total annual energy use. It is evident that the valve mechanism, as simulated, produces the lowest total loads in all locations. The cover matches the valve within one percentage point. Switching produces higher loads in all locations except Albuquerque. This was because high

performance from the heat pipe system in sunny Albuquerque results in a low $q_{a,aux}$ requirement, thus the reduction in system performance when the evaporators and condensers are leveled doesn't have as much significance on q_{total} as it does in locations with smaller solar fractions. Shading is only competitive with the cover and valve in Rock Springs, the climate with the lowest cooling load (Figure 4.11).

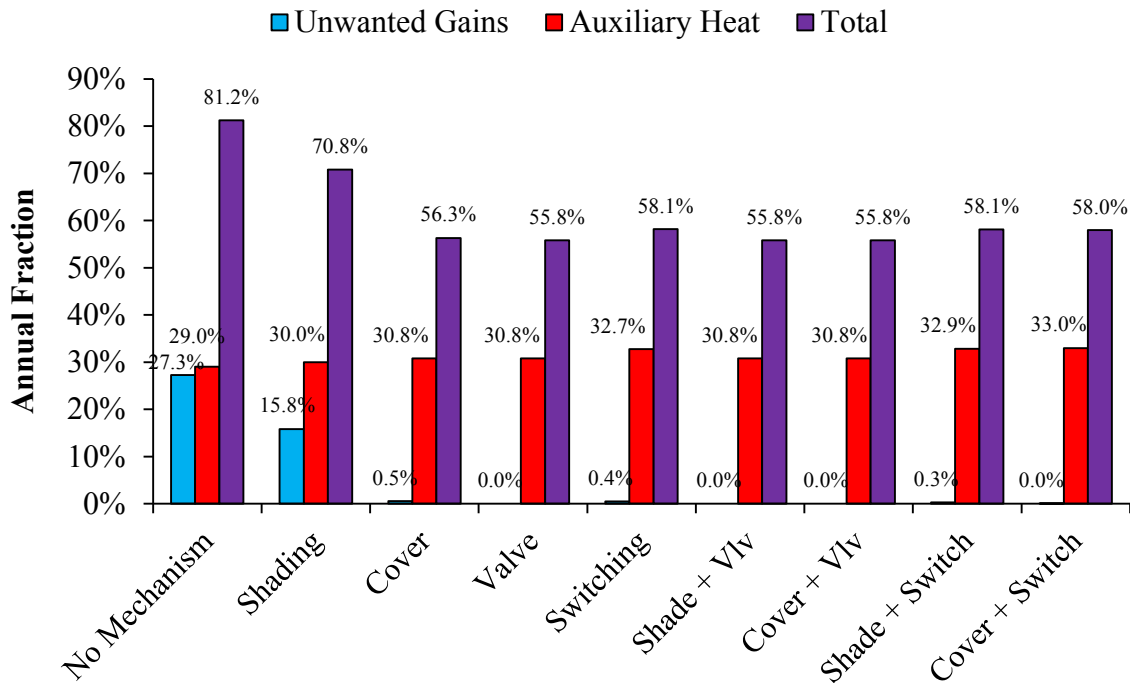


Figure 4.15. Annual loads in Louisville for unwanted gains reduction mechanisms with ambient temperature based control.

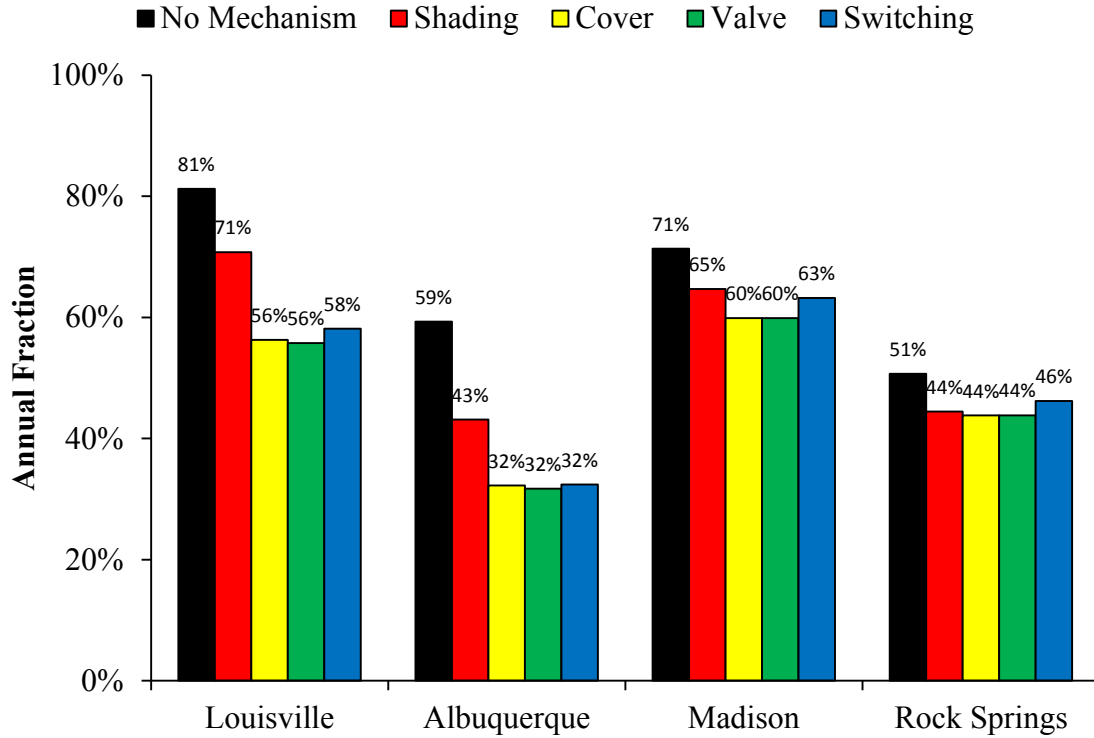


Figure 4.16. Total annual loads with different mechanisms with ambient temperature-based control strategy.

4.4.3 Full-scale Experiments

System efficiency, η , from 9am to 5pm for three consecutive days, is shown in Figures 4.17 – 4.19 for the valve mechanism, cover mechanism, and combination of valve and cover, respectively. η would be zero if the mechanisms were perfectly effective, but as can be see in the figures, some heat transfer to the interior remains. Figures 4.17 – 4.19 also show estimated efficiencies had control mechanisms not been used (Equation 4.16). Unlike the simulations, the valve (Figure 4.17) was less effective in the experiments, and the cover and valve combination (Figure 4.19) provided noticeable benefits relative to each single mechanism.

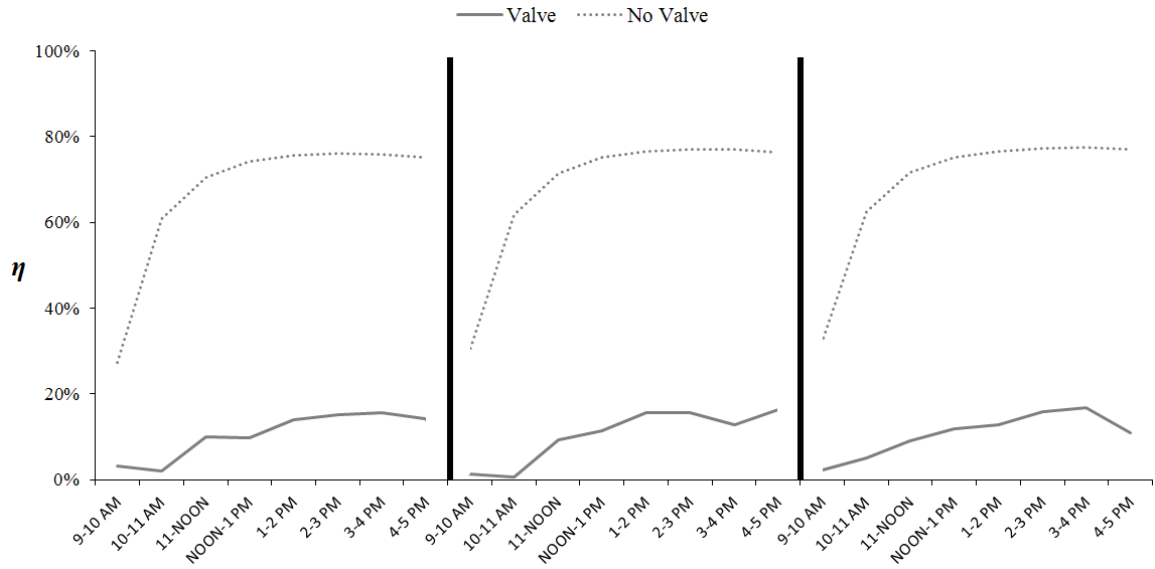


Figure 4.17. Prototype efficiency with and without the valve mechanism on August 22 - 24, 2013.

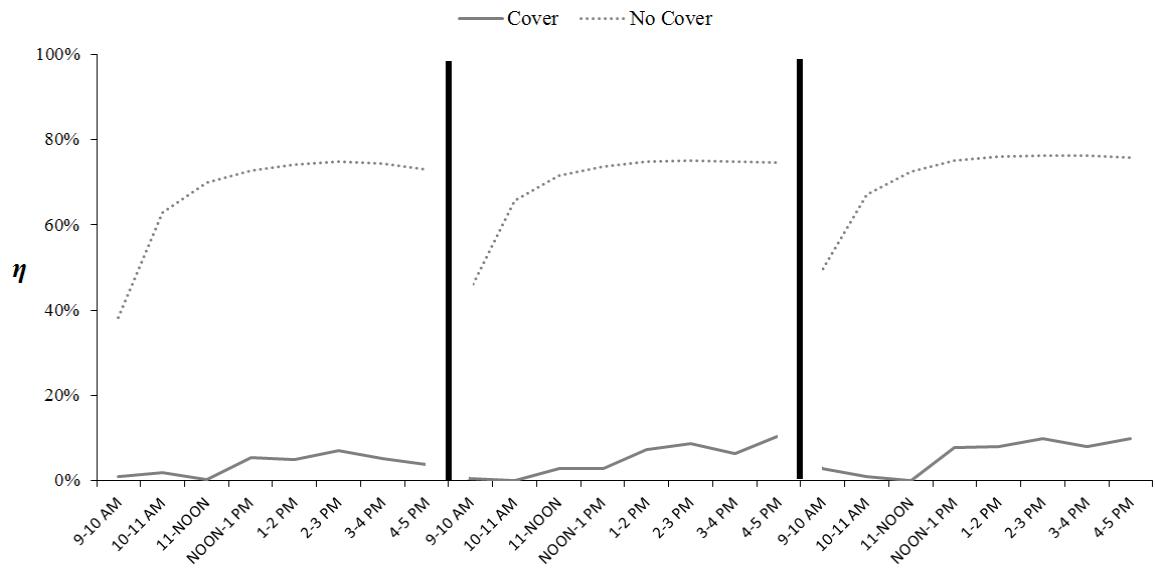


Figure 4.18. Prototype efficiency with and without the cover mechanism on September 9 - 11, 2013.

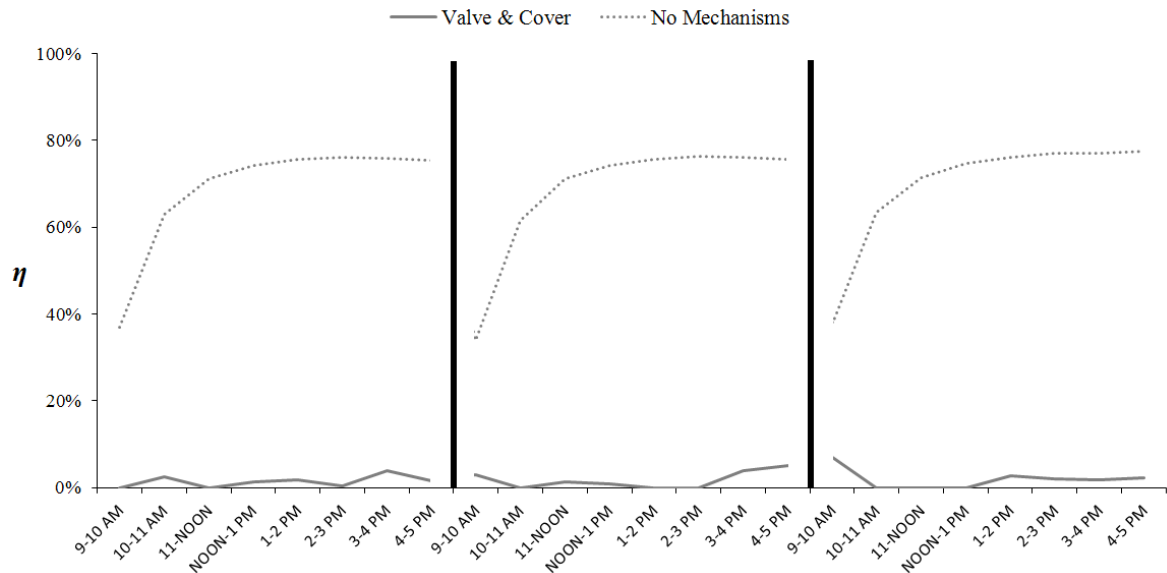


Figure 4.19. Prototype efficiency with and without the combination of valve and cover mechanisms on August 28 - 30, 2013.

For each three-day period, system thermal gains were reduced by an average of 83.8% for the valve mechanism (Figure 4.17), 93.2% for the cover mechanism (Figure 4.18), and 98.1% when combining the two mechanisms (Figure 4.19). These experimental values are compared to simulated annual reductions in unwanted thermal gains using the same mechanisms in Figure 4.20. Because of the difference in time periods and weather data for the experiments and simulations, this comparison is qualitative, but nonetheless provides another indication of the relative effectiveness of the mechanisms as tested. While experimental reductions for the cover and the combination were within the simulated range for all three strategies, experimental reductions using the valve mechanism were lower than reductions reflected in simulations. One possible cause of the smaller reduction is that, although the valve and the adiabatic section were insulated, some heat transfer to the room may have occurred. In particular, each valve

was installed between the rubber adiabatic section and the copper condenser section, and two-phase heat transfer likely still occurred between the evaporator and the lower face of the valve. Therefore, high temperatures at the lower face of the valve (hourly average absorber temperatures were as high as 107.5°C (225.4°F) during this testing period) resulted in additional thermal gains to the room and storage via conduction through the valve and to the condenser.

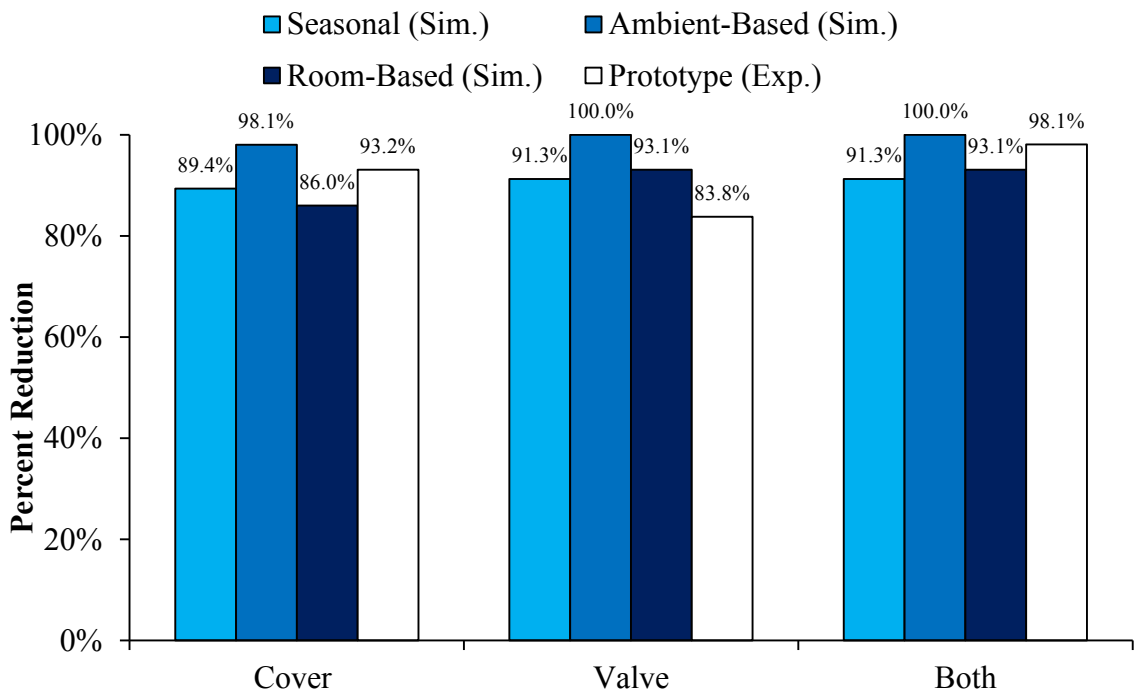


Figure 4.20. Simulated annual and experimental three-day unwanted gains reductions in Louisville.

To investigate whether heat was transferred through the valve to the condenser section, temperatures of the condenser exposed to air were compared on similarly sunny days when the valve was closed and open (Figure 4.21). While the condenser temperature does rise slightly during insolation with the valve closed, the rate of rise is much greater with the valve open. This suggests that thermal gains to the condenser were a result of

conduction heat transfer along the copper pipe wall, instead of the much higher two-phase heat transfer when the valve is open. Consequently, it is expected that a system design in which the valve is installed in the middle of the rubber adiabatic section would further reduce unwanted gains since heat transfer downstream of the valve would be restricted by thermally resistive rubber. The low temperature rise in the condenser with the closed valve also suggests that greater heat may flow to the room from the potentially very hot section of the heat pipe between the absorber and the closed valve.

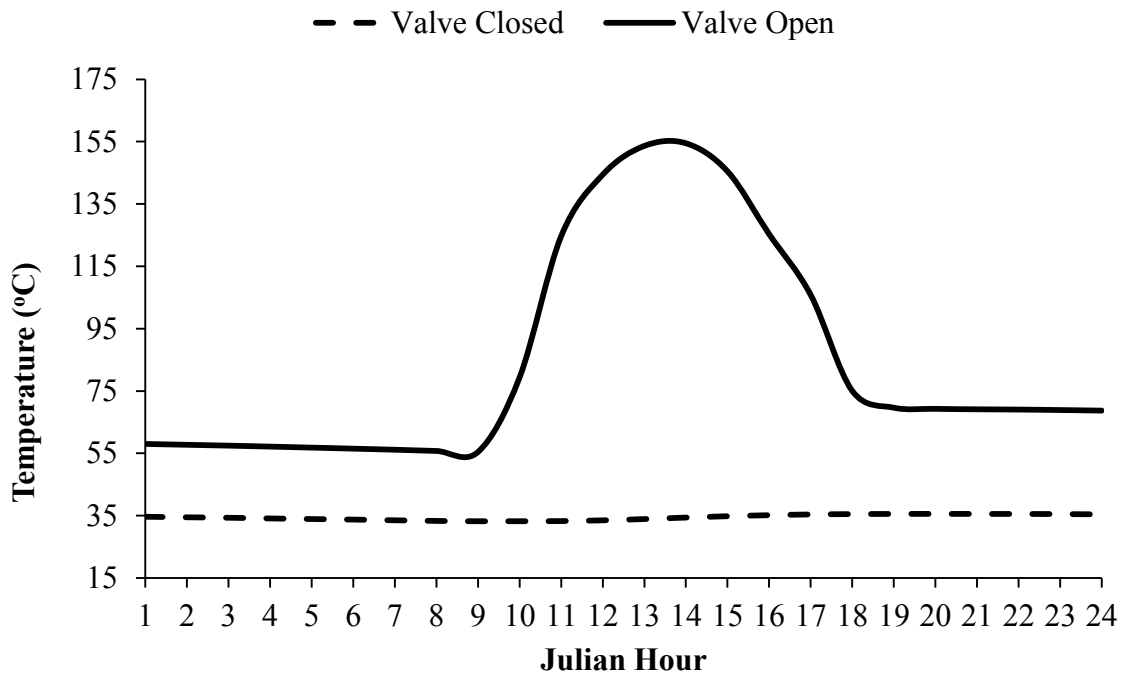


Figure 4.21. Prototype exposed condenser temperatures using the valve mechanism on August 22, 2013, and without the valve mechanism on January 3, 2013.

4.5. Chapter 4 Conclusions

Computer simulations show that maximum reductions in the overall annual space heating and cooling loads are achieved when the heat pipe augmented solar wall utilized a control strategy based on ambient temperature. The best simulated control mechanism

was the valve, which essentially eliminated unwanted gains and produced the lowest total annual load. Close behind were the cover and switching, which also nearly eliminated unwanted gains. The cover required the same auxiliary heating as the valve, but switching required about 2% more due to performance reductions during the heating season. Combining valve or cover with other mechanisms did not significantly improve simulated performance. Shading provided much lower reduction in unwanted gains.

Experimental results confirmed the performance of the cover, but suggested that a small amount of heat was still transferred when the valve was closed. Changes in valve placement and heat pipe design may reduce, but not entirely eliminate, closed-valve heat transfer, for instance by adding a section of low conductivity rubber tubing between the valve and the condenser.

With the valve and cover providing nearly the same performance, practical implementation of automatic control becomes a consideration. Five valves (one in each heat pipe) would be straight-forward to actuate, would require little additional space and the components would be located indoors and out of the weather. On the other hand, an automated cover is a single, but large, mechanism that must withstand weather conditions. An electrochromic surface could potentially be used to block solar radiation without moving parts. Both cover and valve mechanisms provide opportunities for modulated, rather than on/off control, which could be advantageous, particularly in the fall and spring when heating and cooling loads can occur within short time periods. Independent control of the heat pipe with exposed condenser might be especially beneficial due to its fast response.

The heat pipe augmented solar wall, analyzed with respect to heating only, exhibits positive returns with increasing solar collection area. However, as collector area increases, so does the potential for unwanted gains during the cooling season, which if reduction mechanisms are not incorporated, will at some threshold begin to increase overall annual load. The heat pipe system shares this common limitation with other passive solar systems. By applying the mechanisms identified in this study, freedom is returned to use larger collector area without increasing unwanted gains to unacceptable levels, and the overall annual load can be reduced to much lower levels than without the mechanisms. Previous studies have shown that lower values of LCR can serve more than 90% of the annual heating load in many locations throughout the U.S. [Robinson & Sharp, 2014]. Research addressing renewable, passive solutions for combining heating and cooling from alternative sources is the next step towards full realization of net-zero energy space conditioning of buildings.

CHAPTER 5: U.S. SPACE COOLING POTENTIALS FOR AMBIENT SOURCES WITH THERMAL ENERGY STORAGE

5.1. Chapter 5 Overview

The potential of ambient thermal sources, including ambient air at dry-bulb and wet-bulb temperatures, ground and night-sky radiant temperatures, to serve building cooling loads was evaluated from TMY3 weather data for US climates. Three different cases were considered: (1) annual potentials, disregarding thermal storage, (2) diurnal storage and (3) storage capacity necessary to serve the entire annual load. The storage capacity was determined by identifying the largest load occurring during spans of time without ambient cooling potential. The sky had cooling potential every night in all 11 American Society of Heating, Refrigeration, and Air-Conditioning Engineers (ASHRAE) climate sub-zones in the continental US, while ground temperature had continuous cooling potential for all but the southernmost locations. Additionally, the thermal storage required to meet the entire annual cooling load with night sky radiation was quite feasible for a building with low overall envelope losses.

5.2. Chapter 5 Introduction

The residential, commercial, industrial and transportation sectors account for 22%, 19%, 31% and 28% of U.S. energy demand, respectively [EIA, 2011]. Building space heating and cooling represents 54% of the residential load, 18% of the commercial load, 9% of the industrial load and an insignificant fraction of the transportation load [EIA

2011]. Therefore, supplanting fossil fuel based energy production for building space conditioning with alternative energy solutions would account for nearly 19% of total U.S. energy demand.

While solar energy is an excellent universal source for space heating applications [Susheela and Sharp, 2001; Balcomb, 2008; Albanese et al., 2012; Robinson et al., 2013], other ambient energy sources may be more appropriate for space cooling applications. The ambient sources that could provide a cold sink for space cooling purposes include ambient air at dry-bulb temperature, wet-bulb air temperature (for evaporative cooling), ground temperature (geothermal), and cool night sky radiant temperature.

In many traditional buildings, dry-bulb air has been used for ventilation and for cooling, including breezeways in dogtrot southern homes and porches that exclude insolation and locally cool the air surrounding the home. Considerable potential exists for increased energy savings by supplanting manual ventilation with automatic control [Agas and Matsaggos, 1994; Santamouris et al., 1997]. Wet-bulb temperature provides greater cooling potential than dry-bulb and is utilized in current evaporative coolers. Because it involves adding moisture to the space, effective use of direct evaporative cooling is limited to locations where humidity is significantly lower than the upper limits of human comfort. Across most of the US, ground temperature at sufficient depths remains below indoor comfort temperatures, and earth-to-air heat exchangers have the potential to provide the entire cooling load for a building [Mihalakakou et al., 1994; Mihalakakou et al., 1995; De Paepe and Janssens, 2003].

Night sky radiators utilize radiation through the atmosphere to the cold (near absolute zero) temperature of outer space to provide cooling. Catalanotti et al. [1975] constructed

a selective radiator using polyvinyl fluoride (TEDLAR) deposited on aluminum with a polyethylene cover, and reported 10–15 °C depression of the radiator surface temperature below ambient air temperature. Kimball [1984] obtained experimental measurements for three different night sky radiators, each covered with polyethylene, constructed with bare aluminum, white TiO₂ paint and black paint, respectively. Similar measurements were also obtained with a fourth radiator that had an uncovered, black painted surface. Depressions below air temperature under stagnation conditions (no energy addition to the radiator due to flow from an external source) of 6 °C and 2.5 °C were observed with the aluminum and black uncovered radiators, respectively. Depressions for the white and black paint covered radiators were about 11 °C and 6 °C, respectively. The performance of a radiation cooling system capable of a mean nightly cooling rate of 80 W/m² over an 8-hour operating period was experimentally investigated by Erell and Etzion [1996]. The system made use of a single 2.2 x 1.3 meter, commercially available flat plate solar water heater, but with the glazing removed. Al-Nimr et al. [1998] constructed a radiating panel made of 1500 x 400 mm mild steel plates, with a 40 µm polyethylene cover and a rockwool back-insulation and a pump circulating water to a 120-liter storage tank. Results showed that the radiation panel was able to reduce temperature of the water by 15 °C under spring weather conditions in Irbid, Jordan.

The focus for this study was on quantifying the potential for these ambient energy sources to serve building cooling loads for the range of climates throughout the U.S. For each climate zone, three different cases were evaluated. Cooling potentials for each ambient source were calculated (1) without thermal storage and (2) with diurnal storage. Finally, (3) the storage capacity necessary to serve the entire annual cooling load was

determined (enough capacity to serve the span of time with the largest load during the year when no ambient cooling potential existed).

The prospects for cooling by ambient sources are exemplified by Figure 5.1, which displays the average monthly high and low temperatures in Louisville, KY for each ambient source in relation to the lower and upper room comfort limits (defined as 68 – 72 °F). Monthly low dry-bulb and wet-bulb temperatures may be suitable for cooling from August to June, but the largest cooling loads occur during July when cooling from these sources is unavailable. Geothermal temperature (56.5 °F) remains a constant potential for cooling all year long, and radiant night sky temperatures, both monthly highs and lows, appear to offer the greatest cooling potential during the cooling season, reaching a maximum average monthly high temperature – slightly above ground temperature – during the hottest month of July. These simplified comparisons suggest the usefulness of a comprehensive evaluation of ambient energy source potential across the U.S.

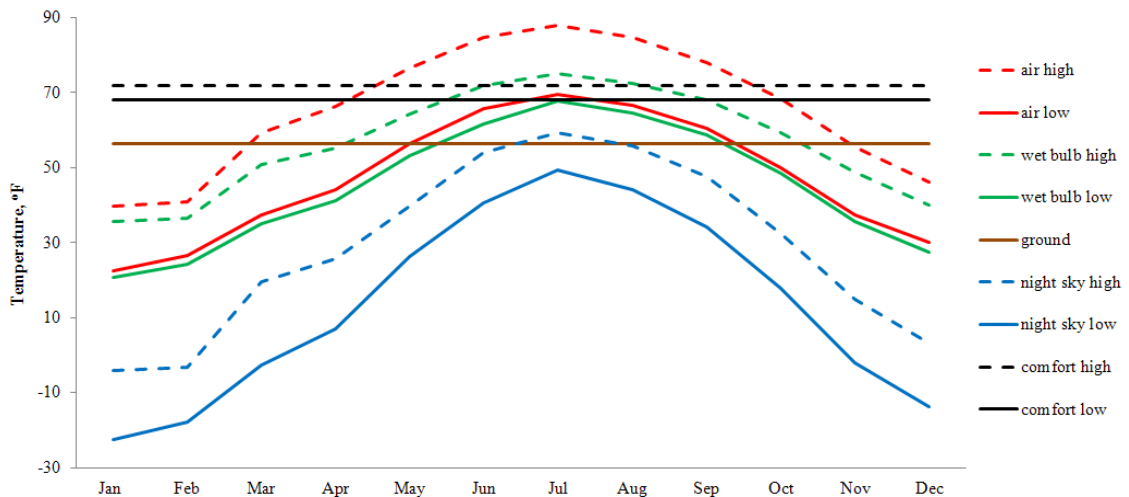


Figure 5.1. Average monthly temperatures of ambient energy sources relative to indoor comfort temperatures in Louisville, KY.

5.3. Chapter 5 Methods

Cooling potentials from ambient sources were evaluated by three different methods. First, total annual potentials were evaluated, which may be the most difficult to utilize because of the possibility of long delays between the harvesting of thermal energy and its utilization. Second, potentials and demands were compared on a daily basis, which would allow a relatively small amount of thermal mass to store the thermal energy until it was needed later the same day. This comparison resulted in estimates of the fraction of the cooling load that could be met with diurnal storage. Third, the thermal mass required to serve the largest cooling load over each span of time without ambient cooling potentials was identified. The span with the largest cooling load determined the thermal mass necessary to serve the entire annual load. Algorithms for calculating cooling potentials from ambient sources were developed in MATLAB, and the results were written to an Excel spreadsheet. TMY3 weather data, including dry-bulb ambient temperature T_{db} , dew-point temperature T_{dp} , relative humidity ϕ , and barometric pressure P , were used for 814 locations throughout the nation (TMY3 data represent a single year of weather typical of measurements from the 1991-2005 National Solar Radiation Data Base and, thus, do not include extremes that may occur on an irregular basis, nor climate change since 2005 [Wilcox and Marion, 2008]). US maps representing annual cooling loads and potentials were created for visual assessment (Maptitude, Caliper Corporation, Newton, MA).

5.3.1. Annual Cooling Potential

Cooling loads for each hour were calculated using the degree-day method given by

$$CDH = (T_a(m, n) - T_b)^+ \quad (5.1)$$

For this study, base temperature T_b was set at the commonly used value of 65°F [NOAA National Climatic Data Center, 2013]. The baseline annual cooling load was calculated as

$$CDD = \frac{\sum_{n=1}^{365} \left[\sum_{m=1}^{24} CDH(m, n) \right]}{24} \quad (5.2)$$

The degree-day method was also used to evaluate the annual cooling potential for ambient sources. Potential for cooling exists when the ambient source temperature T_{as} is lower than $T_{c,hi}$, where the indoor comfort temperature range was defined as $T_{c,lo} = 68^\circ\text{F}$ and $T_{c,hi} = 72^\circ\text{F}$ (This conservatively narrow range corresponds to > 90% acceptance for indoor temperature control in cool climates [ASHRAE standard 55-204]. The range can be seen as high as $\pm 6^\circ\text{F}$ for 80% acceptance. Consistent with the simple estimates of this study, the range was taken as a constant, whereas there is considerable evidence that the perception of comfort temperature follows monthly mean ambient temperature, particularly for naturally conditioned buildings [Nicol and Humphreys, 2002].) Therefore, annual ambient cooling capacity is

$$ACDD = \frac{\sum_{n=1}^{365} \left[\sum_{m=1}^{24} (T_{c,hi} - T_{as}(m, n))^+ \right]}{24} \quad (5.3)$$

Wet-bulb temperature, T_{wb} , is the minimum temperature that can be achieved by evaporative cooling of a water-wetted, ventilated surface [Jensen et al., 1990]

$$T_{wb} = \frac{\gamma T_a + \delta T_{dp}}{\gamma + \delta} \quad (5.4)$$

where γ is

$$\gamma = 0.00066 * P \quad (5.5)$$

where P is atmospheric pressure in kPa, and δ is

$$\delta = \frac{4098 * e}{(T_{dp} + 237.3)^2} \quad (5.6)$$

and e is

$$e = \frac{\phi}{100} * 0.611 \exp\left(\frac{17.27 T_a}{T_a + 237.3}\right) \quad (5.7)$$

Kasuda [1965] derived a correlation for ground temperature T_g as a function of time of year and depth below the surface, given by

$$T_g = T_{mean} - T_{amp} * \exp\left(-Z \sqrt{\frac{\pi}{365\alpha}}\right) \cos\left[\frac{2\pi}{365}\left(t_{year} - t_{shift} - \frac{Z}{2} \sqrt{\frac{365}{\pi\alpha}}\right)\right] \quad (5.8)$$

At large depth Z , T_g asymptotes to a constant equal to the annual average dry-bulb temperature (T_{mean}) for that location. Florides and Kalogirou [2004] found that ground temperatures measured in a borehole equaled T_{mean} within 0.5 °C for depths of two meters or greater. T_g at these depths thus offers cooling potential in locations where the annual average ambient temperature is less than the upper comfort limit. T_g was estimated by averaging hourly ambient temperatures from TMY3 data.

Sky temperature, T_s , was calculated as [Duffie and Beckman, 2006]

$$T_s = T_{db} \left[0.711 + 0.0056 T_{dp} + 0.000073 T_{dp}^2 + 0.013 \cos(15t)\right]^{1/4} \quad (5.9)$$

where t is the number of hours from midnight. During daylight hours, absorption of solar energy overpowers emission to the sky for typical radiator materials, so sky cooling potential was calculated from sunset to sunrise. (This point will be revisited in the Conclusions section.)

For this study, 11 US cities, one from climate zone 1 and one from each respective climate sub-zone in zones 2-6, were chosen to give a broad perspective of the capabilities of ambient sources to meet cooling loads across the continental US (Table 5.1). Among the eight ASHRAE-defined climate zones [DOE, 2010], most of the continental US is represented by climate zones 2-6. The very hot climate zone 1 represents the southern tip of Florida. Very cold climate zone 7 (northern tip of Maine, north-central US, and high elevation locations in the Rocky Mountains) and subarctic climate zone 8 (majority of Alaska) were not considered due to the small cooling loads there. Sub-zones “A” and “B”, for humid and dry climates, respectively, were included for each zone, with the exception of climate zone 1 which is exclusively humid. The selected cities embody a range of climate characteristics pertinent to this study, including: (i) seasonal ambient temperature that affects annual cooling loads, (ii) diurnal temperature swings that affect the capability of one-day thermal storage to serve that day’s cooling load, (iii) humidity that affects T_{wb} and (iv) sky clearness that affects T_s .

Table 5.1. Description of ASHRAE-defined climate subzones within the continental US, and the representative cities used for this study.

Climate Zone	Description	City
1A	Very Hot & Humid	Miami, FL
2A	Hot & Humid	New Orleans, LA
2B	Hot & Dry	Phoenix, AZ
3A	Warm & Humid	Atlanta, GA
3B	Warm & Dry	Los Angeles, CA
4A	Mixed & Humid	Louisville, KY
4B	Mixed & Dry	Albuquerque, NM
5A	Cool & Humid	Boston, MA
5B	Cool & Dry	Denver, CO
6A	Cold & Humid	Madison, WI
6B	Cold & Dry	Rock Springs, WY

For each city and ambient source, an ambient potential to cooling load ratio (*ALR*) was calculated as

$$ALR = \frac{ACDD}{CDD} \quad (5.10)$$

ALR represents the relative potential for serving the cooling load from the respective ambient source, but not the actual performance, which depends on system design and control strategies. Importantly, *ALR* neglects phase lags between source and load and the associated need for thermal storage.

5.3.2. Cooling Potential with Diurnal Storage

The effects of limited thermal storage were taken into account by calculating a daily ambient source potential

$$f_{as,ld} = \frac{\sum_{m=1}^{24} (T_{c,hi} - T_{as}(m,n))^+}{\sum_{m=1}^{24} (T_a(m,n) - T_b)^+} \quad (5.11)$$

so that $f_{as,1d}$ suggests the fraction of the daily cooling load that could be met by the ambient source, $f_{as,1d}$ is limited to 1 when the ambient potential exceeds the daily load, and is limited to zero when either ambient potential or cooling load is not present on a particular day. An annual ambient source fraction was calculated from the daily fractions

$$F_{as,1d} = \frac{\sum_{n=1}^{365} \left(f_{as,1d}(n) \sum_{m=1}^{24} (T_a(m,n) - T_b)^+ \right)}{24CDD} \quad (5.12)$$

Consequently, $F_{as,1d}$ is an indicator of the potential of ambient energy systems with “one day’s worth” of thermal storage to serve the annual cooling load.

5.3.3. Storage Capacity for 100% Ambient Source Cooling

The requirements for storage of ambient energy to meet the entire annual load were also estimated. This process began by searching hourly data for the degree-day loads, CDD_{nas} , during spans of time, t_{nas} , when ambient source temperature was too high to be available for cooling, $T_{as} > T_{c,hi}$

$$CDD_{nas} = \sum_{m=1}^{t_{nas}} (T_a(m,n) - T_b)^+ \quad (5.13)$$

The maximum time span, $t_{nas,max}$, during which the ambient source provided no cooling potential, and the largest load $CDD_{nas,max}$, which may or may not coincide with $t_{nas,max}$, were also noted. If $t_{nas,max}$ was equal to zero for a particular source in a particular location, then that source offers potential every hour of the year and thermal storage is not required.

The thermal storage capacity, M^* , necessary to serve the load during periods with no ambient source potential was found from the energy balance

$$M^* c_p \Delta T = CDD_{nas}(UA) \quad (5.14)$$

where the left hand term represents the heat in the thermal mass and the right hand term represents the heat gains into the building, c_p is the specific heat of the thermal mass, UA is the building overall loss coefficient, and ΔT is defined by

$$\Delta T = T_{c,hi} - T_{min} \quad (5.15)$$

where T_{min} was somewhat arbitrarily set as the minimum ambient source temperature during the 24-hour period prior to the start of t_{nas} . (This period of time spans one typical diurnal swing in ambient source availability, and may limit the necessary complexity of the storage system in particular, passive storage may be sufficient for short periods. The interval of time over which energy can usefully be stored may depend on a number of factors, including forecasting accuracy and storage losses.) Rearranging Equation 5.14, the normalized thermal capacitance required to meet the cooling load during each period t_{nas} is

$$C^* = \frac{M^* c_p}{UA} = \frac{CDD_{nas}}{\Delta T} \quad (5.16)$$

The largest thermal mass required to meet the load during the period with the greatest ratio of load to ambient source potential is

$$C_{max}^* = \frac{M_{max}^* c_p}{UA} = \left(\frac{CDD_{nas}}{\Delta T} \right)_{max} \quad (5.17)$$

Because all other periods have smaller ratios of load to ambient source potential, M_{max}^* represents the thermal mass required to meet the entire annual cooling load.

For normalized thermal mass $C < C^*$, the load met by the ambient source was assumed to be proportional to C/C^* , which leads to an annual ambient cooling fraction of

$$F_{as} = 1 - \frac{\sum_{n=1}^{365} \left\{ \sum_{m=1}^{24} \left[\left(1 - \frac{C}{C^*} \right)^+ (T_a(m,n) - T_b)^+ \right] \right\}_{nas}}{24CDD} \quad (5.18)$$

where the superscripts + indicate summation only when the quantities in parentheses are positive and the subscript *nas* indicates summation only when no ambient source is available (during periods t_{nas}).

The necessary mass of four different storage materials (water, concrete, and phase change materials eutectic salt ($\text{Na}_2\text{SO}_4 \cdot 10\text{H}_2\text{O}$) and paraffin) was calculated. Effective specific heat for each phase change material was estimated using

$$c_p = \frac{18.3}{T^{*2}} \lambda + \left(1 - \frac{18.3}{T^{*2}} \right) c_{sol} + \frac{18.3}{T^{*2}} c_{liq} \quad (5.19)$$

where T^* is the melting temperature of the medium - set to 18.3 °C (65 °F) for this calculation (Paraffin melting at this temperature is commercially available [Rubitherm, 2013], and sodium sulphate decahydrate can be modified to melt at this temperature by addition of sodium chloride [Sharma et al., 2004]), λ is the heat of fusion, c_{sol} is the specific heat as a solid, and c_{liq} is the specific heat as a liquid [Duffie and Beckman, 2006]. Using a building overall loss coefficient $UA = 0.5 \text{ W/m}^2\text{K}$ that meets the PassivHaus standard in temperate and cooler climates (the PassivHaus maximum design load of 10 W/m^2 [www.passivhaus.org.uk] at a design temperature difference of 20°C or less), the required thickness of thermal storage for each medium is

$$th = \frac{M_{max}^*}{\rho A} \quad (5.20)$$

where A is the floor area and ρ is the density of the respective storage medium. Densities and specific heats for each medium [Duffie and Beckman 2006] are shown in Table 5.2. The density of eutectic salt is lower for liquid than solid state, thus the smaller of these values was used to ensure maximum required storage thickness was accounted for.

Table 5.2. Specific heat values for the thermal storage mediums.

Medium	Density (kg/m ³)	Specific Heat (J/kg*K)
Water	1000	4186
Concrete	2300	750
Eutectic salt	1330	15,709
Paraffin	786	14,311

5.4. Chapter 5 Results

CDD exceeds 900 °F days for the majority of the country, but is greater than approximately 3600 °F days for a few locations in CA, AZ, TX and FL (Figure 5.2). A considerable reduction in annual cooling loads could be obtained by increasing the base temperature from 65°F (Figure 5.2) to 72°F (Figure 5.3), which could be accomplished not only by allowing higher indoor temperatures, but also by reducing indoor heat generation. Only southern CA, AZ, TX and FL have cooling potential from dry-bulb air temperature less than 2500 °F days, while a significant portion of the northern and mountainous regions exceed 10,000 °F days (Figure 5.4). Wet-bulb potential is low along a small portion of the southern tip of TX and the southern part of FL (Figure 5.5). The majority of the rest of the country, including a large portion of the humid southeast, has wet-bulb potential above 5000 °F days. Most of the country has cooling potential from ground temperature exceeding 2500 °F days, but due to ground temperature near or above $T_{c,hi}$, the

southernmost states and hot, desert-like regions of California and Nevada have the least, and some have none at all (Figure 5.6). Nearly the entire country, including most of TX and FL, has potentials for night sky cooling exceeding 5000 °F days, and potentials in approximately two-thirds of the country surpass 10,000 °F days (Figure 5.7).

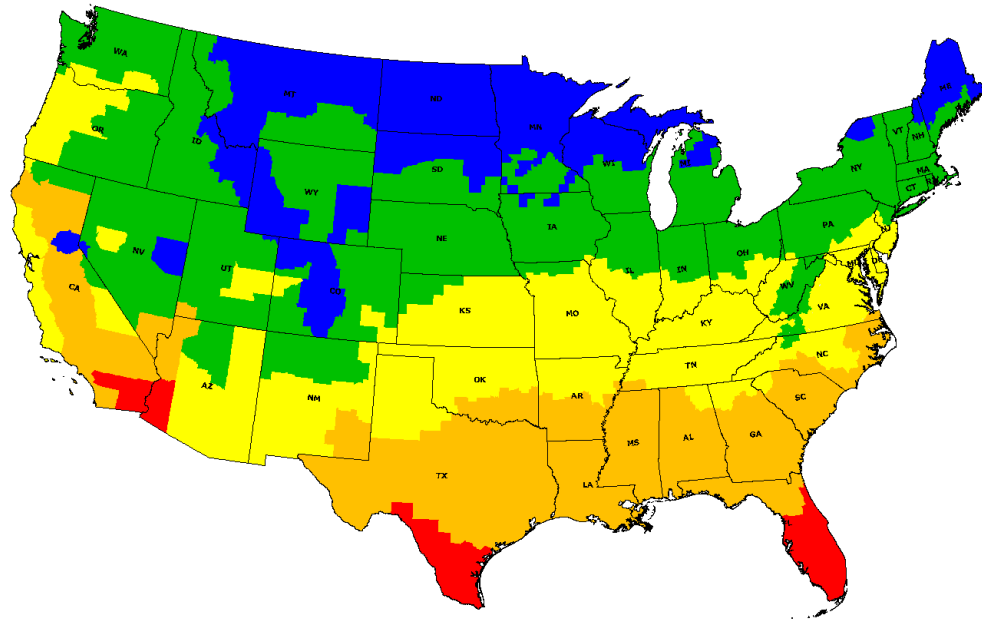


Figure 5.2. Annual cooling load (CDD) for $T_b = 65^\circ F$. The representative annual CDD ranges and their assigned colors are as follows:

- **Blue: 0 – 900 °F days**
- **Green: 901 – 1800 °F days**
- **Yellow: 1801 – 2700 °F days**
- **Orange: 2701 – 3600 °F days**
- **Red: over 3600 °F days**

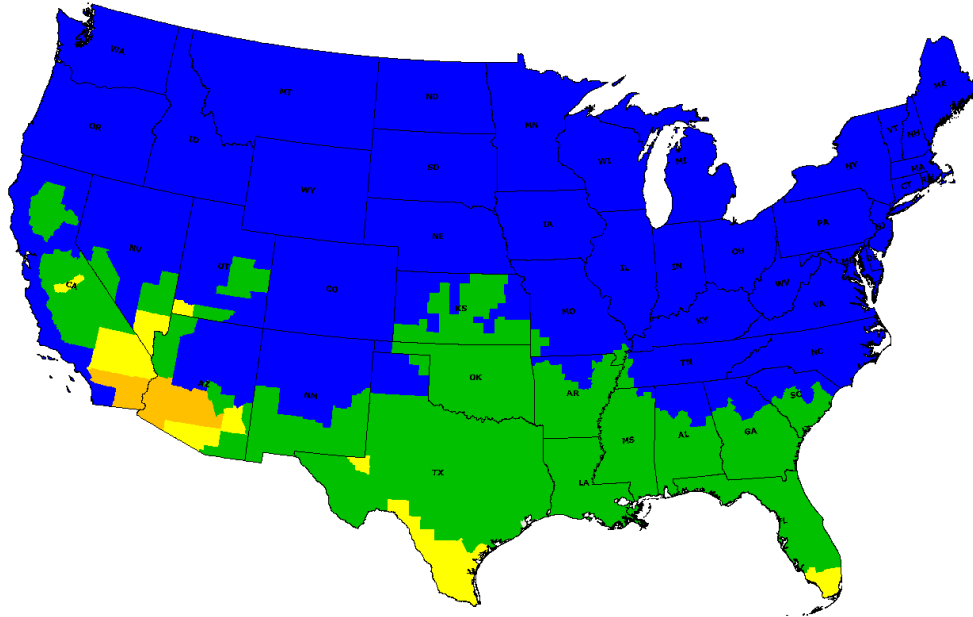


Figure 5.3. Annual cooling load (CDD) for $T_b = 72^\circ\text{F}$. Ranges and shades are the same as that for Figure 5.2.

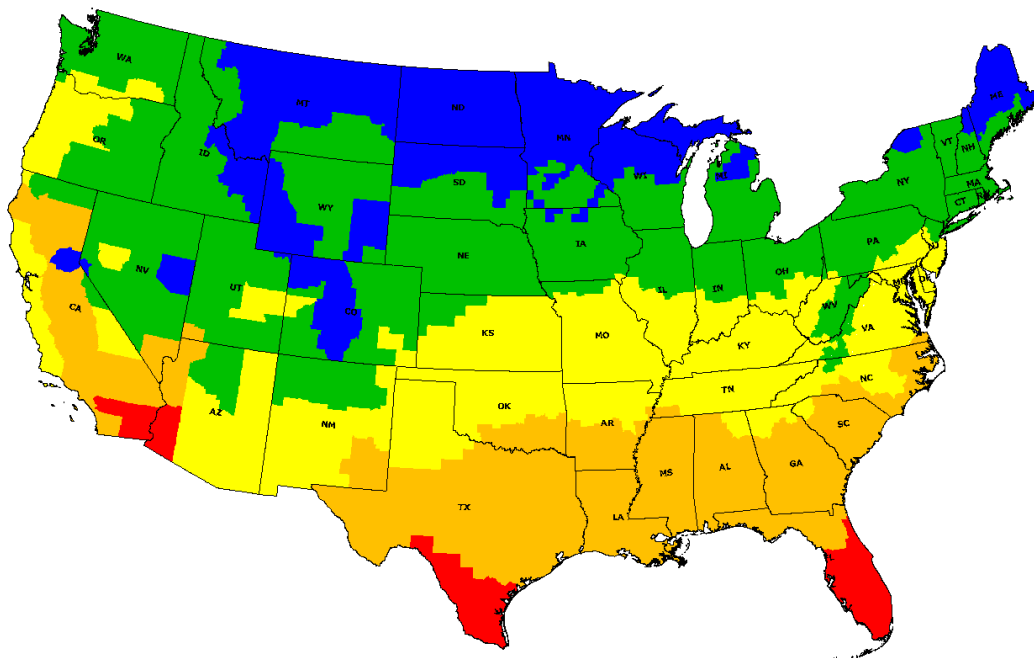


Figure 5.4. Annual dry-bulb cooling capacity for $T_{c,hi} = 72^\circ\text{F}$. The range is broken into 5 increments:

- *Red: 0 – 2500 °F days*
- *Orange: 2501 – 5000 °F days*
- *Yellow: 5001 – 7500 °F days*
- *Green: 7501 – 10,000 °F days*
- *Blue: over 10,000 °F days*

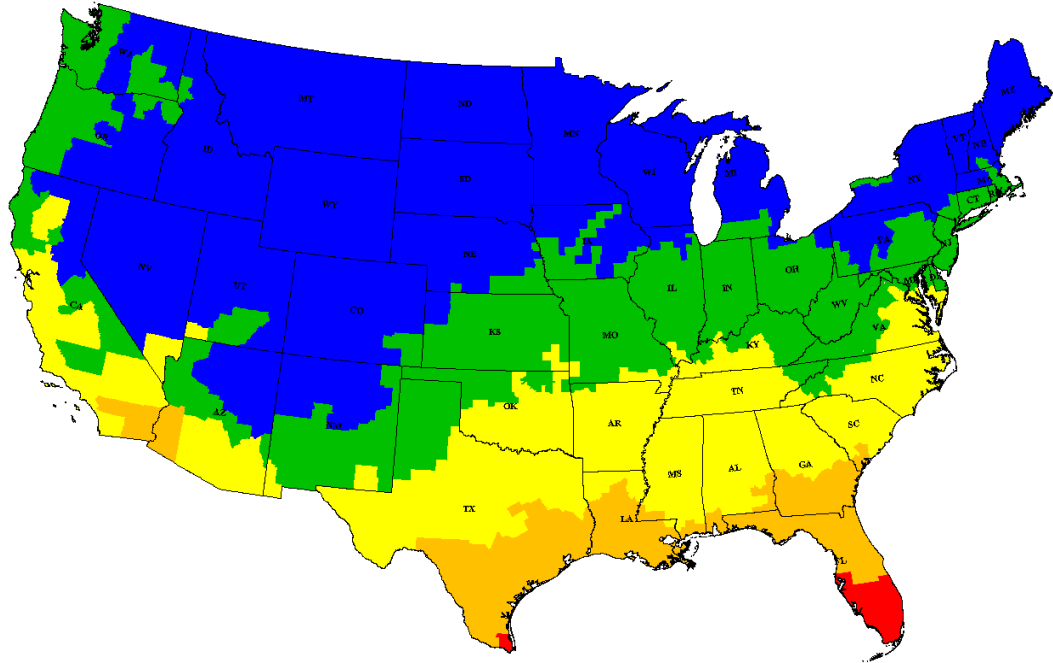


Figure 5.5. Annual wet-bulb cooling capacity for $T_{c,hi} = 72^\circ\text{F}$. The ranges and their assigned colors are the same as Figure 5.4.

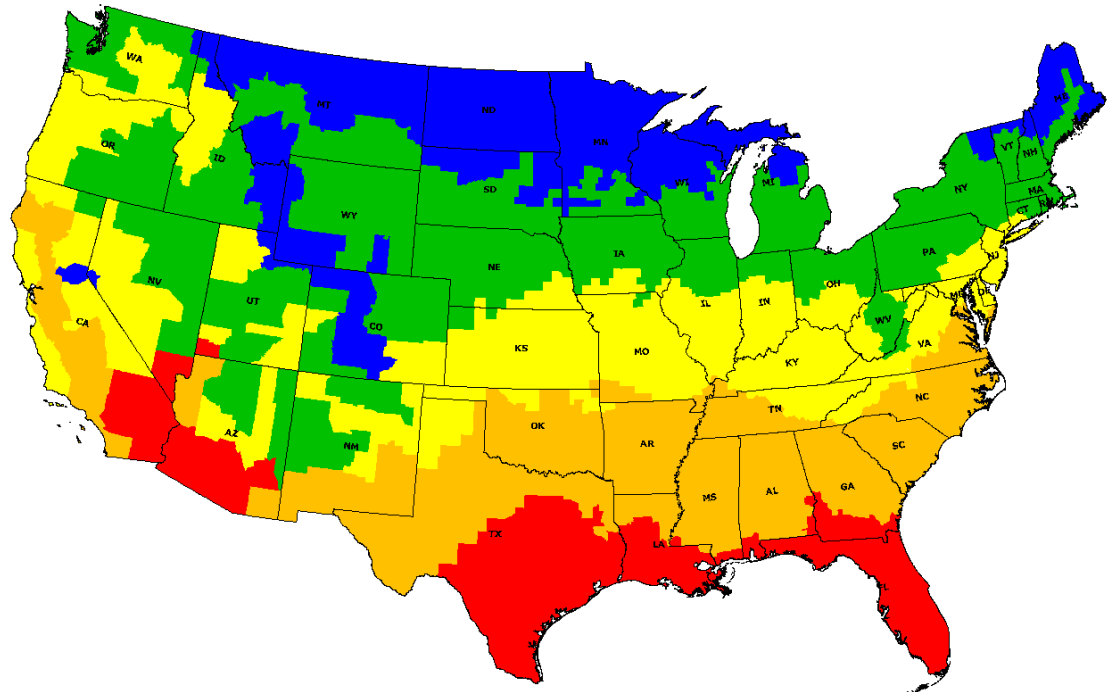


Figure 5.6. Annual ground temperature cooling capacity for $T_{c,hi} = 72^\circ\text{F}$. The ranges and their assigned colors are the same as Figure 5.4.

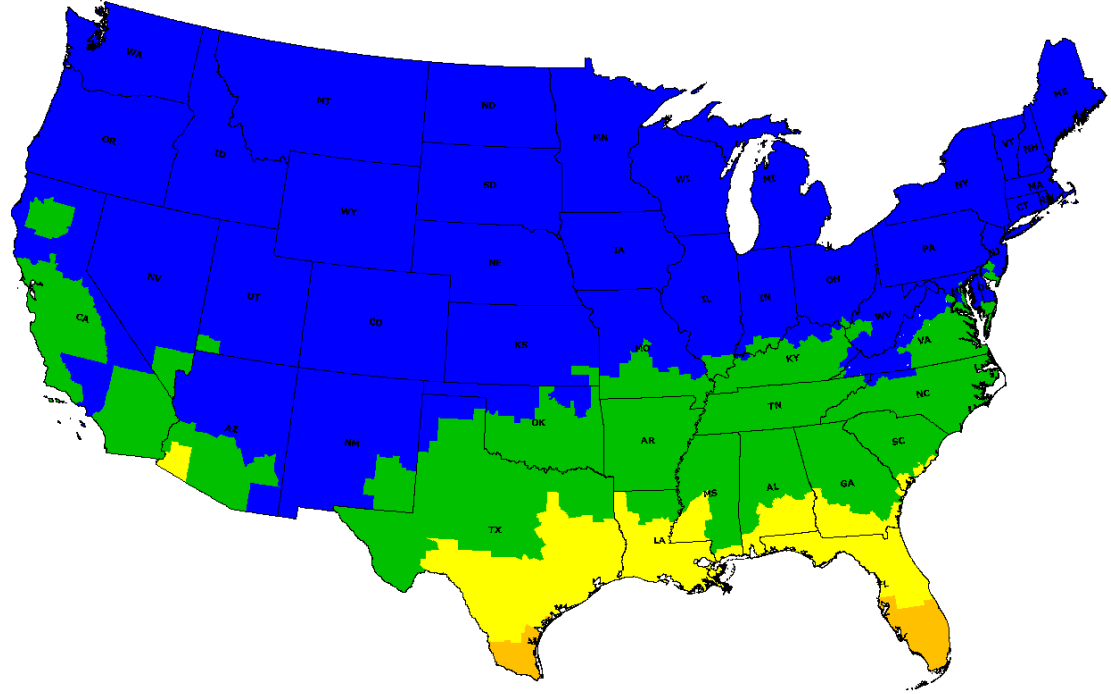


Figure 5.7. Annual sky temperature cooling capacity for $T_{c,hi}=72^{\circ}\text{F}$. The ranges and their assigned colors are the same as Figure 5.4.

A representative comparison of the maximum and average daily cooling potential for dry-bulb, wet-bulb, ground and sky ambient sources in Louisville, KY is shown in Table 5.3. Potential from the sky is largest by both measures, but not overwhelmingly. Maximum and average daily ACDD for ground are equivalent since its temperature is constant.

ALR exceeded one for dry-bulb air and for ground temperature for all locations except Miami, New Orleans and Phoenix (Figure 5.8). Wet-bulb and sky ALR exceeded one for all locations except Miami. The largest ALR for all locations was for sky cooling. Cold and dry Rock Springs had the highest ratio of cooling potential to load for all sources.

Table 5.3. Louisville, KY maximum and average daily cooling potentials for $T_{c,hi} = 72^{\circ}\text{F}$.

Ambient source	Dry-bulb	Wet-bulb	Ground	Sky
Maximum daily ($^{\circ}\text{F days}$)	60.2	62.1	15.5	64.6
Average daily ($^{\circ}\text{F days}$)	17.4	21.2	15.5	25.1

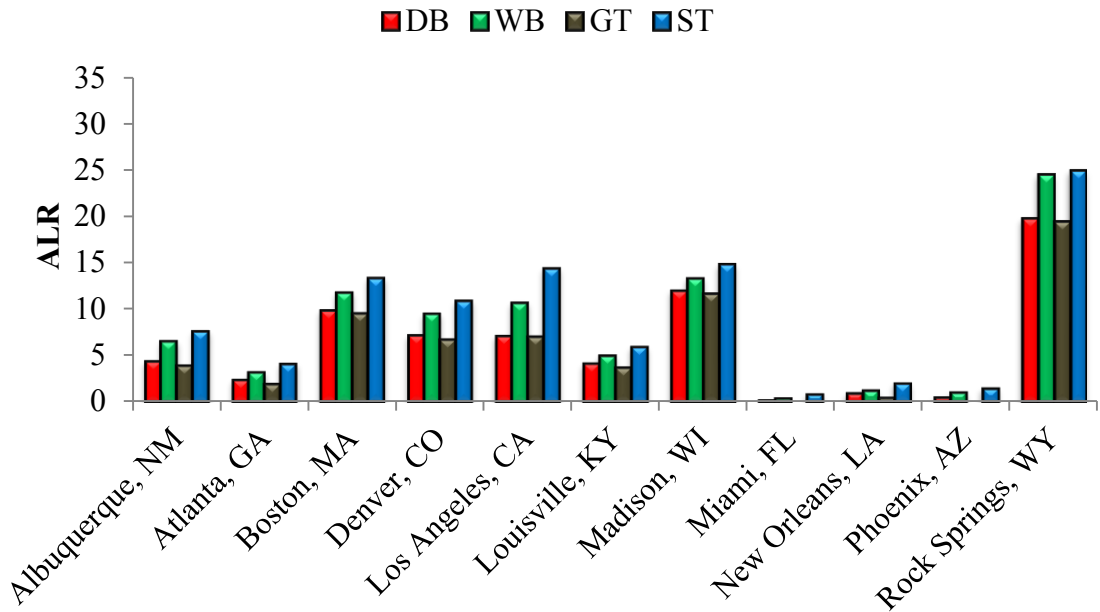


Figure 5.8. Ambient potential to cooling load ratio for dry-bulb (DB), wet-bulb (WB), ground temperature (GT) and sky temperature (ST) ambient sources.

Daily cooling loads and potentials for dry-bulb on days with cooling loads in Denver, CO are shown in Figure 5.9, and the cooling capacity available from the sky on days with cooling loads is shown in Figure 5.10. In these figures, the red bars represent the cooling load for a particular day and blue bars represent cooling potential. The lack of a bar on a particular day indicates that no cooling load exists. Cooling loads occur for 170 days based on hourly temperatures. Eighty of these days have cooling potential from dry-bulb air exceeding the cooling load (Figure 5.9), and 156 days have sky potential that exceeds the cooling load (Figure 5.10).

Annual ambient potential fractions for diurnal storage are shown in Figure 5.11. The lack of a bar for ground temperature in Miami and Phoenix means that ground temperature in this location is above the defined upper comfort limit, thus it offers no cooling potential. $F_{as,1d}$ equaled one for ground temperature for Denver, Los Angeles,

Madison and Rock Springs and for sky temperature for Los Angeles and Rock Springs. $F_{as,1d}$ for ground temperature was above 0.9 for all locations except the southerly locations of Atlanta, Miami, New Orleans and Phoenix. In addition to Los Angeles and Rock Springs, $F_{as,1d}$ for sky temperature exceeded 0.9 for the more moderate and dry climates of Albuquerque and Denver. $F_{as,1d}$ for sky temperature exceeded 0.6 for all locations except the hot climates in Miami, New Orleans and Phoenix, yet sky temperature still provided the greatest $F_{as,1d}$ of all sources in these climates.

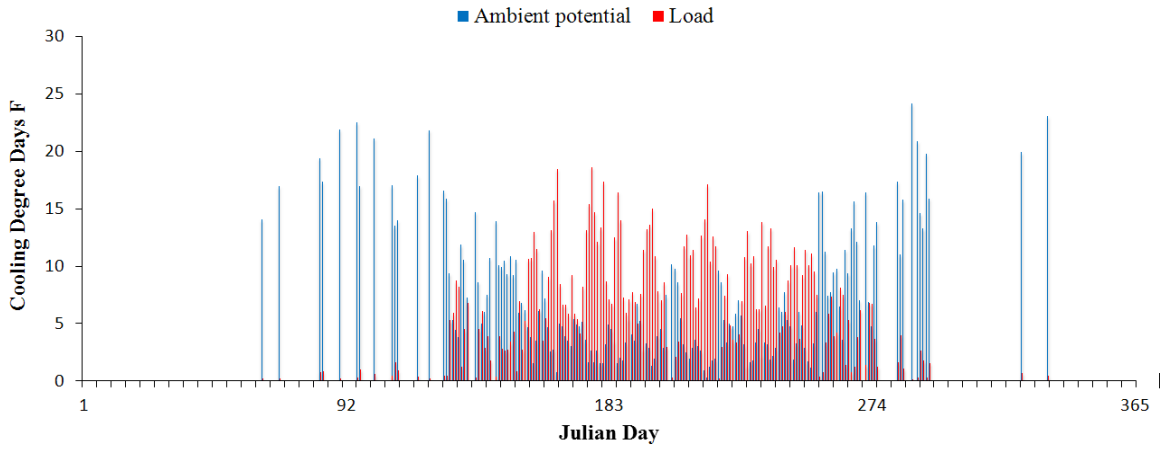


Figure 5.9. Cooling load and cooling capacity (degree days F) from ambient air for Denver, CO.

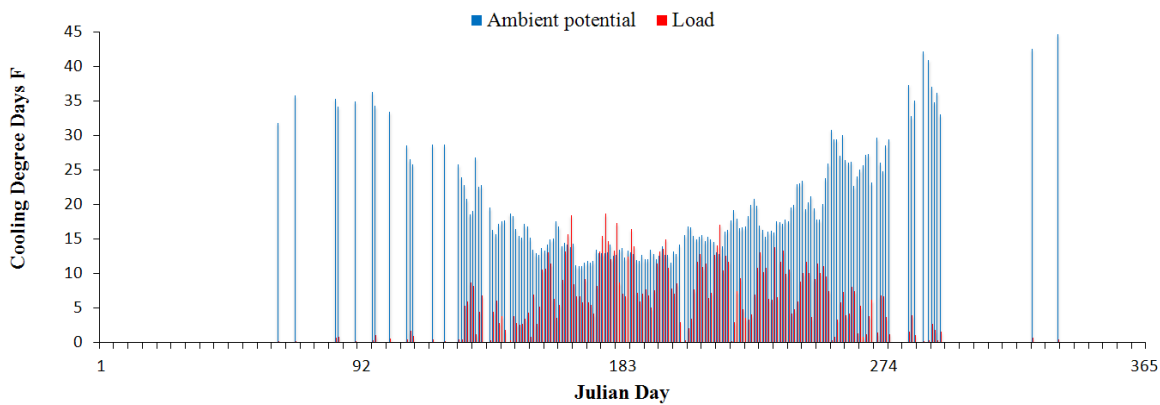


Figure 5.10. Cooling load and cooling capacity (degree days F) from sky for Denver, CO.

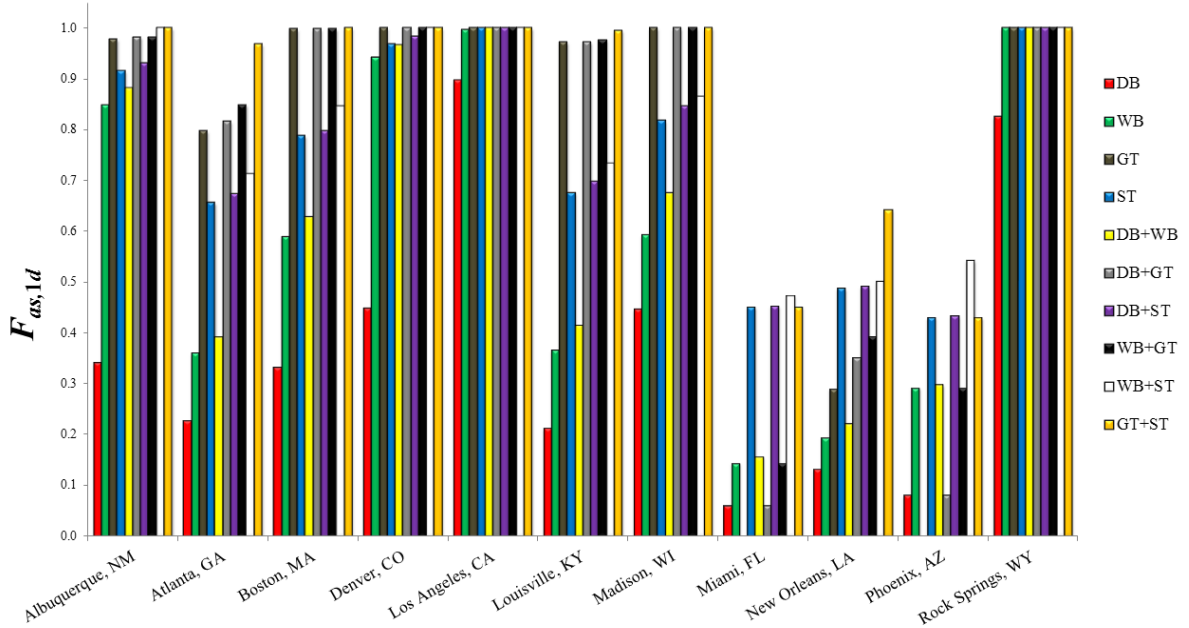


Figure 5.11. Annual ambient potential fraction, $F_{as,1d}$, for all possible combinations of ambient sources for 11 locations.

Storage capacity to building overall loss coefficient ratio, C^*_{max} , is shown in Figure 5.12. Ground temperature is not shown in Figure 5.12; since this source provides potential during every hour of the year (wet-bulb temperature also provided continuous cooling potential in Los Angeles and Rock Springs). Therefore, $C^*_{max} = 0$ and thermal storage is not required. Dry-bulb storage requirements are significantly greater than wet-bulb and sky in all locations except Los Angeles, where all ambient sources provided effective cooling potential. Wet-bulb temperature provided improved potential over dry-bulb temperature in all locations, but large thermal capacitance was still required in Atlanta, New Orleans, Phoenix and Miami. Night sky cooling required the smallest thermal capacitance in all locations with the exceptions of Albuquerque and Denver, where C^*_{max} values for wet-bulb temperature were also small.

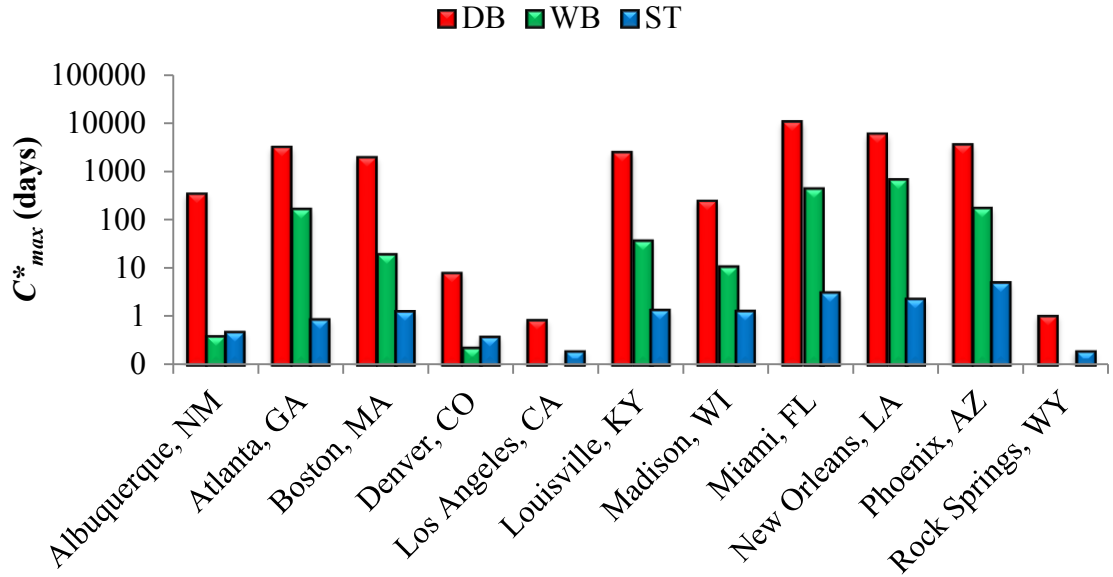


Figure 5.12. Storage capacity to building overall loss coefficient ratio C^* for ambient sources requiring thermal mass for 11 locations.

Values throughout the year for CDD_{nas} and C^* for dry-bulb in Albuquerque and New Orleans are shown in Figures 5.13 and 5.14, respectively. For Albuquerque, dry-bulb $t_{nas,max}$ was equal to 1.67 days (40 hours), and dry-bulb $t_{nas,max}$ for New Orleans was equal to 56.0 days (1345 hours). Spans with no bar signify periods in which there were no cooling loads, or there were cooling loads concurrent with ambient source cooling potential. Spans with durations of 8 hours or less are shorter than the resolution of these figures, thus are not visually apparent, but can be identified by changes in the values of CDD_{nas} and C^* .

Plots of F_{as} versus C/C^*_{max} for Albuquerque only and both New Orleans and Phoenix are shown in Figures 5.15 and 5.16, respectively. C^*_{max} is the maximum calculated value, for all ambient sources, for each respective location.

The required mass and equivalent thickness per square meter of floor area for four different storage materials with $C^* = 1$ day for a building that meets the PassivHaus

standard of approximately $0.5 \text{ W/m}^2\text{K}$ are shown in Figures 5.17 and 5.18. The storage material that required the smallest storage mass and, accordingly, thickness was eutectic salt.

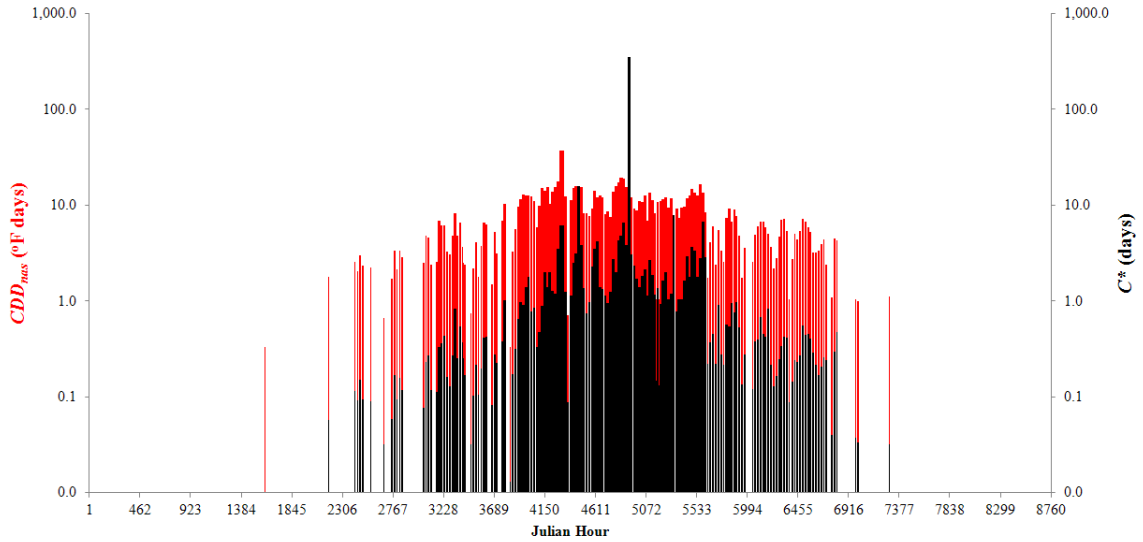


Figure 5.13. Values throughout the year for CDD_{nas} and C^* for dry-bulb in Albuquerque, NM.

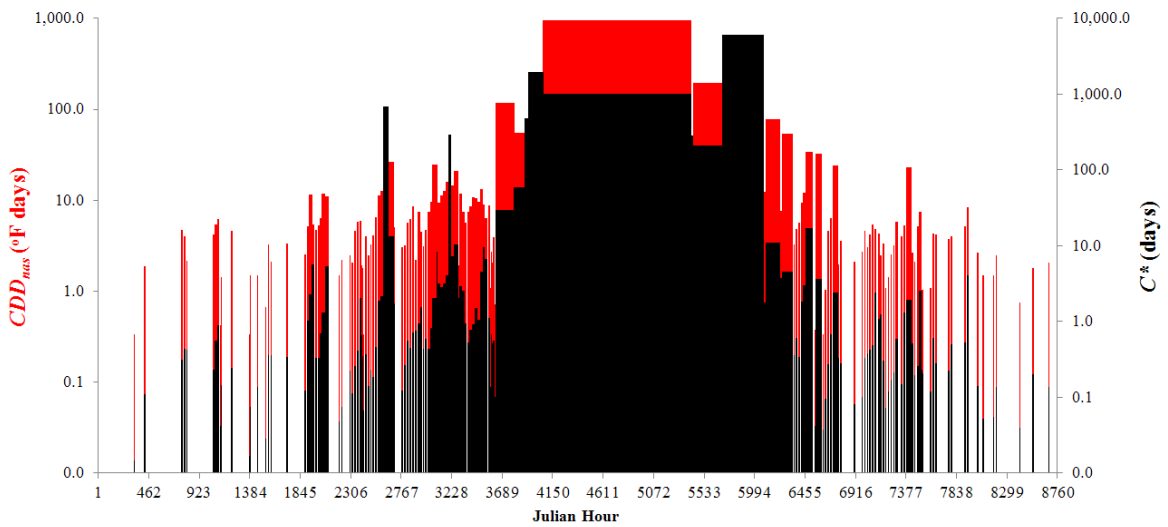


Figure 5.14. Values throughout the year for CDD_{nas} and C^* for dry-bulb in New Orleans, LA.

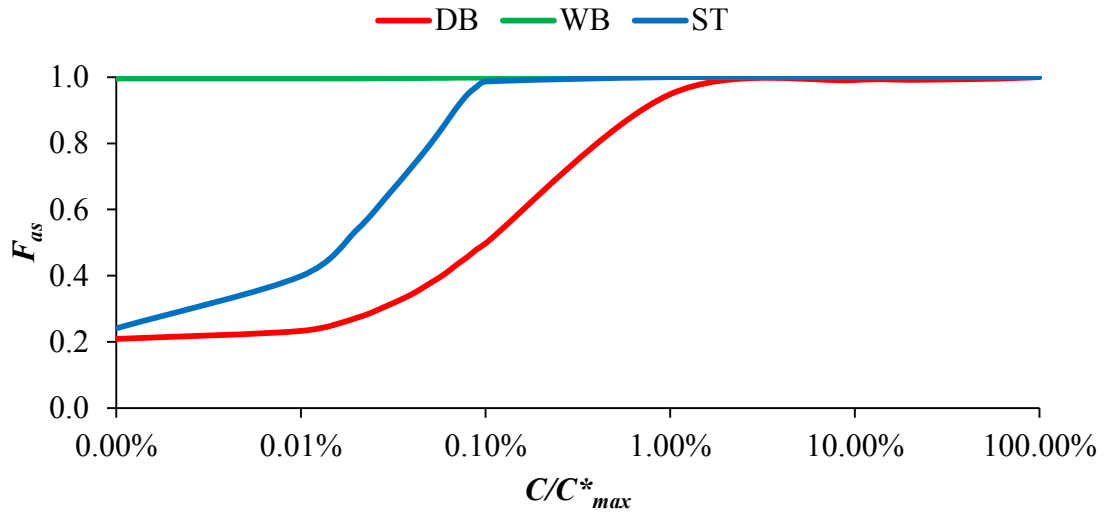


Figure 5.15. F_{as} versus C/C^*_{max} for Albuquerque, NM.

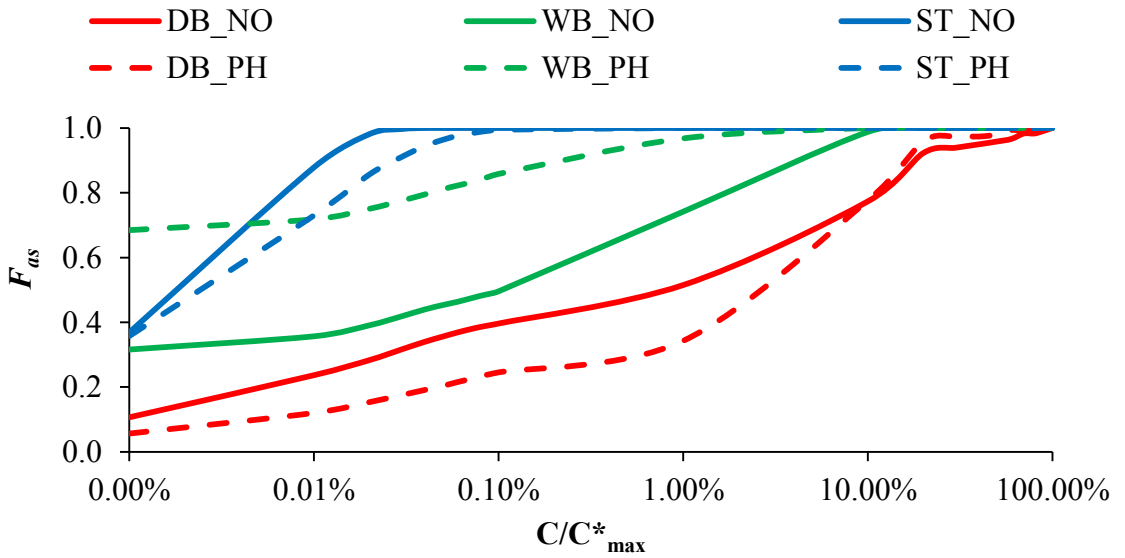


Figure 5.16. F_{as} versus C/C^*_{max} for New Orleans, LA and Phoenix, AZ.

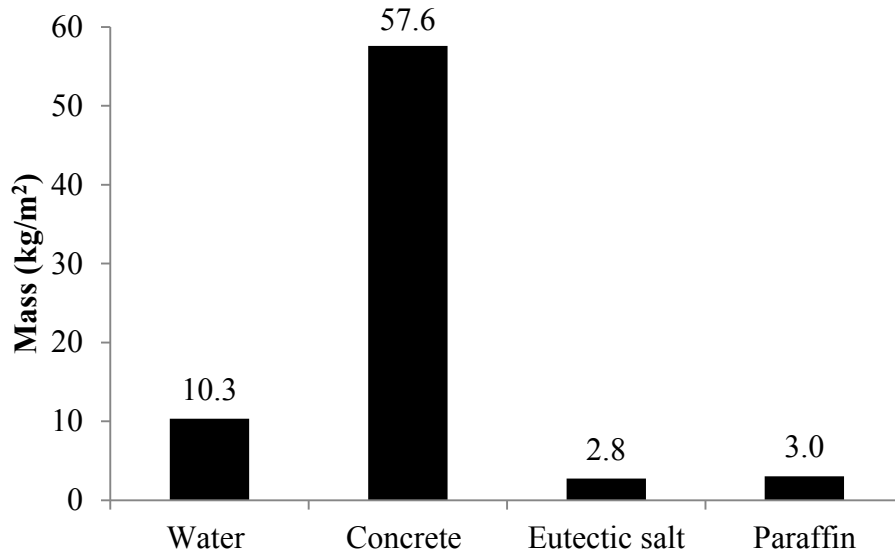


Figure 5.17. Required mass per square meter of floor area and for four different storage materials for a building that meets the PassivHaus standard.

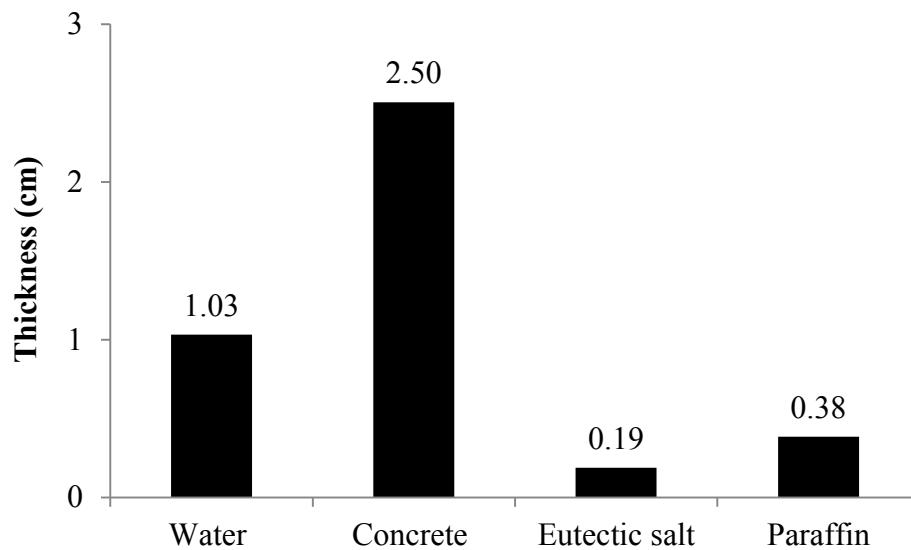


Figure 5.18. Required thickness per square meter of floor area and for four different storage materials for a building that meets the PassivHaus standard.

5.5. Chapter 5 Discussion

T_{ab} offers the least cooling potential among all ambient sources (Figs. 5.4-5.7). T_{wb} cooling potential is significantly higher for the western half of the US, which accounts for typically dryer climates than the eastern half. T_s provides significantly greater cooling

potential over all other ambient sources. As shown in Table 5.3, daily average *ACDD* in Louisville for sky is greater than for ground by a factor of 1.6, dry-bulb by a factor of 1.4, and wet-bulb by a factor of 1.2. In southern cities, such as Miami, New Orleans, and Phoenix, neither seasonal dry-bulb temperatures nor ground temperatures offer much cooling potential relative to the upper comfort limit; in fact, there is no ground temperature cooling potential in Miami nor Phoenix and small potential in New Orleans ($ALR = 0.41$, Figure 5.8). It is important to note that $ALR = 1$ is not a threshold for serving the annual cooling load. Rather, *ALR* simply compares the temperature difference between the source and the upper comfort limit to the cooling load. The thermal mass required to meet the entire cooling load tends to be inversely proportional to *ALR*. With large enough thermal mass, the annual load could be met by an arbitrarily small *ALR*.

In Denver, as in many locations, a particular day may exhibit both cooling loads and cooling potentials (Figs. 5.9 and 5.10). When ambient temperature is between the room comfort temperature limits, cooling from ambient air can be immediately applied. However, for ambient temperature below this range, cooling is not immediately needed, but thermal storage can be used to save the coolness until a load occurs. When cooling potential occurs on the same day, the load might be served with one night's worth of storage, some of which can be met with the relatively modest thermal mass in conventional homes.

Eight of the eleven locations had at least one ambient source or combination of sources that attained $F_{as,1d} = 0.9$ or greater, with the exceptions being Miami, New Orleans and Phoenix (Figure 5.11). For these locations, the highest $F_{as,1d}$ was still greater than 0.47. Maximum $F_{as,1d}$ values greater than 0.47 for very hot and humid Miami were

obtained with wet-bulb and sky temperatures, 0.64 for hot and humid New Orleans with ground and sky temperatures, and 0.54 for hot and dry Phoenix with wet-bulb and sky temperatures. For those locations and ambient sources for which $F_{as,ld} < 1$, the fraction of the cooling load served might be increased with greater thermal storage capacity. Also noteworthy is that, in four locations, only one source was necessary to achieve $F_{as,ld} = 1$ (three other locations also nearly met this limit: since the ground temperature sources in Albuquerque, Boston and Louisville provided $F_{as,ld} = 0.978$, 0.998 and 0.972 , respectively) and no more than two sources were necessary to achieve the same level of cooling that could be gained from a combination of all ambient sources. These results can be used to guide the selection of the best sources for particular climates, eliminating the need to utilize three or more sources and the additional costs associated with doing so.

Dry-bulb temperature was effective as a cooling source in locations, such as Denver, Los Angeles and Rock Springs, that consistently experienced nighttime temperatures significantly below $T_{c,hi}$ (Figure 5.12). In contrast, long spans of time without dry-bulb cooling capacity produced large C^*_{max} in Atlanta, Boston, Louisville, Miami, New Orleans and Phoenix. Wet bulb allowed the least thermal storage in dry climates, while required thermal capacitance was lowest for night sky cooling in humid climates.

Time intervals t_{nas} for dry-bulb in Albuquerque (Figure 5.13) were short, since most nights, even during the summer, exhibited dry-bulb temperatures below $T_{c,hi}$. t_{nas} for sky temperature in all locations were similarly short since cooling potential is available every night of the year. Frequent availability of ambient cooling reduced CDD_{nas} and C^* for these sources. On the other hand, the onset of summer months in hot and humid New Orleans results in long periods during which T_{db} never drops below $T_{c,hi}$, resulting in long

t_{nas} and high CDD_{nas} and C^* (Figure 5.14). Figures 5.13 and 5.14 also highlight scenarios in which $CDD_{nas,max}$ does not occur at the same time as C^*_{max} , where the maximum required thermal capacitance in both locations occurs several days after the occurrence of $CDD_{nas,max}$. Large C^* occurs when T_{min} is only slightly smaller than $T_{c,hi}$, preventing storage from becoming significantly cooled, and requiring a much greater capacitance to meet the load. Situations as such occur most often for dry-bulb in warm and hot locations, on fewer occasions for wet-bulb, and do not occur for night sky cooling, since when this source is available, sky temperatures tend to be low. For locations where this occurs, remaining values of C^* are so much smaller than C^*_{max} , that large values of F_{as} can be obtained at very small fractions of C^*_{max} . In Figure 5.15, F_{as} for dry-bulb is equal to 0.95 using only 1% of C^*_{max} , and is equal to 99% using 10% of C^*_{max} .

The maximum values of C^*_{max} in Figs. 5.15 and 5.16 were for dry-bulb, which was also the case for all other locations. In Albuquerque, F_{as} for wet-bulb is already equal to 0.996 without any thermal capacitance because there was only a total of 7 hours of no wet-bulb cooling potential during the entire year (Figure 5.14). In hot climates, wet-bulb requires considerably less thermal capacitance in dry (Phoenix) versus humid conditions (New Orleans, Figure 5.15). For each climate zone, the wet-bulb thermal capacitance required to serve the annual cooling load was an average of 94.3% less in dry climates versus humid ones. A mere 0.1% of C^*_{max} is required to obtain F_{as} equal to 1.0 for sky in both locations, and no more than 10% of C^*_{max} is required to obtain the same results in all locations, with the exceptions being Los Angeles and Rock Springs. In these two locations, the cooling potentials of all ambient sources are so large that C^*_{max} for dry-bulb is not much larger than C^*_{max} for sky.

For Albuquerque, utilizing $C/C^*_{max} = 0.1$ to serve 99% of the annual cooling load would require thermal mass thickness $th = 36.4$ cm using water as thermal storage. Using paraffin instead reduces the required th by more than 60% to 13.55 cm, eutectic salt would require the smallest th at 6.64 cm, and even concrete, with a considerable smaller specific heat than the other three storage mediums, would require less than a meter at 88.34 cm. The ambient source and storage medium combination of sky temperature and eutectic salt yielded the smallest required value of th in all locations at all C/C^*_{max} , with the exception of the cooler and dry climates of Albuquerque, Denver and Rock Springs, in which the combination of wet-bulb using eutectic salt required similar th . To obtain $F_{as} = 1$ using sky temperature in any location, the maximum required th using each of the four storage mediums investigated was 12.56 cm (in Phoenix using concrete). For Denver, Los Angeles and Rock Springs, the required th to obtain $F_{as} = 1$ using sky temperature for all storage mediums, including concrete, fell in the range of mm's. For all other locations except Miami, New Orleans and Phoenix, the required th using sky temperature for all storage mediums was less than 5 cm.

5.6. Chapter 5 Conclusions

Ambient cooling potential to cooling load ratio, ALR , provides a measure of the potential to serve annual cooling loads, without identifying the necessary thermal storage capacity. The primary utility of ALR may be in identifying the most promising ambient cooling sources in each climate. Annual ambient cooling potential fraction, $F_{as,1d}$, incorporates a rudimentary element of thermal storage, and estimates the potential of ambient sources with diurnal thermal storage to serve cooling loads. $F_{as,1d}$ is an indicator of the portion of the cooling load that might be served with each ambient source, but

actual load fractions may strongly depend on system design. For climates in which the thermal capacitance required for a particular ambient source to serve the entire annual load seems unreasonable, much smaller fractions of C^*_{max} often served more than 90% of the annual cooling load.

Dry-bulb cooling was marginally effective for locations that typically experience large diurnal temperature swings, and wet-bulb cooling was a suitable option for the dry climates across a large portion of the western US. Ground cooling was suitable for any location where the average annual ambient temperature was less than the upper comfort limit, and ground temperature provided a superior $F_{as,1d}$ over all other sources in these locations. Ground temperature also provided the advantage of continuous hourly potential throughout the year.

Among the ambient sources investigated in this study, sky cooling seemed the most promising. In all climates, sky temperature provided significant cooling potential every night, and had the largest ALR and smallest C^*_{max} . Sky temperature was the only ambient source that provided cooling potential in every climate, and was the only available source in the southernmost climates. Furthermore, a nano-structured radiator has recently been designed with very high solar reflectance that is theoretically capable of achieving cooling to the sky during daytime [Rephaeli, et al. 2013]. If real surfaces can be developed with this level of performance, then the potential of sky cooling could be approximately twice that assumed in this study.

While this study shows that ground and sky temperature sources have the greatest cooling potential in the majority of locations, actual thermal performance depends on details of system design and operation that were not part of this study. Indeed, a number

of specific ambient cooling systems have been evaluated in more detail, both numerically and experimentally [Cook, 2000; Santamouris, 2007]. The value of this work lies rather in identifying candidate sources with the greatest potential for natural cooling in a range of locations across the US, while achieving the cooling potentials estimated by these methods remains an engineering challenge. In addition, economic performance was not evaluated, but is an important factor in determining the optimal system. Considering the prospect that ambient sources could entirely eliminate fossil fuel combustion and carbon emissions for space cooling in many climates, further research and development of such systems seems warranted.

CONCLUSIONS

The heat pipe assisted solar space heating system delivers significant amounts of heat to thermal storage and the room during periods of good insolation. Small thermal losses (to ambient) associated with these systems allow thermal gains to the room to remain positive, even during extended periods of little to no insolation, and provides thermal storage temperatures that are quickly restored to high levels upon the next onset of significant insolation. The previous system provided higher thermal performance than conventional direct gain, Trombe wall and water wall systems. The new model of the heat pipe assisted solar wall exhibited even greater performance. Further, by utilizing valve and/or cover control mechanisms and an ambient-based control strategy for reducing unwanted thermal gains to the room during the cooling season, low load to collector ratio (LCR) values become practical, allowing the system to serve a large fraction of building space heating loads in a wide range of climates across the U.S. To address space cooling needs, cooling potential of several ambient sources was evaluated. Sky temperature offers greater space cooling potential over dry-bulb, wet-bulb, and ground temperatures in all climates. Also, sky temperature utilized in conjunction with reasonable thermal storage, is the only 'universal' ambient source that has the potential to serve the entire annual space cooling load for buildings in *all* U.S. locations. Further research on night sky radiators and combined heating and cooling systems is warranted.

REFERENCES

- Agas G, and Matsaggos T. 1994. "On the Use of Atmospheric Heat Sinks for Heat Dissipation." *Energy and Buildings* 17 (4): 321-29.
- Al-Nimr MA, Kodah Z., and Nassar B. 1998. "A Theoretical and Experimental Investigation of a Radiative Cooling System." *Solar Energy* 63 (6): 367-73.
- Albanese MV, Robinson BS, Brehob EG and Sharp MK. 2012. "Simulated and Experimental Performance of a Heat Pipe Assisted Solar Wall." *Solar Energy*, 86:5:1552-62.
- American Society for Testing Materials (ASTM) International *Standard E779: Standard Test Method for Determining Air Leakage Rate for Fan Pressurization*. 2010.
- ASHRAE Std 55-2004. 2004. *Thermal Environmental Conditions for Human Occupancy*. Atlanta, GA: American Society of Heating, Refrigeration and Air Conditioning Engineers.
- Athienitis AK, and Ramadan H. 1999. "Numerical Model of a Building with Transparent Insulation." *Solar Energy* , 67 (1-3), 101-09.
- Balcomb JD. 2008. *Passive Solar Buildings (Solar Heat Technologies)*. Cambridge, MA: MIT Press.
- Bataineh KM, and Fayez N. 2011. "Analysis of thermal performance of building attached sunspace." *Energy and Buildings* 43:8:1863-68.
- Catalanotti S, Cuomo V, Piro G, Ruggi D, Silvestrini V, & Troise GR. 1975. "The Radiative Cooling of Selective Surfaces." *Solar Energy* 17 (2): 83-89.
- Chmielewski NE. 2009. "Design, construction, and experimentation of a heat pipe augmented solar wall." *MS thesis*, Department of Mechanical Engineering, University of Louisville.
- Cook J. ed. 2000. *Passive Cooling*. Cambridge, MA: MIT Press.

- Corliss JM. 1979. "Evaluation of Heat Pipe Application for Passive Solar Systems." *DOE Report*, Dept. of Energy, Washington, D.C.
- Dahl CA, and McDonald L. 1998. "Forecasting Energy Demand in the Developing World." *Energy Sources* , 20, 875-89.
- De Paepea M, and Janssens A. 2003. "Thermo-hydraulic Design of Earth-Air Heat Exchangers." *Energy and Buildings* 35 (4): 389-97.
- DOE. 2010. "Guide to Determining Climate Regions by County." US Department of Energy: Energy Efficiency and Renewable Energy. Accessed February 21, 2013. http://apps1.eere.energy.gov/buildings/publications/pdfs/building_america/ba_climateguide_7_1.pdf
- Duffie JA, and Beckman WA. *Solar Engineering of Thermal Processes* (3rd ed.). Hoboken, NJ: Wiley, 2006.
- Dunn PD, and Reay DA. 1994. *Heat Pipes*. Oxford: Pergamon Press.
- EIA (Energy Information Administration) 2011. "Annual Energy Review 2011". Accessed February 15, 2014. <http://www.eia.gov/totalenergy/data/annual/pdf/aer.pdf>
- Erell E, and Etzion Y. 1996. "Heating Experiments with a Radiative Cooling System." *Building and Environment* 31 (6): 509-17.
- Florides GA, and Kalogirou SA. 2004. "Measurements of Ground Temperatures at Various Depths." *3rd International Conference on Sustainable Energy Technologies*. Nottingham, UK.
- Gan G. 1998. "Parametric study of Trombe walls for passive cooling of buildings." *Energy and Buildings* 27:1:37-43.
- Ghrab-Morcos N, Bouden C, and Franchisseur R. 1993. "Overheating caused by passive solar elements in Tunis. Effectiveness of some ways to prevent it." *Renewable Energy* 3:6-7:801-11.
- Hegerl GC, Zwiers FW, Braconnot P, Gillett NP, Luo Y, Marengo Orsini JA. 2007. *Climate Change 2007: The Physical Science Basis. Contribution of Working Group I to the Fourth Assessment Report of the Intergovernmental Panel on Climate Change.* (S. Solomon, D. Qin, M. Manning, Z. Chen, K. A. Marquis, M. Tignor, et al., Eds.) *Understanding and Attributing Climate Change* .
- Incropera FP, and DeWitt DP. *Introduction to Heat Transfer, 6th ed.* Hobokenm NJ: Wiley, 2011.
- Jensen ME, Burman RD, and Allen RG. 1990. *ASCE Manual No. 70*: 176-77.

- Kimball BA. 1984. "Cooling Performance and Efficiency of Night Sky Radiators." *Solar Energy* 34 (1): 19-33.
- Kummert M., Andre P., and Nicolas J. 2000 "Optimal Heating Control in a Passive Solar Commercial Building." *Solar Energy* , 69 (6), 103-16.
- Kusuda T. 1965. "Earth Temperature and Thermal Diffusivity at Selected Stations in the United States." *ASHRAE Transactions*: 71.
- Mihalakakou G, Santamouris M, and Asimakopoulos D. 1994. "Modeling the Thermal Performance of Earth-to-Air Heat Exchangers." *Solar Energy* 53 (3): 301-05.
- Mihalakakou G, Santamouris M, Asimakopoulos D, and Tselepidaki I. 1995. "Parametric Prediction of the Buried Pipes Cooling Potential for Passive Cooling Applications." *Solar Energy* 55 (3): 163-73.
- Mihalakakou G. 2002. "On the use of sunspace for space heating/cooling in Europe." *Renewable Energy* 26:3:415-429.
- Nicol JF, and Humphreys MA. 2002. "Adaptive Thermal Comfort and Sustainable Thermal Standards for Buildings." *Energy and Buildings* 34 (6): 563-572.
- NOAA National Climatic Data Center. 2013. "Heating and Cooling Degree Data." www.ncdc.noaa.gov/oa/document library/hcs/hcs.html.
- Raicu A, Wilson HR, Nitz P, Platzer W, Wittwer V, and Jahns E. 2002. "Facade Systems with Variable Solar Control Using Thermotropic Polymer Blends." *Solar energy* , 72 (1), 31-42.
- Rephaeli E, Raman A, and Fan S. 2013. "Ultrabroadband Photonic Structures To Achieve High-Performance Daytime Radiative Cooling." *NanoLetters* [dx.doi.org/10.1021/nl4004283](https://doi.org/10.1021/nl4004283).
- Ripple D, Burns GW, & Scroger MG. 1994. "Assessment of uncertainties of thermocouple calibrations at NIST." *NISTIR 5340* (Gaithersburg, Maryland, National Institute of Standards and Technology). 34p.
- Robinson BS, Chmielewski NE, Knox Kelecy A, Brehob EG, Sharp MK. 2013 "Heating season performance of a full-scale heat pipe assisted solar wall." *Solar Energy* 87:76–83.
- Robinson BS, Dorwart J, and Sharp MK. 2013. "U.S. Space Cooling Potentials for Ambient Sources with Thermal Energy Storage." *J Ambient Energy* online Dec 2013, DOI:10.1080/01430750.2013. 864585

- Robinson BS, and Sharp MK. "Heating Season Performance Improvements for a Solar Heat Pipe System." *Solar Energy* (submitted 2014)
- Robinson BS, and Sharp MK. "Reducing Unwanted Gains during the Cooling Season for a Solar Heat Pipe System." *Solar Energy* (submitted 2014)
- Rubitherm. 2013. Accessed November 2013. http://www.rubitherm.com/english/download/phase_change_materials.pdf.
- Santamouris M, ed. 2007. *Advances in Passive Cooling*. London: Earthscan.
- Santamouris M, Mihalakakou G, and Asimakopoulos DN. 1997. "On the Coupling of Thermostatically Controlled Buildings with Ground and Night Ventilation Passive Dissipation Techniques." *Solar Energy* 60 (3-4): 191-97.
- Sharma SD, Kitano H, and Sagara K. 2004. "Phase Change Materials for Low Temperature Solar Thermal Applications." *Research Reports of the Faculty of Engineering, MIE University* 29: 31-64.
- SRCC, 2012. Solar Rating and Certification Corporation. <<http://www.solar-rating.org/ratings/index.html>. (last accessed 04/05/2014).
- Susheela N, and Sharp, MK. 2001. "A heat pipe augmented passive solar system for heating of buildings." *J Energy Eng* 127:1:18-36.
- Tester JW, et al. *Sustainable Energy: Choosing Among Options*. Cambridge, MA: MIT Press. 2005.
- Trenberth KE, Jones PD, Ambenje P, Bojariu R, Easterling D., and Tank AK. 2007. *Climate Change 2007: The Physical Science Basis. Contribution of Working Group I to the 4th Assessment Report of the Intergovernmental Panel on Climate Change*. (S. Solomon, D. Qin, M. Manning, Z. Chen, K. A. Marquis, M. Tignor, et al., Eds.) *Observations: Surface and Atmospheric Climate Change* .
- Vanek FM, and Albright LD. *Energy Systems Engineering Evaluation & Implementation*. New York: McGraw-Hill. 2008.
- Wilcox S, and Marion W. 2008. "Users Manual for TMY3 Data Sets." Technical Report NREL/TP-581-43156, revised May 2008.
- Zaheer-Uddin, M. 1989. "Identifying the Domain of Overheating on the Energy Performance Curves of a Passive Solar House." *Energy* , 17 (12), 879-88.
- Zittel W, and Schindler J. 2007. *Crude Oil: The Supply Outlook*. Report to the Energy Watch Group, EWG-Series No. 3.

APPENDICES

Supplementary Analysis of Matching Simulations with Experimental Results for the New Heat Pipe System

Figure A.1 shows simulated and experimental evaporator, tank and room temperatures for January 19 and 20 using the modified simulation parameters specified in Chapter 3. Simulated and experimental evaporator temperatures are analogous to previous results (Figure 3.17), in which experimental temperatures are higher only during peak insolation due to direct evaporator exposure to radiation. The average temperature difference between simulated and experimental room temperatures is 0.22 K. The temperature difference between the tanks slightly exceeds the established threshold of 0.50 K, with an average of 0.53 K. Nevertheless, the close proximity of these results between simulated and experimental temperatures using a model comparison with two days that were not used in “tuning” the model further strengthens the results and the veracity of the modeling work discussed in Chapter 3.

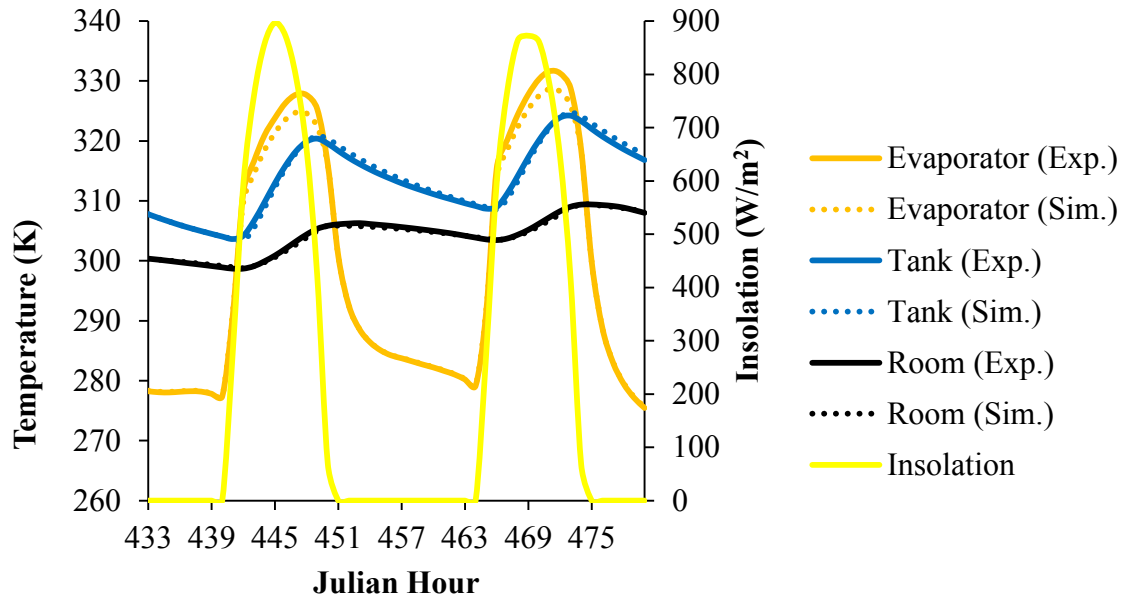


Figure A.1. Simulated and experimental evaporator, tank and room temperatures, for January 19 & 20, after matching.

Nomenclature for Chapter 2: “Heating Season Performance of a Full-Scale Heat Pipe Assisted Solar Wall”

Variables

a	protrusion distance for the horizontal overhang on the building [0.71 m]	\dot{Q}_{sr}	rate of energy (power) transferred from the system thermal mass storage (water) to the room [W]
A_c	prototype collector area [2.41 m ²]	\dot{Q}_s	rate of increase of energy (power) gained by the system thermal mass storage (water) over a one-hour interval [W]
A_s	total heat transfer surface area of the storage tank walls [m ²]	\dot{Q}_u	useful thermal gains for the system; transferred from the heat pipes to the thermal storage and room [W]
b	distance between prototype collector and horizontal overhang on the building [0.77 m]	R_{cond}	conductive resistance through the storage tank wall [K/W]
c_p	specific heat for water used for thermal storage [4186 J/kg·K]	$R_{r,conv}$	convective resistance between the outside of the tank wall and the room air [K/W]
g	acceleration due to gravity [9.81 m/s ²]	R_{rad}	radiative resistance between the outside of the tank wall and the room envelope [K/W]
h	height of the prototype collector [2.02 m]	$R_{s,conv}$	convective resistance between storage water and the inside tank wall [K/W]
h_{rad}	heat transfer coefficient for radiation between the storage tank wall and room envelope [W/m ² K]	R_{sr}	total thermal resistance from the thermal storage to room air [K/W]
$h_{s/r}$	convection coefficient for water (h_s) or room air (h_r), respectively [W/m ² K]	$Ra_{s/r}$	Rayleigh number for water (Ra_s) or air (Ra_r)
$k_{s/r}$	thermal conductivity for water (k_s) or room air (k_r), respectively [W/m·K]	S	insolation received by the prototype collector [W/m ²]
k_w	thermal conductivity of the storage tank wall [0.5 W/m·K]	$S_{diffuse}$	measured shaded insolation on the prototype collector [W/m ²]
L	storage tank wall height [1.52 m]	S_{total}	measured unshaded insolation on the prototype collector [W/m ²]
M	mass of the water in the thermal storage tanks [kg]		
$Nu_{s/r}$	Nusselt number for water (Nu_s) or room air (Nu_r), respectively		
$Pr_{s/r}$	Prandtl number for water (Pr_s) or room air (Pr_r), respectively		

t_w	storage tank wall thickness [3.18 mm]	σ	Stefan-Boltzmann constant [5.67x10 ⁻⁸ W/m ² K ⁴]
T_a	ambient temperature [°C, K]	ϕ	latitude (38.3° in Louisville)
T_r	hourly average temperature of the room [°C, K]	ω	solar hour angle
T_s	hourly average temperature of the storage tank water [°C, K]		
T_w	storage tank wall temperature [°C, K]		
UA	building overall loss coefficient [W/K]		
V	volume of water in the storage tank(s) [m ³]		
x	fraction of shading on the prototype collector		
α	thermal diffusivity [m ² /s]		
β	volumetric thermal expansion coefficient [K ⁻¹]		
δ	solar declination angle		
ε	radiative emissivity of the storage tank wall [0.95]		
ΔT_s	storage water temperature change over a one-hour interval [°C, K]		
ΔT_{sw}	temperature difference between storage water and tank wall [°C, K]		
ΔT_{wr}	temperature difference between tank wall and room air [°C, K]		
Δt	time interval [one hour]		
η	thermal efficiency for the full-scale prototype of the heat pipe solar system		
θ_z	solar zenith angle		
μ	absolute viscosity [Pa*s]; uncertainty for error propagation		
ν	kinematic viscosity [m ² /s]		
ρ	density [kg/m ³]		

Nomenclature for Chapter 3: “Heating Season Performance Improvements for a Solar Heat Pipe System”

Variables

A_c	heat pipe system collector area [2.41 m ²]		(see Table 3.1 for more detail) [W/m ² K]
$A_{cnds\ r}$	surface area of the condenser [m ²]	k_{23^*}	conductance between nodes 2 and 3* in the thermal network used in computer simulations (see Table 3.1 for more detail) [W/m ² K]
A_{cond}	cross-sectional area of the condenser [m ²]		
A_s	total heat transfer surface area of the storage tank walls [m ²]	k_{3^*6}	conductance between nodes 3* and 6 in the thermal network used in computer simulations (see Table 3.1 for more detail) [W/m ² K]
c_p	specific heat for water used for thermal storage [4186 J/kg·K]		
D	outside diameter of the heat pipes [0.029 m]		
g	acceleration due to gravity [9.81 m/s ²]	k_{34}	conductance between nodes 3 and 4 in the thermal network used in computer simulations (see Table 3.1 for more detail) [W/m ² K]
$h_{cnds\ r}$	convection coefficient for the exposed condenser to room air [W/m ² K]		
h_{rad}	heat transfer coefficient for radiation between the storage tank wall and room envelope [W/m ² K]	k_{41}	conductance between nodes 4 and 1 in the thermal network used in computer simulations (see Table 3.1 for more detail) [W/m ² K]
$h_{rad,cnds\ r}$	heat transfer coefficient for radiation between the exposed condenser and room envelope [W/m ² K]	k_{45}	conductance between nodes 4 and 5 in the thermal network used in computer simulations (see Table 3.1 for more detail) [W/m ² K]
$h_{s/r}$	convection coefficient for water (h_s) or room air (h_r), respectively [W/m ² K]	k_{56}	conductance between nodes 5 and 6 in the thermal network used in computer simulations (see Table 3.1 for more detail) [W/m ² K]
k_{12}	conductance between nodes 1 and 2 in the thermal network used in computer simulations (see Table 3.1 for more detail) [W/m ² K]		
k_{23}	conductance between nodes 2 and 3 in the thermal network used in computer simulations	k_{67}	conductance between nodes 6 and 7 in the thermal network used in computer simulations

	(see Table 3.1 for more detail) [W/m ² K]		for the new model) to the room [W]
k_{71}	conductance between nodes 7 and 1 in the thermal network used in computer simulations (see Table 3.1 for more detail) [W/m ² K]	\dot{Q}_s	rate of increase of energy (power) gained by the system thermal mass storage (water) over a one-hour interval [W]
k_{ij}	heat transfer coefficient between nodes i and j within a thermal network [W/m ² K]	\dot{Q}_u	useful thermal gains for the system; transferred from the heat pipes to the thermal storage and room [W]
$k_{s/r}$	thermal conductivity for water (k_s) or room air (k_r), respectively [W/m*K]	$R_{cnds r}$	total thermal resistance from the exposed condenser to room air [K/W]
k_w	thermal conductivity of the storage tank wall [0.5 W/m*K]	R_{cond}	conductive resistance through the storage tank wall [K/W]
L	storage tank wall height [1.52 m]	$R_{conv,cnds r}$	convective resistance between the exposed condenser and the room air [K/W]
m_i	capacitance of node i within a thermal network [J/K]	$R_{r,conv}$	convective resistance between the outside of the tank wall and the room air [K/W]
M	mass of the water in the thermal storage tanks [kg]	R_{rad}	radiative resistance between the outside of the tank wall and the room envelope [K/W]
N_{exp}	number of condensers exposed directly to room air	$R_{rad,cnds r}$	radiative resistance between the exposed condenser and the room envelope [K/W]
Nu_D	Nusselt number for free convection from a heated tube	$R_{s,conv}$	convective resistance between storage water and the inside tank wall [K/W]
$Nu_{s/r}$	Nusselt number for water (Nu_s) or room air (Nu_r), respectively	R_{sr}	total thermal resistance from the thermal storage to room air [K/W]
$Pr_{s/r}$	Prandtl number for water (Pr_s) or room air (Pr_r), respectively	Ra_D	Rayleigh number for free convection from a heated tube
$q_{a,aux}$	simulated annual auxiliary heating load per unit collector area [kWh/m ²]	$Ra_{s/r}$	Rayleigh number for water (Ra_s) or air (Ra_r)
$q_{a,hl}$	simulated annual space heating load per unit collector area [kWh/m ²]	S	insolation received by the collector [W/m ²]
\dot{q}_{ij}	heat transfer rate between arbitrary nodes i and j within a thermal network [W/m ²]		
\dot{Q}_{out}	rate of energy (power) transferred from the storage tanks (and exposed condenser		

S_i	insolation received by node i within a thermal network [W/m ²]		pipe used for computer simulations [K]
S_{io}	insolation received by node i , for the previous time step, within a thermal network [W/m ²]	T_a	ambient temperature [°C, K]
SF	simulated solar fraction	T_b	base temperature used for calculating annual heating and cooling loads in computer simulations [65°F]
t_w	storage tank wall thickness [3.18 mm]	T_{cndsr}	temperature of the exposed condenser [°C, K]
T_1	temperature of node 1 for the thermal network of the heat pipe used for computer simulations [K]	T_i	temperature of node i within a thermal network [K]
T_2	temperature of node 2 for the thermal network of the heat pipe used for computer simulations [K]	T_{io}	temperature of node i , for the previous time step, within a thermal network [K]
T_3	temperature of node 3 for the thermal network of the heat pipe used for computer simulations [K]	T_j	temperature of node j , for the previous time step, within a thermal network [K]
T_{3^*}	temperature of node 3* for the thermal network of the heat pipe used for computer simulations [K]	T_{jo}	temperature of node j within a thermal network [K]
T_4	temperature of node 4 for the thermal network of the heat pipe used for computer simulations [K]	T_r	hourly average temperature of the room [°C, K]
T_5	temperature of node 5 for the thermal network of the heat pipe used for computer simulations [K]	T_s	hourly average temperature of the storage tank water [°C, K]
T_6	temperature of node 6 for the thermal network of the heat pipe used for computer simulations [K]	T_w	storage tank wall temperature [°C, K]
T_7	temperature of node 7 for the thermal network of the heat pipe used for computer simulations [K]	α	thermal diffusivity [m ² /s]
		β	volumetric thermal expansion coefficient [K ⁻¹]
		ε	radiative emissivity of the storage tank wall [0.95]
		ε_{cndsr}	radiative emissivity of the copper condenser [0.02]
		ΔT_s	storage water temperature change over a one-hour interval [°C, K]
		ΔT_{sw}	temperature difference between storage water and tank wall [°C, K]
		ΔT_{wr}	temperature difference between tank wall and room air [°C, K]

Δt	time interval [one hour]	ν	kinematic viscosity [m ² /s]
η	thermal efficiency for the heat pipe system	σ	Stefan-Boltzmann constant [5.67x10 ⁻⁸ W/m ² K ⁴]
μ	uncertainty for error propagation		

Superscript

+ only positive values of the argument in the parenthesis are summed

Nomenclature for Chapter 4: “Reducing Unwanted Thermal Gains during the Cooling Season for a Solar Heat Pipe System”

Variables

A_c	heat pipe system collector area [2.41 m ²]		(see Table 3.1 for more detail) [W/m ² K]
$A_{cnds\ r}$	surface area of the condenser [m ²]	k_{23}	conductance between nodes 2 and 3 in the thermal network used in computer simulations (see Table 3.1 for more detail) [W/m ² K]
A_s	total heat transfer surface area of the storage tank walls [m ²]		
c_p	specific heat for water used for thermal storage [4186 J/kg·K]	k_{23^*}	conductance between nodes 2 and 3* in the thermal network used in computer simulations (see Table 3.1 for more detail) [W/m ² K]
cf	correction factor from bench-scale experiments used to correlate radiation measured at each corner of the collector to mean radiation across the collector	k_{3^*6}	conductance between nodes 3* and 6 in the thermal network used in computer simulations (see Table 3.1 for more detail) [W/m ² K]
D	outside diameter of the heat pipes [0.029 m]		
g	acceleration due to gravity [9.81 m/s ²]	k_{34}	conductance between nodes 3 and 4 in the thermal network used in computer simulations (see Table 3.1 for more detail) [W/m ² K]
$h_{cnds\ r}$	convection coefficient for the exposed condenser to room air [W/m ² K]	k_{41}	conductance between nodes 4 and 1 in the thermal network used in computer simulations (see Table 3.1 for more detail) [W/m ² K]
h_{rad}	heat transfer coefficient for radiation between the storage tank wall and room envelope [W/m ² K]	k_{45}	conductance between nodes 4 and 5 in the thermal network used in computer simulations (see Table 3.1 for more detail) [W/m ² K]
$h_{rad,cnds\ r}$	heat transfer coefficient for radiation between the exposed condenser and room envelope [W/m ² K]	k_{56}	conductance between nodes 5 and 6 in the thermal network used in computer simulations
$h_{s/r}$	convection coefficient for water (h_s) or room air (h_r), respectively [W/m ² K]		
k_{12}	conductance between nodes 1 and 2 in the thermal network used in computer simulations		

	(see Table 3.1 for more detail) [W/m ² K]	$q_{a,sw}$	simulated annual heat transfer out of the heat pipe system per unit collector area [kWh/m ²]
k_{67}	conductance between nodes 6 and 7 in the thermal network used in computer simulations (see Table 3.1 for more detail) [W/m ² K]	$q_{m,hl}$	simulated monthly space heating load per unit collector area [kWh/m ²]
k_{71}	conductance between nodes 7 and 1 in the thermal network used in computer simulations (see Table 3.1 for more detail) [W/m ² K]	$q_{m,uwg}$	simulated monthly unwanted thermal gains to storage and room, per unit collector area [kWh/m ²]
k_{ij}	heat transfer coefficient between nodes i and j within a thermal network [W/m ² K]	q_{total}	simulated annual (total) space conditioning load per unit collector area [kWh/m ²]
$k_{s/r}$	thermal conductivity for water (k_s) or room air (k_r), respectively [W/m*K]	$q_{a,uwg}$	simulated annual unwanted thermal gains to storage and room, per unit collector area [kWh/m ²]
k_w	thermal conductivity of the storage tank wall [0.5 W/m*K]	\dot{q}_{ij}	heat transfer rate between arbitrary nodes i and j within a thermal network [W/m ²]
L	storage tank wall height [1.52 m]	$\dot{Q}_{cnds r}$	rate of energy (power) transferred from the exposed condenser to the room [W]
m_i	capacitance of node i within a thermal network [J/K]	\dot{Q}_{sr}	rate of energy (power) transferred from the storage tanks to the room [W]
M	mass of the water in the thermal storage tank(s) [kg]	\dot{Q}_s	rate of increase of energy (power) gained by the system thermal mass storage (water) over a one-hour interval [W]
Nu_D	Nusselt number for free convection from a heated tube	\dot{Q}_u	useful thermal gains for the system; transferred from the heat pipes to the thermal storage and room [W]
$Nu_{s/r}$	Nusselt number for water (Nu_s) or room air (Nu_r), respectively	$R_{cnds r}$	total thermal resistance from the exposed condenser to room air [K/W]
$Pr_{s/r}$	Prandtl number for water (Pr_s) or room air (Pr_r), respectively	R_{cond}	conductive resistance through the storage tank wall [K/W]
$q_{a,aux}$	simulated annual auxiliary heating load per unit collector area [kWh/m ²]		
$q_{a,cl}$	simulated annual space cooling load per unit collector area [kWh/m ²]		
$q_{a,hl}$	simulated annual space heating load per unit collector area [kWh/m ²]		

$R_{conv,cndsr}$	convective resistance between the exposed condenser and the room air [K/W]		pipe used for computer simulations [K]
$R_{r,conv}$	convective resistance between the outside of the tank wall and the room air [K/W]	T_3	temperature of node 3 for the thermal network of the heat pipe used for computer simulations [K]
R_{rad}	radiative resistance between the outside of the tank wall and the room envelope [K/W]	T_{3^*}	temperature of node 3* for the thermal network of the heat pipe used for computer simulations [K]
$R_{rad,cndsr}$	radiative resistance between the exposed condenser and the room envelope [K/W]	T_4	temperature of node 4 for the thermal network of the heat pipe used for computer simulations [K]
$R_{s,conv}$	convective resistance between storage water and the inside tank wall [K/W]	T_5	temperature of node 5 for the thermal network of the heat pipe used for computer simulations [K]
R_{sr}	total thermal resistance from the thermal storage to room air [K/W]	T_6	temperature of node 6 for the thermal network of the heat pipe used for computer simulations [K]
Ra_D	Rayleigh number for free convection from a heated tube	T_7	temperature of node 7 for the thermal network of the heat pipe used for computer simulations [K]
$Ra_{s/r}$	Rayleigh number for water (Ra_s) or air (Ra_r)	T_a	ambient temperature [°C, K]
S	insolation received by the collector [W/m ²]	T_b	base temperature used for calculating annual heating and cooling loads in computer simulations [65°F]
S_i	insolation received by node i within a thermal network [W/m ²]	T_{cndsr}	temperature of the exposed condenser [°C, K]
S_{io}	insolation received by node i , for the previous time step, within a thermal network [W/m ²]	T_i	temperature of node i within a thermal network [K]
SD	season determination ratio	T_{io}	temperature of node i , for the previous time step, within a thermal network [K]
SF	simulated solar fraction		
t_w	storage tank wall thickness [3.18 mm]		
T_1	temperature of node 1 for the thermal network of the heat pipe used for computer simulations [K]		
T_2	temperature of node 2 for the thermal network of the heat		

T_j	temperature of node j , for the previous time step, within a thermal network [K]	ε_{cnds}	radiative emissivity of the copper condenser [0.02]
T_{jo}	temperature of node j within a thermal network [K]	ΔT_s	storage water temperature change over a one-hour interval [$^{\circ}\text{C}$, K]
T_r	hourly average temperature of the room [$^{\circ}\text{C}$, K]	ΔT_{sw}	temperature difference between storage water and tank wall [$^{\circ}\text{C}$, K]
T_s	hourly average temperature of the storage tank water [$^{\circ}\text{C}$, K]	ΔT_{wr}	temperature difference between tank wall and room air [$^{\circ}\text{C}$, K]
T_w	storage tank wall temperature [$^{\circ}\text{C}$, K]	Δt	time interval
α	thermal diffusivity [m^2/s]	η	thermal efficiency for the heat pipe system
β	volumetric thermal expansion coefficient [K^{-1}]	μ	uncertainty for error propagation
ε	radiative emissivity of the storage tank wall [0.95]	ν	kinematic viscosity [m^2/s]
		σ	Stefan-Boltzmann constant [$5.67 \times 10^{-8} \text{ W/m}^2\text{K}^4$]

Superscript

+ only positive values of the argument in the parenthesis are summed

Nomenclature for Chapter 5: “U.S. Space Cooling Potentials for Ambient Sources with Thermal Energy Storage”

Variables

A	building floor area [m ²]	$f_{as,1d}$	fraction of the daily load that can be met by a respective ambient source
$ACDD$	annual ambient source cooling capacity [°F days]	F_{as}	fraction of the annual load that can be met by a respective ambient source
ALR	annual cooling potential to cooling load ratio	$F_{as,1d}$	fraction of the annual load that can be met by a respective ambient source using ‘one day’s worth’ of thermal storage
c_{liq}	specific heat for a phase change material as a liquid [J/kg*K]	M^*	thermal storage mass required to store sufficient energy to serve the load during an interval, t_{nas} , with no ambient source cooling potential [kg]
c_p	specific heat for a material or substance [J/kg*K]	M_{max}^*	thermal storage mass required to meet the entire annual cooling load [kg]
c_{sol}	specific heat for a phase change material as a solid [J/kg*K]	P	barometric pressure (kPa)
C^*	thermal storage capacitance, normalized by building UA , required to serve the load during an interval, t_{nas} , with no ambient source cooling potential [days]	t	number of hours from midnight; used to calculate T_s
C_{max}^*	thermal storage capacitance, normalized by building UA , required to meet the entire annual cooling load [days]	th	thickness of a respective thermal storage material to meet the annual cooling load
CDD	annual cooling load [°F days]	t_{nas}	period(s), over the course of a year, in which there is no ambient source cooling potential
CDD_{nas}	cooling load during corresponding period t_{nas} in which there is no ambient source cooling potential [°F days]	$t_{nas,max}$	longest period, over the course of a year, in which there is no ambient source cooling potential
$CDD_{nas,max}$	largest cooling load amongst all intervals of CDD_{nas} [°F days]	T^*	phase change temperature [°F]
CDH	hourly cooling load [°F hours]	T_a	ambient temperature [°F]
e	factor used to calculate T_{wb} ; defined in Equation 5.7		

T_{as}	temperature of respective ambient source [$^{\circ}\text{F}$]	UA	building overall loss coefficient [W/K]
T_b	base temperature used for degree-day method [65°F]	Z	depth below ground surface
$T_{c,hi}$	upper temperature limit of indoor comfort range [72°F]	γ	factor used to calculate T_{wb} ; defined in Equation 5.5
$T_{c,lo}$	lower temperature limit of indoor comfort range [68°F]	δ	factor used to calculate T_{wb} ; defined in Equation 5.6
T_{dp}	dew-point temperature [$^{\circ}\text{F}$]	ΔT	difference in temperature
T_g	ground temperature [$^{\circ}\text{F}$]	ϕ	relative humidity
T_{mean}	annual mean ground surface temperature [$^{\circ}\text{F}$]	λ	heat of fusion of phase change material [kJ/kg]
T_s	sky temperature [$^{\circ}\text{F}$]	ρ	density of a respective phase change material [kg/m^3]
T_{wb}	wet-bulb temperature [$^{\circ}\text{F}$]		

Superscript

+ only positive values of the argument in the parenthesis are summed

CURRICULUM VITAE

Brian Scott Robinson

7029 Rainelle Dr
Lanesville, IN 47136
(502) 291-9463 (812) 923-7584
bsrobi02@louisville.edu

EDUCATION

- 8/09 – 4/14 University of Louisville Speed School of Engineering, Louisville, KY
PhD Mechanical Engineering, with High Honors

Dissertation: “Advancements in Alternative Energy Applications for Passive Space Conditioning”
- 8/08 – 8/09 University of Louisville Speed School of Engineering, Louisville, KY
MEng Mechanical Engineering, with High Honors

Thesis: “Sackett Hall Solar System Data Acquisition, Display, and Experimental Implementation”
- 8/04 – 8/08 University of Louisville Speed School of Engineering, Louisville, KY
BS Mechanical Engineering, with High Honors
- 8/01 – 5/03 University of New Orleans, New Orleans, LA
Mechanical Engineering, 43 Semester Hours Completed
GPA: 3.7 / 4.0

WORK EXPERIENCE

- 8/12 – 4/14 Tutor Doctor of Louisville
Tutor
- Worked as an independent contractor tutoring various clients with ages ranging from middle school to high school to adults at the college level.
- 8/09 – 8/13 University of Louisville: Renewable Energy Applications Laboratory
(REAL), Louisville, KY
- Graduate Research Assistant
- Integral part of REAL’s day-to-day research and operations, including a number of presentations for visitors to the lab as well as off-campus presentations for funding agencies and school groups
- 5/07 - 8/07, 8/06 - 12/06, & 1/06 – 5/06 Essroc Italcementi, Speed, IN
Mechanical Engineering Cooperative Internship
- Member of cement company’s Maintenance Department: responsible for building extensive Bill of Material (BOM)

database for the plant from scratch, foremen supervision, developing and implementing weekly maintenance plans, and the design and construction of the kiln intake fan partition and ductwork

1/07 – 5/07 & 5/06 – 8/06

Essroc Italcementi, Speed, IN
Part-time Purchasing Director

- Worked part-time between co-op tenures with cement company's Purchasing Department
- Responsible for day-to-day purchasing necessities including daily parts and materials receiving, and creating and sending company purchase orders

6/01 – 8/04

U.S. Navy: Enlisted Placement Management Center, New Orleans, LA
Detailer

- Assigned and placed U.S. Navy GENDET personnel throughout the fleet
- Reviewed, drafted and released all official naval messages for my command
- Provided customer service to naval career counselors throughout the fleet
- Maintained divisions' financial records
- Supervised 6 junior detailers in my department

8/95 – 5/01

U.S. Navy: USS McClusky, FFG-41, San Diego, CA
Engineman

- Supervised Auxiliary Division: responsible for operation of and preventive/corrective maintenance on ship's service diesel generators, high and low pressure air compressors, distilling plants, RAST helicopter recovery system, steering gear, fin stabilizers, and various auxiliary equipment associated with laundry and messing services
- Trained numerous personnel on auxiliary equipment fundamentals for watch-standing qualification(s), maintenance procedures, and casualty control to pass engineering certification assessments
- Stood watch while underway as Electric Plant Control Console Operator

TEACHING EXPERIENCE

8/12 – Present

Tutor Doctor of Louisville
Tutor

- Have successfully tutored 14 clients/students in the Louisville area primarily in the following subjects: all levels of mathematics, chemistry, and standardized test preparation (ACT, SAT, ASVAB, GRE, etc.)

8/10 – 12/13
Louisville, KY

University of Louisville: Department of Mechanical Engineering,

Instructor

- Taught graduate-required Mechatronics course (ME 644) in Fall semester, 2010 when the tenured professor was involved in a severe traffic accident at the start of the semester and recommended I cover the remainder of the course
- Starting in Fall semester, 2012, taught full-semester courses in department as follows:
 - ME 314: Engineering Measurements
Course Evaluations: Fall 2013 4.25 / 5
 - ME 422: Machine Design I
Course Evaluations: Fall 2013 4.45 / 5

- ME 440:	Heat Transfer		
	Course Evaluations:	Spring 2013	4.29 / 5
		Fall 2013	4.20 / 5
- ME 442:	Machine Design II		
	Course Evaluations:	Fall 2012	4.67 / 5
- ME 560:	Nuclear Engineering		
	Course Evaluations:	Fall 2012	4.31 / 5
		Fall 2013	4.42 / 5
- ME 575:	Manufacturing Processes		
	Course Evaluations:	Spring 2013	4.54 / 5
- ME 610:	Data Acquisition & Digital Signal Processing		
	Course Evaluations:	Summer 2013	4.00 / 5
- ME 618:	Heat Exchanger Design		
	Course Evaluations:	Summer 2013	4.25 / 5

8/09 – 8/13
(REAL), Louisville, KY

University of Louisville: Renewable Energy Applications Laboratory

Graduate Research Assistant

- Trained and advised 17 undergraduate and graduate students for various REAL related projects

8/08 – 8/09
Louisville, KY

University of Louisville: Department of Mechanical Engineering,

Teaching Assistant

- Taught and supervised students in undergraduate-required laboratory courses
- Evaluated student technical reports and provided constructive feedback

8/05 – 12/05

University of Louisville: Speed School of Engineering, Louisville, KY

- Graded exams, quizzes and homework assignments pertaining to Engineering Analysis Core (i.e. Calculus) classes
- Tutored students that requested assistance with mathematical concepts in which they were struggling

RESEARCH PUBLICATIONS

Peer-Reviewed Journal Articles:

1. **Robinson BS** & Sharp MK, "Reducing Unwanted Thermal Gains during the Cooling Season for a Solar Heat Pipe System," *Solar Energy* (submitted 2014).
2. **Robinson BS** & Sharp MK, "Heating Season Performance Improvements for a Solar Heat Pipe System," *Solar Energy* (submitted 2014).
3. **Robinson BS**, Dorwart J, Sharp MK, "US Space Cooling Potentials for Ambient Sources with Thermal Energy Storage," *International Journal of Ambient Energy*, published online, DOI: 10.1080/01430750.2013.864585 (hard copy to be published in next issue).

4. **Robinson BS**, Chmielewski NE, Knox Kelecy A, Brehob EG, Sharp MK, "Heating Season Performance of a Full-scale Heat Pipe Assisted Solar Wall," *Solar Energy* 87:1:76-83, 2013.
5. Albanese MV, **Robinson BS**, Brehob EG, Sharp, MK, "Simulated and Experimental Performance of a Heat Pipe Assisted Solar Wall," *Solar Energy* 86:5:1552-62, 2012.

Conference Presentations with Reviewed Paper in Proceedings:

6. **Robinson BS** & Sharp MK, "A Reconfigurable Passive Solar Test Facility," ASME 2012 6th International Conference on Energy Sustainability, San Diego, CA, Jul 23-26, 2012.
7. **Robinson BS** & Sharp MK, "Reducing Unwanted Gains During the Cooling Season from a Heat Pipe Augmented Passive Solar Heating System," ASME 2012 6th International Conference on Energy Sustainability, San Diego, CA, Jul 23-26, 2012.
8. **Robinson BS** & Sharp MK, "Space Cooling Potentials for Ambient Energy Sources Across the U.S.," ASME 2011 5th International Conference on Energy Sustainability, Washington, DC, Aug 7-10, 2011.
9. **Robinson BS** & Sharp MK, "Heating Season Performance of a Heat Pipe Passive Solar Heating System," ASES Conference, Raleigh, NC, May 17-20, 2011.
10. **Robinson BS**, Albanese MV, Chmielewski N, Brehob EG, Sharp MK, "Heat Pipe Augmented Solar Heating System," ASME 2010 4th International Conference on Energy Sustainability, Phoenix, AZ, May 17-22, 2010.

HONORS & AWARDS

- Tutor Doctor of Louisville "Tutor of the Year" award for 2013
- ASME / UofL Joint Chapter Most Outstanding Research Presentation Award
- U.S. Department of Energy PhD Scholarship & Stipend
- University of Louisville Master's of Engineering Scholarship & Stipend
- 3 Navy & Marine Corp Achievement Medals
- Armed Forces Expeditionary Medal
- Southwest Asia Service Medal
- 3 Sea Service Deployment Ribbons